# SURFACE XRF MAPPING FOR INTRAPARTICLE HETEROGENEITY ASSESSMENT AND PARTICLE GRADE ESTIMATION

by

Santiago Seiler

B.Eng., Universidad de la República, 2015

A THESIS SUBMITTED IN PARTIAL FULFILLMENT OF

THE REQUIREMENTS FOR THE DEGREE OF

MASTER OF APPLIED SCIENCE

in

THE FACULTY OF GRADUATE AND POSTDOCTORAL STUDIES

(Mining Engineering)

THE UNIVERSITY OF BRITISH COLUMBIA

(Vancouver)

December 2017

# ABSTRACT

Sensor-based sorting is perceived as a feasible solution for some of the most critical aspects of mineral processing. There are two basic classes of sensors, 1. those that measure a property characteristic of the bulk of a particle; and 2. those that measure a property of the surface of a particle. For the second class, the surface measurement is then correlated to the bulk property of interest. The correlation does not only depend on how well the sensors can analyze the surface, but also on how well the surface correlates to the volume of the rock. The correlation is even more complex since only part of the rock surface is scanned by an actual sorter. Thus, the heterogeneity within each particle, defined as intraparticle heterogeneity, is an important variable to be characterized.

The main objective of this work was to design and develop a method for rock surface mapping to assess intraparticle heterogeneity and to evaluate the correlation between surface grade and bulk grade for run of the mine or primary crushed rocks. The XRF mapping technique developed, and the procedure selected to analyze the mapping data, were described and applied to two porphyry copper ore samples.

According to an univariate statistical analysis, for the samples analyzed, copper and iron data distributions did not follow either normal or lognormal distribution. Median and median absolute deviation were proposed as the best parameters to summarize the surface grade and the intraparticle heterogeneity, respectively. The median value of the surface grade data showed the best correlation to the bulk grade of the rock for both elements.

For the copper ore used in this work, with mainly vein type mineralization, the one-dimensional heterogeneity assessment showed a high degree of intraparticle heterogeneity. This characteristic of the ore might generate poor reproducibility in the results of an XRF sorter when sensing only one face of each rock. The variogram was evaluated as a measure of heterogeneity in two dimensions. Two-color mapping method was selected to display the data collected in the XRF mapping for both samples analyzed.

# LAY ABSTRACT

Grinding is necessary to separate valuable minerals from non-valuable in rocks, but because it consumes a lot of energy and water, so it is important to grind only the rocks that have valuable minerals. This research focuses on sorting rocks, where the rocks without valuable minerals (waste) are rejected before they go to the mill but to do this, a way to know whether they are waste or not is required. One option is to measure a property at the surface and use this property to decide, but this is not easy because in mining a lot of rocks are processed per second so we just have time to measure part of the surface. This work studies how similar is the surface of each rock to the whole rock and how good is to measure only part of the surface to decide whether the rock is waste or not.

# PREFACE

The idea to develop a method to scan rock surfaces for enhancing the understanding of the rock heterogeneity arose from a discussion between the author and Xuejie Deng. This discussion was the starting point for this thesis. The X-Ray Fluorescence mapping method was developed by the author, Xuejie Deng and Sijia Liu. The data collection was carried out by the author, Xuejie Deng, Sijia Liu and Xinyang Yu.

The approach selected to process and to analyze the data collected was defined by the author. The scripts and implementation used for the data analysis, as well as the manuscript preparation was done by the author.

# TABLE OF CONTENTS

# LIST OF TABLES

# LIST OF FIGURES

# LIST OF SYMBOLS

Cu = Copper grade [%]

$CH_L$= Constitution heterogeneity [-]

$d_i$ = Average diameter of a grain of phase i [µm]

$d_p$ = Texture dimension [µm]

Fe = Iron grade [%]

$h$ = Lag distance [mm]

$m_x$ = Mode grade [%]

$N(h)$ = Number of pairs [-]

$v_i$ = Volume fraction of phase i [$\mu m^3$]

$z$ = Raw data point [%]

$z*$ = Data point after Box-Cox transformation [-]

$z_x$ = Observed value at the location [%]

$z_{x+h}$ = Observed value at another point at a distance $h$ [%]

$\gamma(h)$ = Semivariogram [-]

$\lambda$ = Box-Cox coefficient [-]

$\mu_x$ = Mean grade [%]

# LIST OF ABBREVIATIONS

AEM/EDS: Analytical transmission electron microscope/energy-dispersive spectrometer.

AEM/PEELS: Analytical transmission electron microscope/parallel collection electron energy loss spectrometer.

CCD: Charge-coupled device

CV: Coefficient of variation.

EPMA/WDS: Electron probe microanalyzer/wavelength-dispersive spectrometer.

HG: High grade sample.

LG: Low grade sample.

LIBS: Laser-induced breakdown spectroscopy.

MLA: Mineral liberation analysis.

MW/IR: Microwave/infrared.

PFTNA: Pulsed fast thermal neutron activation.

PGNAA: Prompt gamma neutron activation analysis.

PIXE: Proton induced X-ray emission.

QEMScan: Quantitative evaluation of minerals by scanning electron microscopy.

RGB: Red, green and blue.

SAM/AES: Scanning Auger microscope/Auger electron spectrometer.

SEM/EDS: Scanning electron microscope/energy-dispersive spectrometer.

SIMS: Secondary ion mass spectrometer.

XRF-S: X-Ray Fluorescence – Spectroscopy.

XRL/UV: X-Ray Luminescence/ultraviolet.

XRT: X-Ray Transmission.

# ACKNOWLEDGEMENTS

I would like to thank Dr. Bern Klein for his supervision and support throughout this thesis research. Also, I would like to express my deepest gratitude to Dr. Aldo Bologna for his excellent guidance, caring, patience, and encouraging me to come to Canada to pursue this master. Also, thanks to Dr. Gustavo Sánchez for his support during the last two years.

I would like to thank Xuejie Deng, who as a good friend, was always willing to help and give his best suggestions. It would have been a lonely lab without him. Many thanks to Sijia Liu, Mike McClintock and the other fellow students at CMP lab for their support, as well as Pius Lo for his good suggestions and patience.  I have to appreciate the guidance given by Dr. Andrew Bamber to my research that has improved the organization of this manuscript, thanks to his comments and advices. Also, thanks to Dr. Don Hallbom for the time that he invested in showing me how to find the odd trend and how much “fuzzy” is the world. My research would not have been possible without their helps.

I would like to acknowledge the financial support of the Agencia Nacional de Investigación e Innovación (ANII) from Uruguay and the International Development Research Centre (IDRC) during the two years of my master program.

I would also like to thank my parents, my sister, and my friends. They were always supporting me and encouraging me with their best wishes. Finally, special thanks to the support and motivation of Florencia, it would have been much harder to finish my thesis without her.

# 1. INTRODUCTION

## 1.1 Sensor-based sorting

In the mining industry, one of the main challenges is the proper identification of ore and waste. Due to the large size scale that is commonly used for resource modelling and mine planning, waste or barren material may be introduced as ore to the process, and ore may report to the waste dump. The efficiency of a process directly depends on the quality of the material to be processed, so improvements that could minimize the dilution are of great interest to mining companies. The addition of a pre-concentration stage, such as mineral sorting, prior to milling has shown to have a significant effect by reducing dilution.

Mineral sorting has been applied in the mining industry since the industry beginnings. In the early stages of the industry hand sorting was the method used. In this method, the identification of ore was carried out based on what people were able to detect regarding color, weight, brightness, breakage, and other properties of the rocks. Since this method cannot be applied to large scale mining, sensor-based sorting has become an interesting alternative.

The first review on sensor-based sorting was published in 1972 by R.A. Wyman, which described the first "true" sensor-based sorter, developed in 1947 (Wyman, 1972). That sorter was able to detect and isolate uranium-bearing pieces of rocks.

The term used to describe the technology has changed over the years. Wyman defined this technology as electronic sorting, and explained the origins indicating: *'Sorting by machine became feasible with the advent of a means of duplicating some of the functions of the brain. The means was provided by modern electronics, so, for this reason, machine sorting is usually referred to as "electronic sorting"* (Wyman, 1972). Furthermore, Salter and Wyatt, who published another review for this technology in 1991, called it "Automated Sorting" (Salter & Wyatt, 1991). However, most recently the sorting technology is referred to as sensor-based sorting, as introduced by H. Wotruba (Wotruba, 2006).

The sorting process description has not changed from Wyman's description in 1972. The process consists of four different elements: (i) a method of presentation or feeding; (ii) a method of distinguishing one "mineral" or grade of "mineral" from others; (iii) a method of comprehending and using this information; and (iv) a method of separating one "mineral" from others (Wyman, 1972). These methods or sub-processes interact with each other. There are two types of applications of sensor-based sorting: particle and bulk sorting (Klein & Bamber, 2017). In particle sorting, the separation is applied to individual particles, whereas in bulk sorting, the separation is applied to a group of particles. Figure 1.1 shows a flowchart with the interactions between the different sub-processes for particle sorting, which represents the focus of this study.

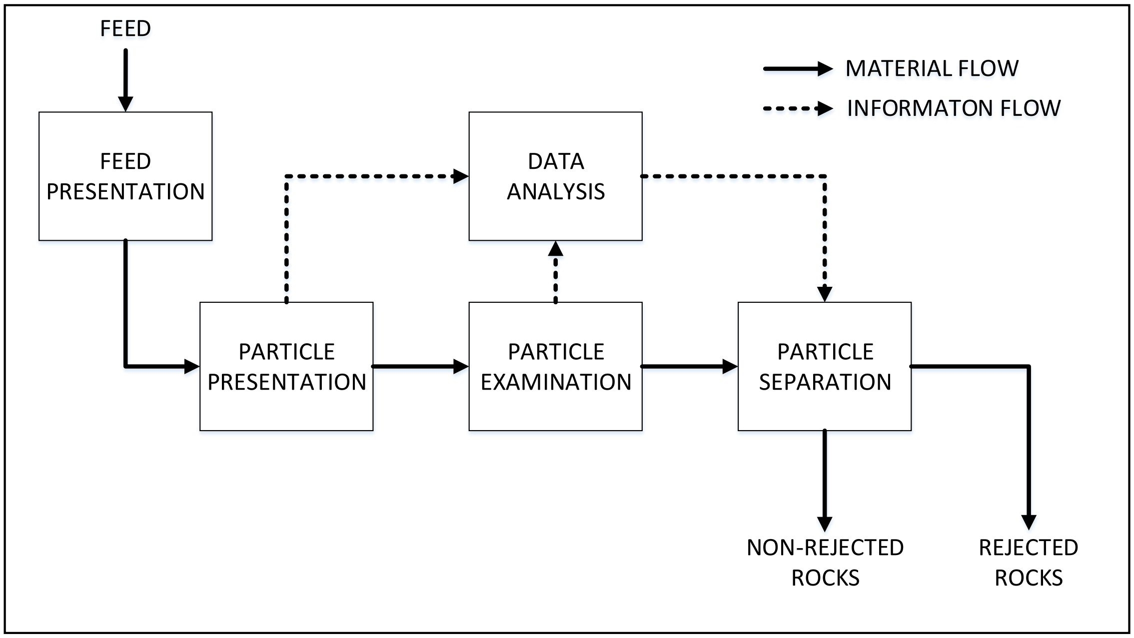

**Figure 1.1:** Particle sorting machine sub-processes interactions (Salter & Wyatt, 1991).

Table 1.1 shows a list of the sensors that are applicable to ore sorting, which exploit a wide variety of physical properties at different scales. Based on the sensed property, sensors can be usually divided in two classes: volumetric or surface. Sensors that correlate a volumetric property to metal grades are considered to have a higher degree of confidence for sorting.

**Table 1.1:** Sensor types for ore sorting (Klein & Bamber, 2017).

| Technology | Physical Property | Principle | (Surface/ Volume) | Ore Types | Sorting applications (particle/bulk) | Manufacturer |
|---|---|---|---|---|---|---|
| Radiometric (Scintillometer) | Natural Gamma Radiation | Radioactivity | Volume | Uranium, Witwatersrand Gold Ores | Particle/Bulk | Tomra |
| PGNAA, PFTNA | Elemental Composition | Neutron activation/ gamma emission | Volume | Iron ore | Bulk | Scantec, Thermo Fisher, PANalytical |
| X-Ray Transmission (XRT) | Atomic Density | Atomic Density | Volume | Base/Precious Metals, Coal, Diamonds, sulphides, etc | Particle | Steinert, Tomra |
| X-Ray Fluorescence Spectroscopy (XRF-S) | Elemental Composition | Inner shell electron excitation | Surface | Base/Precious Metals, Metal Sulphides | Particle/Bulk | Minesense, Rados, Steinert, IMA |
| Laser Fluorescence/X-Ray Fluorescence | Visible Fluorescence under X-Ray/Laser stimulation | Fluorescence | Surface | Diamonds, Limestone, Iron Ore, Sulphides | Particle/Bulk | IMA, AIS Sommer |
| Microwave-Infrared (MW/IR) | Microwave Absorption, Heat Conductivity | Polar bond excitation | Surface | Base Metals, Carbonaceous Materials | Particle | |
| Laser Induced Breakdown Spectroscopy (LIBS) | Elemental Composition | Electron excitation/light emission | Volume | | Particle | Secopta, LDS, LSA |
| X-Ray Luminescence XRL/UV | | Luminescence through x-ray or UV stimulation | Surface | Diamonds | Particle | Tomra / De Beers |
| Photometric (CCD) | RGB/Colour, Grey Scale, Surface, Texture, Size/Shape | Chromatic Reflectance/ absorption | Surface | Industrial Minerals, Gem Stones, Diamond, Coal, Massive Sulphides, Phosphates | Particle | Steinert, Tomra |
| Hyper-spectral Analysis | Mineral Composition | | Surface | | Particle | |
| Electromagnetic (EM) | Conductivity/ Magnetic Susceptibility | Electromagnetism/ Induction | Volume | Base Metals, Native Metals, Metal Sulphides, Massive Oxides | Particle/Bulk | Tomra/MineSense |
| Magnetic Resonance Spectroscopy | Minerals Chalcopyrite | Resonant Frequency of molecules | Volume | | | CSIRO |

The general benefits of sorting, either using sensors or other discriminating techniques, are widely discussed in the literature. The following list summarizes the main advantages (Bamber, Klein, & Scoble, 2006; Bamber, Klein, & Stephenson, 2006; Klein & Bamber, 2017; Salter & Wyatt, 1991; Wotruba, 2006; Wyman, 1972):

1. Lower overall capital costs for a given product output.
2. Lower operating costs per unit of production due to savings in energy and wear (especially for milling).
3. Reductions in disposal costs for fine waste (e.g. flotation and leaching tailings) which lead to a reduction of the environmental impact.
4. Overall improved process recovery (optimum feed-rate with a consistent grade of material).
5. Increase on the valuable mineral/metal production of an existing plant.
6. Increase on the reserves/the life span of a deposit by including previously untouched blocks (e.g. with dykes or close to the ore body boundaries), which have been excluded due to unavoidable dilution below cut-off grade.
7. Free reagent operation and lower water consumption.

It must be noted that these advantages are associated with any pre-concentration process (1 to 6) except number (7), which is only associated with sensor-based sorting. Despite these advantages, sensor based technology is still not widely accepted in the mining industry. This lack of interest in the technology may be explained by the technical limitations associated with it, as well as the misconceptions associated with a technology that is still evolving. Low processing capacity and particle size limitations of the material to be treated are part of the main technical challenges.

## 1.2 Ore sortability

Sensor-based technologies are not applicable to all ores. Sortability depends directly on ore heterogeneity, such that a homogeneous ore, uniform in composition, is not amenable to sorting.

Ore sortability studies focus on determining ore amenability to sorting and providing design information for sorting systems. This sortability study is divided into four components: ore heterogeneity, sensor response evaluation, sorting analysis, and feasibility. (Klein & Bamber, 2017)

Ore heterogeneity is an intrinsic property of each mineral deposits and it is considered independent of the sensor or the sorting method to be used. Sensor response evaluation is focused on the study of the correlation between sensor response and the property of interest, typically ore grade. The third component, sorting analysis, takes the results from the first two components and presents a summary analysis in terms of yield/grade/recovery relationships. Finally, the feasibility evaluates the viability of the sorting application considering factors such as economic, technological and scheduling aspects. This thesis was focused solely on ore heterogeneity.

The degree of ore heterogeneity is controlled by the geological processes that occurred during the formation of the orebody. Identification and understanding of lithologies within the orebody and their mineralogy are key elements in the early assessment of ore heterogeneity. For example, visual examination of rocks or drill cores can provide important information about the texture and grade distribution of the valuable minerals throughout the mineral deposit.

Even though visual examination is a useful tool for assessing heterogeneity, testing is needed to validate the observation. In some cases, although a fair degree of heterogeneity could be present, it may not be readily visible. Therefore, different working models have been developed to quantify heterogeneity and, in most cases, the quantification has been depicted as an index or value that can be compared between samples.

One of the main variables associated with heterogeneity is scale. In the mining industry, heterogeneity is usually evaluated at two stages: the block modelling stage, e.g. 5 m x 5 m, in which understanding of heterogeneity helps to distinguish between ore and waste, and the concentration stage, e.g. <500 µm, where mineral liberation is evaluated (Klein & Bamber, 2017). Sensor-based sorting was developed to exploit mid-scale heterogeneity (see Figure 1.2). Little information has been published on mid-scale heterogeneity assessment until recently, when sorting became a topic of interest for the mining industry. Most of the literature on mid-scale heterogeneity comes from sampling theory and its application.

Two terms are introduced in this work to classify the heterogeneity: intraparticle heterogeneity and interparticle heterogeneity. Intraparticle heterogeneity is used to describe the uniformity within a particle or rock. However, interparticle heterogeneity is used to describe the uniformity between rocks.

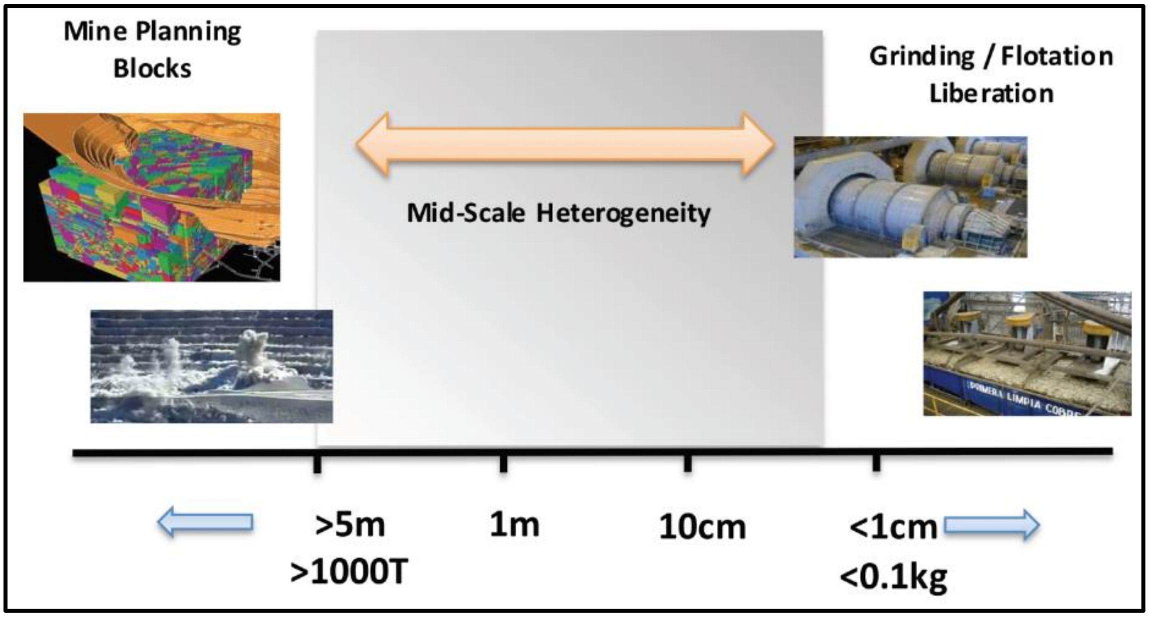

**Figure 1.2:** Schematic illustration of mid-scale heterogeneity ("MineSense Technologies Ltd.", 2015).

## 1.3 Interparticle heterogeneity

Most of the literature found in ore heterogeneity is focused on the heterogeneity between particles, which was previously defined in this study as interparticle heterogeneity (see Introduction Section). Researches have suggested the application of the term constitution heterogeneity ($CH_L$) as an index to evaluate the sorting potential of a sample (Mazhary & Klein, 2015; Robben, Wotruba, Robben, von Ketelhodt, & Kowalczyk, 2013). This term was first introduced by Pierre Gy in the "Theory of Sampling" (Gy, 1979). The constitution heterogeneity is an ex-situ analysis of the uncertainty that is inherent in sampling, where the fragments or rocks are removed from their original location and grouped in lots. The index is represented by the relative dimensionless variance associated with each fragment from a lot of $N_F$ fragments, as follows:

$$CH_L = N_F \sum_i \frac{(a_i - a_L)^2}{a_L^2} \cdot \frac{M_i^2}{M_L^2} \tag{1}$$

where $a_i$ and $a_L$ are the grades of the fragment and the lot, respectively; $M_i$ and $M_L$ are the masses of the fragment and the lot, respectively. Based on the definition, the higher the value of $CH_L$, the higher degree of heterogeneity.

A high $CH_L$ value corresponds to an improved potential sorting performance, with respect to mass pull and recovery (Mazhary & Klein, 2015). Therefore, the $CH_L$ can be used as an indicator to quantitatively characterize the sorting potential of a sample.

Sortability index is another method found in the literature to assess the sorting potential (Wilkie, 2016). This index was developed based on the study of the grade distribution within a group of particles for porphyry copper ores, and it is characterised by four categories based on the relative values of the mean grade $(\mu_x)$ and the mode grade $(m_x)$ for the group of particles under study.

Category 1: $m_x \sim 0.05\% \, and \, \mu_x \sim m_x$. Narrow particle grade distribution with insufficient inhomogeneity to sort high grade particles from barren or near barren particles, mainly seen in disseminated low grade ores. This category is identified as unsortable.

Category 2: $m_x \gg 0.05\% \, and \, \mu_x \sim m_x$. Narrow particle grade distribution that has no barren or near barren particles to reject. This category is identified as unsortable.

Category 3: $m_x \gg 0.05\% \, and \, \mu_x \gg m_x$. Broad particle grade distribution that has no barren or near barren particles to reject., mainly seen in disseminated high grade ores. This category is identified as unsortable.

Category 4: $m_x \sim 0.05\% \, and \, \mu_x \gg m_x$. Broad particle grade that has abundant liberated and near liberated gangue particles to reject. This category is identified as sortable

## 1.4 Intraparticle heterogeneity

As described, several sensors measure the surface properties of the rocks. With these sensors, the ore is sorted based on a response obtained from the surface of the rocks. XRF sensor is an example of a surface sensor. At industrial scale, only part of the surface is scanned and the elemental composition at the rock surface is the measured response used to classify the rock as ore or waste.

The correlation between the surface grade and the bulk grade, and the accuracy of the sensor are the main consideration that determine the performance of surface sensing techniques. A certain correlation between the surface and bulk grades needs to be present in order to achieve a reasonable sorting performance. This correlation between the surface and bulk grades depends on the intraparticle heterogeneity. For homogenous rocks, one measurement at the rock surface is enough to know the bulk grade of that rock, but this is not normally the case when dealing with run of the mine ore.

Most of the literature related to intraparticle heterogeneity is focused on texture analysis. Analysis of the ore texture, distribution of minerals, and grain size are important to mineral processing in order to quantify mineral liberation. The information for this analysis can be obtained by a wide variety of mapping techniques, that are used in technologies such as the Mineral Liberation Analyser

(MLA) and the Quantitative Evaluation of Minerals by Scanning electron microscopy (QEMScan). The results obtained through these analyses can be applied to assessment of flotation, leaching, or gravity concentration processes.

Texture analysis is usually performed on particles that are below 500 µm in size, since, for most of the base and precious metal ores, the valuable mineral is liberated within this size range. The analysis can be performed by using optical or scanning electron microscopy. A few hundred particles are mounted in a resin to be polished afterwards prior to being analyzed. The analysis is focused on mineral identification and not on surface grade mapping.

There is a lack of published information related to texture analysis, or intraparticle heterogeneity analysis, applied to sensor-based sorting. One of the main limitations of the commonly used mapping devices is the maximum particle size. Particle sorters are designed to process material within a size range from 20 mm to 250 mm, but the mapping devices cannot handle such large particle sizes.

The only available published report that applies texture analysis to evaluate sorting potential defined a texture dimension as part of the analysis (Wilkie, 2016). The model proposed for texture analysis was focused on finding the optimal particle size for sorting. For disseminated mineralization, texture dimension was defined as the average distance between sulphide grains embedded in the gangue matrix. In the model, the texture dimension was quantified by calculating the average size of the particle produced by breaking the texture into smaller pieces. The breakage is designed to fulfill two requirements: 1. each piece contains one sulphide grain, and 2. the average particle grade is the same as the bulk grade of the texture. This definition is illustrated in Figure 1.3.

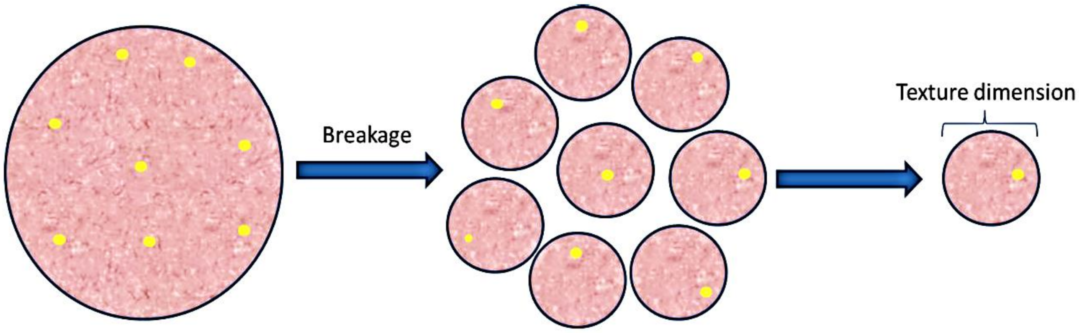

**Figure 1.3:** Schematic illustration of texture dimension concept (Wilkie, 2016).

The texture dimension (*dp*) was calculated according to the following equation (Wilkie, 2016):

$$d_p = \sqrt[3]{\frac{d_i^3}{v_i}} \tag{2}$$

where $d_i$ is the average diameter of a grain of phase, and $v_i$ is the volume fraction of phase *i*.

The texture dimension defines the point of inflection where "liberated" matrix particles are produced during comminution, and the optimum particle size for sorting. The results showed values for texture dimension ranging from 250 µm to 420 µm.

As described, the concepts of the Theory of Sampling have been applied to describe interparticle heterogeneity, and this has contributed to a better understanding of the sorting performance. However, the intraparticle heterogeneity concept and how this heterogeneity relates to the sorting performance of the sample have not been applied to the area of sensor-based sorting.

The variogram of a material at the scale of mineral grain size was proposed as a tool to study in-situ heterogeneity (Lyman, 2011). The aim of Lyman's work was to study the relation between the in-situ heterogeneity and the heterogeneity of the broken material. A variogram function for the valuable mineral phases can be calculated, in the same way that a variogram is calculated from assays in drill cores.

## 1.5 Variography as a tool for intraparticle heterogeneity assessment

### 1.5.1 Geostatistics

A brief introduction to variography analysis, as well as geostatistics, is required in order to understand how this analysis can be applied to analyze intraparticle heterogeneity. Geostatistics is a type of statistics used to analyse data associated with spatial or spatiotemporal phenomena. Matheron stated that: *"Geostatistics, …, are concerned with the study of the distribution in space of useful values for mining engineers and geologists, such as grade, thickness, or accumulation, including a most important practical application to the problems arising in ore-deposit evaluation"* (Matheron, 1963).

However, a modern definition of geostatistics includes the application of their methods to other fields, not only to mining or geology. Geostatistics is focused on describing the autocorrelation of one or more variables in 1D, 2D, 3D space or even in 4D space-time (Trauth, 2007). The description of the autocorrelation can be used to reproduce spatial variability and uncertainty, to make predictions for unobserved locations, and to give information about the accuracy of the predictions.

When dealing with geostatistical data, each measurement is attached to a location and the attributes are taken at only a finite number of points. For the data analysis, the variogram is the tool used to describe the spatial autocorrelation in terms of shape, range, and direction. This tool is being discussed in the following section.

### 1.5.2 Variogram

The variogram was developed as a simple mathematical tool to deal with different aspects of spatial distribution of a regionalized variable, i.e. an actual function taking a definite value in each point of space. The variogram was defined as *"a curve representing the degree of continuity of mineralization"* (Matheron, 1963). In order to quantify the degree of continuity, the following expression for semivariogram ($\gamma(h)$) was proposed:

$$\gamma(h) = \frac{1}{2V} \iiint_V [f(M+h) - f(M)]^2 dV \qquad \textbf{(3)}$$

where $M$ is a point of the geometrical field $V$ by a regionalized random variable $f(M)$, defined on a given geometrical support $v$, with $h$ as a vector argument.

Stationarity is required for the random variable, and there are different orders of stationarity. For the scope of this study, the intrinsic hypothesis (local stationarity) is presented with the following requirements: the local average and variance of the variable, as well as the variance of the difference for all vectors *h* do not depend on the location.

As with other parameters in statistical analysis, the true variograms for spatial continuous processes generally are unknown, and have to be estimated from observations. The estimation procedure of the true variogram is called variography. Variography is divided in three steps, as follows: calculation of the experimental variogram, summary of the experimental variogram by the variogram estimator, and fitting of a variogram model to the variogram estimator.

The expression presented above for the semi-variogram, defined in a 3D space, can be simplified to a 2D space, which is called "experimental semi-variogram", and is defined by the following expression:

$$\gamma(h) = \frac{1}{2 * N(h)} \cdot \sum_{i=1}^{N(h)} (z_{xi} - z_{xi+h})^2 \qquad (4)$$

where $z_x$ is the observed value at the location $x$, $z_{x+h}$ is the observed value at another point at a distance $h$, and $N(h)$ is the number of pairs with the distance $h$.

The terms semivariogram and variogram are often used interchangeably. By definition, $\gamma(h)$ is the semivariogram and $2\gamma(h)$ is the variogram. In this section, $\gamma(h)$ will be referred to as the variogram.

Three main variables need to be defined for variogram construction: lag increment, tolerance, and number of lags, where lag is known as the length of the separation vector *h.* The lag increment defines the distances between points, and tolerance is used when the observations are unevenly spaced, since it defines distance bins for lag increments. The number of lags together with the size of lag increment will limit the total distance for the variogram calculation.

Two practical rules that may be considered when deciding on the value for lag increment and for the number of lags are proposed in the literature (Journel & Huijbregts, 2003): the experimental variogram should only be considered for distance *h* for which the number of pairs (*N(h)*) is greater than 30; and the distance of reliability for an experimental variogram should be $h < D/2$, where *D* is the maximum distance over the data

The *range*, *sill* and *nugget effect* are the most common parameters used to describe variograms. A variogram example with the graphical definition of the main parameters is shown in Figure 1.4.

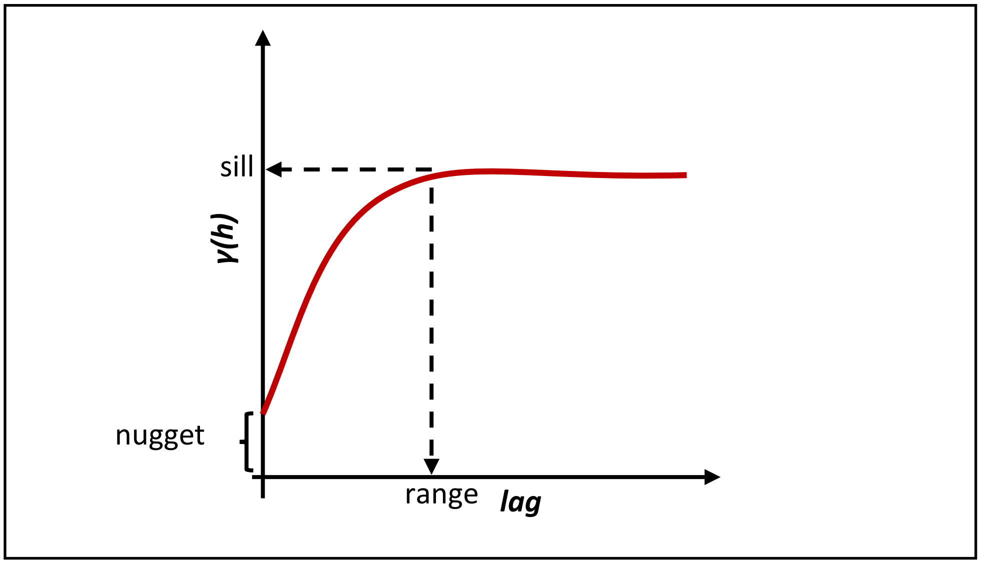

**Figure 1.4:** Example of a variogram plot showing the main parameters.

The *range* represents the distance at which the curve achieves the plateau or *sill*, which means that at that distance the data are no longer autocorrelated. The *sill* is the $\lim_{h\to\infty}\gamma(h)$, representing the variance of the random field. The *nugget effect* represents micro-scale variation or measurement error, and it reveals a discontinuity at the origin of the curve.

### 1.5.3 Variogram and intraparticle heterogeneity

Lyman (2011) prepared an artificial texture represented by three phases (a black one, a grey one and a white background) to explain how to apply the variogram in heterogeneity assessment. The texture was created based on squares randomly distributed with a fixed square size distribution. The squares were from 5 to 100 pixels in size, with a 90% passing size of 70 pixels for the black and grey phases. The area was distributed as follows: 35% black, 35% grey and 30% white, as shown in Figure 1.5a.

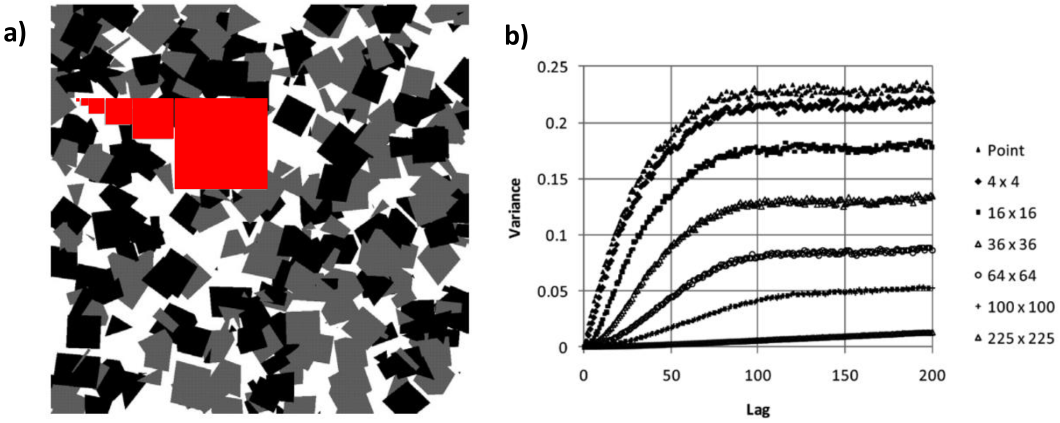

**Figure 1.5: a)** A 'non-nuggetty' texture of square grains at 35% in area for each phase (black and grey); **b)** Variograms of sample 'grade' for the black phase as a function of sample size.
Notes: 1. red squares show the sample size; 2. image is 1024x1024 pixels; 3. variograms are plotted down to the origin for all sample sizes (Lyman, 2011).

Figure 1.5b shows seven variograms calculated for the black phase on the artificial texture. Each of the variograms was generated using 10,000 randomly oriented sampling points and different sampling areas. The smallest sampling area is one pixel and the largest is a square of 225 x 225 pixels. The typical variogram curve can be observed in most of them. The *range* is approximately 70 pixels, and increases with increasing the sampling area. However, for the largest sampling area, the range cannot be observed. For this case, the variogram losses the ability of representing the structure. Regarding the *sill* parameter, it decreases for the variograms with larger sampling areas. The variation of the sill with the sampling area is presented in Figure 1.6.

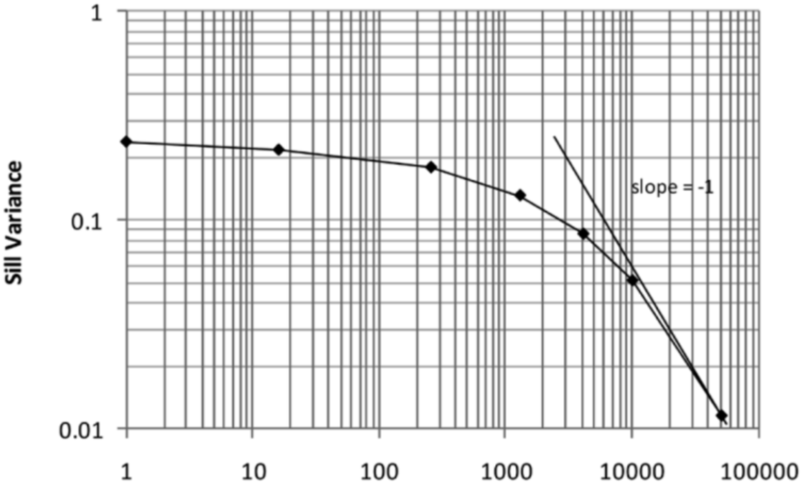

**Figure 1.6:** The *sill* variance as a function of the sample area for texture in Figure 1.5a (Lyman, 2011).

The theoretical analysis performed represents an example of how the variogram can be used in order to estimate the average size of the phase of interest, and also, how the resolution of the variogram decreases while increasing the sampling area.

In order to test how the shape of the variogram changes with the phase concentration, Lyman carried out the same procedure for a "low grade" texture with a black phase concentration of 1.62%, as presented in Figure 1.7a. This texture could be described as "nuggetty", with just a few squares of target phase. Figure 1.7b shows the variograms for this "nuggetty" texture.

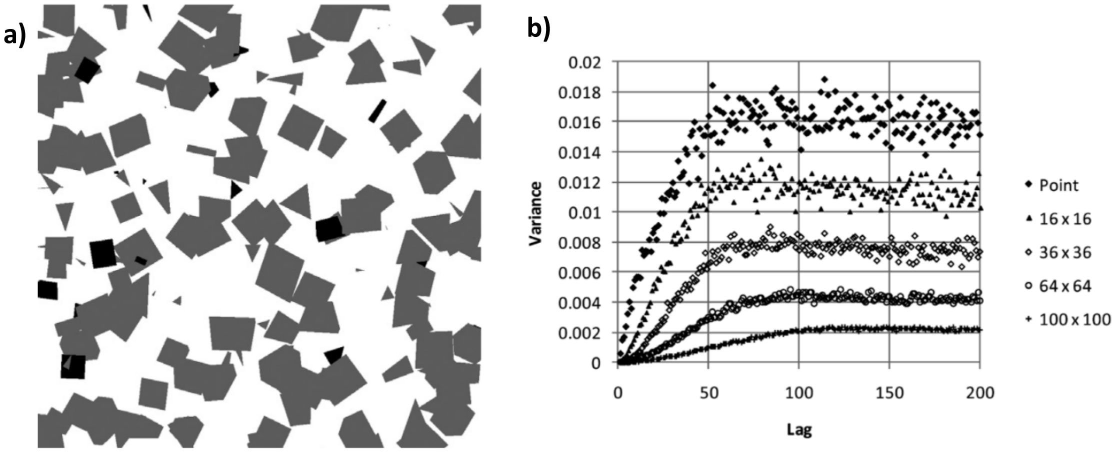

**Figure 1.7: a)** A 'nuggetty' texture of square grains at 1.62% black phase and 39% grey phase; **b)** Variograms of sample 'grade' for black phase as a function of sample size.
Notes: 1. image is 1024x1024 pixels; 2. the variograms are plotted down to the origin for all sample sizes (Lyman, 2011).

As can be observed in the Figure 1.7b the shape of the variograms do not change, and the *range* still represents the average size of the squares. The sampling area is an important variable for the variogram calculation. For the texture shown in Figure 1.7a, the variogram losses the ability to identify the structure and size of the black squares if the sampling area is larger than the squares. Figure 1.8 shows that for a sampling area of 100 x100 pixels, the first part of the curve cannot be observed. Therefore, the range of the variogram cannot be identified. For this large sampling area, samples cannot be taken at lags less than 100 pixels due to overlapping, and the first point in the variogram will be observed at 100. For values higher than 100, only a straight line is observed, which might be interpreted as a pure *nugget effect*, but clearly in this example is due to inappropriate sample size, therefore the trend is pure *sill* and not pure *nugget effect*.

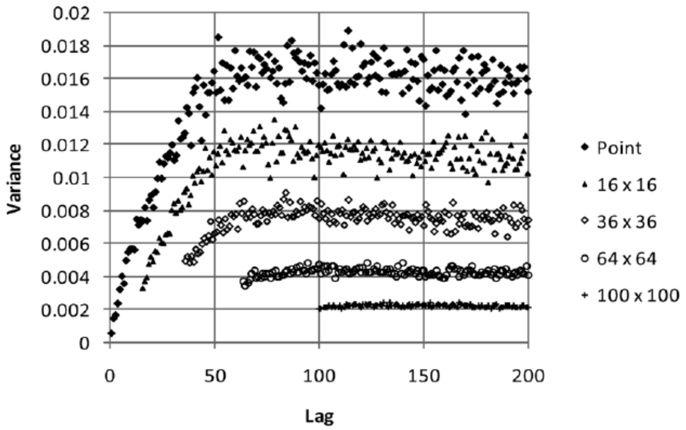

**Figure 1.8:** Experimental variograms of sample ‘grade’ for black phase as a function of sample size, representing only the observable part (Lyman, 2011).

It was also demonstrated that a *nugget effect* may be present due to intrinsic error of the assays. When the material is prepared for assay through crushing, grinding and splitting, a component of variance is introduced in the experimental data.

Two candidates were proposed for measuring in-situ heterogeneity in Lyman’s work: the *sill* and the *range* of the variogram. It was also mentioned that the variogram can be useful to identify structures present within different textures, such as a banded texture, where the variogram will show a periodic structure in the direction normal to the bands.

In order to apply the analysis suggested by Lyman to a particle size range that can be processed in a sensor-based sorter, a grade mapping technique is required, in which the grade at rock surface can be measured on run of the mine or primary crushed rocks (>10 mm). A brief review of the state of the art of rock mapping was carried out in order to evaluate the techniques available to perform such grade mapping.

## 1.6 Mapping techniques

Production of images showing elemental distribution has been an important development for a variety of fields. Table 1.2 lists the most common techniques used for surface mapping.

**Table 1.2:** Mapping techniques for determining the distribution of elements in solids (Friel & Lyman, 2006).

| | Method Name[a] | Input beam | Output signal | Lateral Resolution | Detection limit[b] | Remarks |
|---|---|---|---|---|---|---|
| X-Ray mapping methods | SEM/EDS | Electrons | X Rays | ≈1 µm[c] | 1 wt% | Routine specimen preparation, rapid |
| | EPMA/WDS | Electrons | X Rays | ≈1 µm | 0.1 wt% | Quantitative X-ray maps |
| | AEM/EDS | Electrons | X Rays | ≈2-5 nm | 1 wt% | Normal thickness TEM specimens |
| Other methods | AEM/PEELS | Electrons | Electrons | ≈1 nm | 0.1 wt% | Very thin TEM specimens required |
| | SAM/AES | Electrons | Electrons | ≈50 nm | 1 at% | Surface analysis, depth profiles |
| | SIMS | Ions | Ions | 1 µm | 100 ppb | Depth profiles, best element sensitivity |
| | PIXE | $H^+$, $He^{++}$ | X Ray | 2 µm | 0.01 wt% | Analytical sensitivity |
| | Atom probe | Atom extraction voltage | Ions | Atomic | One atom | Sharp needle specimen required |
| | Micro IR | Infrared light | Infrared light | 10 µm | N/A | Molecular spectroscopy |

[a] SEM/EDS: scanning electron microscope/energy-dispersive spectrometer. EPMA/WDS: electron probe microanalyzer/wavelength-dispersive spectrometer. AEM/EDS: analytical transmission electron microscope/energy-dispersive spectrometer. AEM/PEELS: analytical transmission electron microscope/parallel collection electron energy loss spectrometer. SAM/AES: Scanning Auger microscope/Auger electron spectrometer. SIMS: secondary ion mass spectrometer. PIXE: proton induced X-ray emission.

[b] Detection limits for maps have been estimated to be 10xgreater (worse) than single point analysis because of the limited dwell time per pixel.

[c] For low-voltage SEM/EDS the lateral spatial resolution can be as small as 0.1 mm.

All of them are designed to achieve high resolution and work with fine particles. Their main application is in texture analysis at the micro-scale. Most of the commercially available equipment use SEM/EDS to perform the surface mapping. Each company has its own image processing software and mapping algorithms, such as FEI QEMSCAN & MLA, Oxford INCAMineral, Tescan TIMA, and Zeiss Mineralogic Mining.

The procedures followed by these equipment for scanning the rock is similar for all companies. A regular grid is created over the particle surface and each grid point is analyzed in order to recreate the texture. Figure 1.9 shows an example of the grid generated during the mapping procedure followed by the MLA, which was designed at The University of Queensland in Australia.

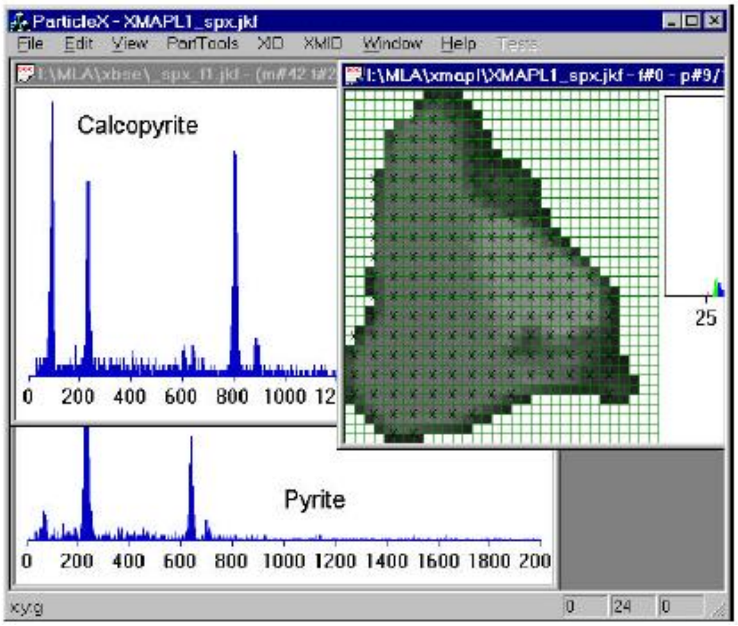

**Figure 1.9:** Regular grid used for surface mapping in MLA (Gu, 2003).

There are a few other techniques, such as Laser-induced Breakdown Spectroscopy (LIBS) and X-Ray Fluorescence (XRF) spectroscopy, that could be used to perform elemental analysis and surface mapping, but are not applied for such a high resolution.

An example of applying XRF to perform grade mapping applied in geology and mining is the XRF Core Scanner, in which pieces of drill-core sample are scanned along the main axis in order to track changes in chemical composition for major, minor and trace elements (Richter et al., 2006). The XRF Core Scanner was designed mainly to be used in sediments analysis, but now it is widely applied for different types of rocks.

The principle of X-Ray Fluorescence is widely explained in the literature. One of the best books available for this technique is '*Practical X-Ray Spectrometry*' (Jenkins & De Vries, 1969). To briefly summarize the principle behind this technique, an electron is expelled from an inner shell of an atom due to the influence of incoming X-Ray radiation. The vacancy generated is filled by an electron falling back from an outer shell. Electromagnetic radiation is emitted due to the energy difference between both shells, and this radiation is measured. The elements can be detected since each one has its own characteristic wavelength. To quantify the element concentration, the peak intensities in the XRF spectrum are used.

In the case of XRF spectroscopy, handheld devices are commercially available, which achieve accurate results for most of the elements such as copper, iron, zinc, and lead. The advantages of the

XRF devices are their portability and low price compared to the other mapping techniques presented above. The sampling area for these devices is in the millimetre size range, which is considerably larger than the sampling area offered for the equipment listed in Table 1.2. However, the sampling area offered for such XRF devices is small enough when analysing run of the mine or primary crushed rocks (>10 mm). Thus, the XRF handheld devices show the potential conditions to perform the variography analysis described above to run of mine or primary crushed rocks.

## 1.7 Summary

Sensor-based sorting is perceived a feasible solution for some of the most critical aspects of mineral production, such as energy and water consumption, fine waste generation and management, operating costs, and head grade decline. Sensor-based particle sorters have been successfully applied in other industries as well as for the processing of industrial minerals like calcite, rock salt, diamonds and some base and precious metal ores. To expand the application of particle sorting for metal sorting, appropriate sensors need to be developed or improved.

For an ore to be potentially sorted, a high degree of heterogeneity between rocks, in terms of the metal grade, is required. This implies that the potential for rejecting a large portion of waste or barren rocks, or alternately recovering a meaningful proportion of valuable rock, is present. This type of heterogeneity was defined, in this work, as interparticle heterogeneity.

Part of the sensors currently available rely on rock surface properties such as color, brightness, or chemical composition in order to estimate the bulk grade of the valuable mineral or metal. For instance, in an X-Ray Fluorescence (XRF) sorter, an elemental analysis is performed at the rock surface and this analysis is correlated with the elemental composition of the entire rock. The correlation does not only depend on how well the sensors can analyze the surface, but also on how well the surface correlates to the volume of the rock. Surface sensing is even more complex since only part of the rock surface is scanned in an actual sorter. Thus, the grade heterogeneity of each particle, defined as intraparticle heterogeneity in this work, controls the correlation in such a way that, the higher the grade heterogeneity within a particle, the poorer the correlation between surface and bulk grades.

Lyman proposed the *sill* and the *range* of the variogram as a measure of in-situ heterogeneity, here defined as intraparticle heterogeneity. In order to calculate the variogram, a variography analysis needs to be performed on the rock surface. The grade distribution of the rock surface is required to perform such analysis. The grade distribution can be obtained using a handheld XRF device.

## 1.8 Research objectives

The main objective of this work was to design and develop a method for rock surface mapping in order to assess intraparticle heterogeneity and to evaluate the correlation between surface grade and bulk grade for run of the mine or primary crushed rocks.

The following specific research objectives are proposed:

1) Design and develop a new method of XRF mapping of run of the mine or primary crushed rocks, and apply it to two porphyry copper ore samples.
2) Evaluate XRF mapping results applying univariate statistical analysis to characterize the copper and iron surface grade distributions and summarize the data obtained.
3) Analyze the correlation between surface grade and bulk grade for copper and iron, in order to evaluate the performance of XRF surface sensing and to assess intraparticle heterogeneity in one dimension for the selected samples.
4) Evaluate variography suitability for intraparticle heterogeneity assessment in two dimensions.
5) Design a method to graphically show the copper data collected in the XRF mapping.

## 1.9 Thesis organization

Section 2 describes how the surface mapping was performed along with an explanation of how the data was processed. Section 3 contains the results obtained in this study and their discussion, starting with the analysis of the scanning procedure. Then, the selected samples are characterized by visual inspection and by presenting their elemental composition. This characterization is followed by the analysis of the surface particle grade distribution for copper and iron, and the study of the correlation between surface and bulk grades. Finally, the heterogeneity assessment by applying variography is discussed along with the color mapping.

Section 4 presents the main conclusions of this work and Section 5 closes this thesis with recommendations for future work based on the results that were obtained and observations made during the study.

## 1.10 Relevance of this study

The research on this XRF scanning method for run of the mine and primary crushed rocks is of practical, industrial and basic scientific interest. The ability to determine elements grade distribution at the rock surface allows a deep understanding of how well the surface grade represents the bulk grade, and how to summarize the data obtained for further modelling of the process. This method could be incorporated into the assessment of the sorting potential of an ore when evaluating surface sensing techniques.  At the lab-scale, the direct practical application of this work is to help in the design and development of a robust procedure for sortability assessment for XRF sensor sorting. The results of the research will also help to develop improved sensing systems for sorting machines.

# 2. METHODOLOGY

## 2.1 Sample description

The porphyry copper ore samples used in this research were provided by Copper Mountain Mining Corporation from the Copper Mountain mine. The Copper Mountain deposit is described as an alkalic porphyry copper deposit with associated gold and silver. The deposit is divided in 6 pits, as follows: Pit 1, Pit 2, Pit 3, Ingerbelle, Virginia and Oriole. The ore samples for this research came from what is currently considered the Super Pit, which is the combination of Pit 1, 2 and 3. Figure 2.1 shows the respective locations of the Pits.

**Figure 2.1:** Super Pit image showing the location of Pit 1, 2 and 3 (*Copper Mountain Commemorative Book*, 2011).

Two ore types were tested, one from a low-grade zone (LG sample) and another from a high-grade zone (HG sample), weighing around 200 kg each. The LG sample came from what is considered a low-grade stockpile (0.1<% Cu<0.19). This stockpile represents the ore feed to the mill at the end of the mine life when the pit has exhausted the ore resource. The source of the LG sample is not clear since there was no tracking of the material source in the stockpile, it could come from Pit 2 or Pit 3. The HG sample was taken from a central location of a high-grade stockpile. This stockpile is filled when the primary crushing circuit is unable to process fresh feed, and this ore is used for short term grade control. The HG sample is a mixture of Pit 2 and Pit 3 ore.

Mineralization at Copper Mountain consists mainly of structurally controlled, multidirectional veins and vein stockworks. Four types of mineralization have been identified in the deposit: 1) disseminated and stockworks chalcopyrite, bornite, chalcocite and pyrite; 2) hematite-magnetite-chalcopyrite replacements and/or veins; 3) bornite-chalcocite-chalcopyrite associated with pegmatite type veins and 4) magnetite breccias. There is no clear correlation between mineralization types and pits but each pit is unique in terms of relative quantities and character of mineralization type (Holbek, Richard, & Frost, 2015)

In Pit 2, mineralization is structurally controlled with copper occurs mainly as chalcopyrite in trending veins, vein stockworks and fracture fillings, which would be a mixture of type (1) and (2) of the description presented above. Some disseminated mineralization is present in this Pit. However, copper in Pit 3 occurs as bornite and chalcocite, (mineralization type (3)). In this case, sulphide mineralization is found in veins, veinlets and disseminated grains (Holbek et al., 2015).

## 2.2 Sampling procedure

Five rocks from each ore type were selected. Rocks of around 10 cm in length were selected in order to have enough area to test an average of 100 points per face. The samples were washed with tap water to remove the dust found at the surface. This is an important step of the sorting process since XRF penetration is limited to nanometers, thus the presence of dust could lead to misreading of the elemental composition. After washing, the largest four faces of each rock were labeled for surface XRF scanning.

## 2.3 XRF mapping

Compositional analyses were performed by a handheld X-ray fluorescence (XRF) (Olympus Innov-X Alpha 6000 XRF Analyzer) equipped with an energy dispersive spectrometer. Equipment spot size is estimated by the manufacturer to be in the order of 10 mm in diameter, which implies an analysis area of 0.8 $cm^2$. The count time was 30 s for all the elements measured including: Ni, Cu, Co, Mo, Pb, Zn, Fe, Ag, Ba, Cd, Cr, Hg, Mn, Sb, Sn, Ta, Ti, Zr. The elements concentration was determined using the Soil mode for Standard Elements.

## 2.4 Wet chemical analysis and fire assay

After XRF testing, the samples were crushed and pulverized. A representative portion of each rock was analyzed with the same handheld XRF device, and sent for gold analysis by fire assay with atomic absorption finish (AAS), and multi-element analysis by Aqua Regia digestion followed by inductively coupled plasma atomic emission spectroscopy (ICP-AES). The assay results from the XRF and ICP were compared in order to test the accuracy of the XRF handheld device (see Appendix B – Wet analysis and XRF assays comparison)

## 2.5 Data analysis

### 2.5.1 Exploratory data analysis and distribution fitting

MATLAB® software (MathWorks, Nattick, MA, USA) was used to calculate the main statistical parameters associated with copper and iron grade for each face, which were summarized in standard box and whisker diagrams. The copper and iron grades were selected due to their predominance over the other detectable elements. These elements were also part of the chalcopyrite and bornite minerals which are the main sources of copper for this ore.

Histograms of raw data were prepared to show distribution. Due to the non-normal behaviour of the raw data, a Box-Cox transformation was carried out to identify the distribution by applying the following equation (Box & Cox, 1964):

$$z^{*} = \begin{cases} \dfrac{(z+m)^{k}-1}{k} & for\ k \neq 0 \\ \log(z+m) & for\ k = 0 \end{cases} \tag{5}$$

where *min(z)+m>0*. Also, the normality test of the lognormal and Box-Cox transformed data was performed.

### 2.5.2 Particle grade prediction

Regression analysis was performed to compare copper and iron surface grades to copper and iron bulk grades, respectively. The arithmetic mean, geometric mean and median were calculated and compared to bulk grade in order to evaluate which one is the best representative parameter for the rock surface.

### 2.5.3 Variography

For the experimental variogram calculation, described in the Literature Review Section, the classical equation to estimate the autocorrelation is defined by the semi-variance, as follows:

$$\gamma(h) = 0.5 \cdot (z_{x} - z_{x+h})^{2} \tag{6}$$

where $z_x$ is the observed value at location *x* and $z_{x+h}$ is the observed value at another point at a distance *h*. Figure 2.2 shows graphically the relation between the variables, in two dimensions.

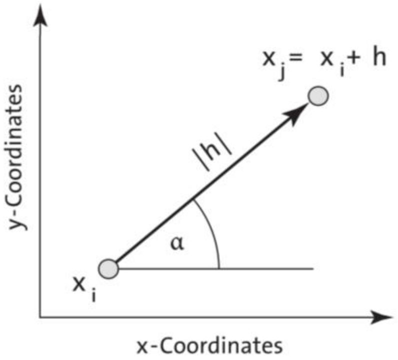

**Figure 2.2:** Separation of vector *h* between two points (Trauth, 2007).

#### 2.5.3.1 Omnidirectional variogram

A MATLAB script was written in order to evaluate the spatial dependency of copper and iron grade in all the XRF mapped data. Here, an example for one face is used to present the script and understand the methodology selected. To clarify the terminology involved, the length of the separation vector *h* is called the *lag distance* or simply the *lag*. The script was focused on the calculation of the omnidirectional variogram, which means that all the possible directions were combined in a single variogram, and the separation distance represented the only variable.

The input variables for this script were location (x,y), and copper grade (Cu) or iron grade (Fe). The example script presented below corresponds to the copper analysis, which was the same one used for iron, but the variable Cu was replaced by Fe. The script was constructed through the following steps:

Step 1: The observations were grouped in pairs and the matrix of separation distances "*D*" between the observation points was calculated. Then, the experimental variogram "*G*" was calculated as half of the squared differences between the observed values. The lower triangular portions of *D* and *G* arrays were used to plot the experimental variogram, known as the *variogram cloud* (see Figure 2.3). This part of the script is shown below:

```
[X1, X2] = meshgrid(x);
[Y1, Y2] = meshgrid(y);
[Cu1, Cu2] = meshgrid(Cu);
D = sqrt((X1 - X2).^2 + (Y1 - Y2).^2);
G = 0.5*(Cu1 - Cu2).^2;
indx = 1:length(z);
[C,R] = meshgrid(indx);
I = R > C;
plot(D(I),G(I),'.' )
xlabel('lag distance (mm)')
```

*ylabel('semivariance')*

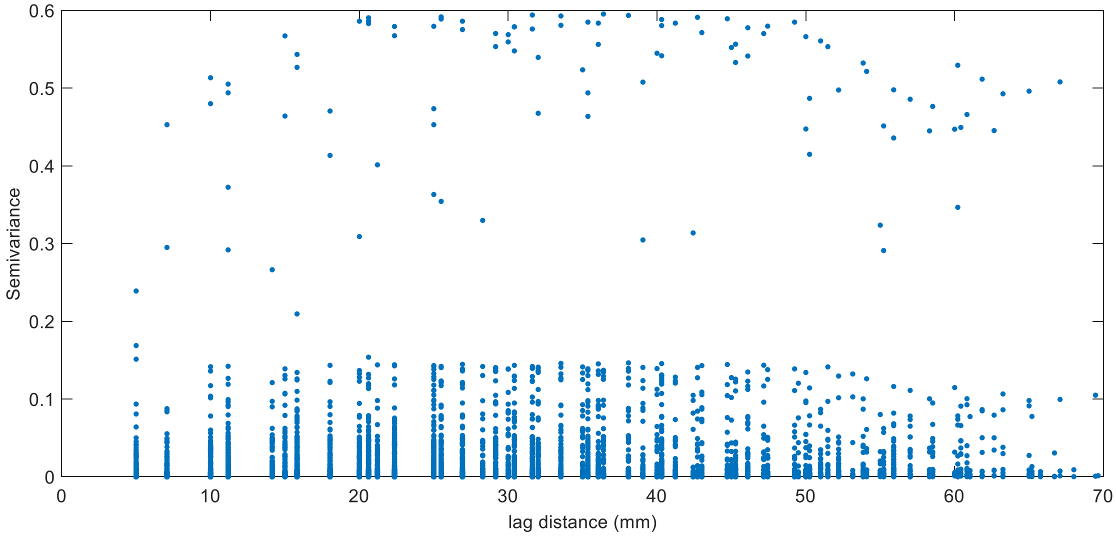

**Figure 2.3:** Variogram cloud for face H-5-2 showing semivariance (half the squared difference between pairs of observations) as a function of the lag distance (separation distance between two components of a pair).

The variogram cloud is not a good tool to identify spatial correlations, however, it could be useful to find outliers or anomalies. This is the reason for preparing the variogram estimator and its model (Trauth, 2007).

Summarizing the central tendency of the experimental variograms is the main target for the variogram estimator. Certain distance classes or bins need to be defined as part of the classical variogram estimator calculation. In this case, the decision was straightforward since sampling had been carried out on a regular grid of 5 x 5 mm and, for a better resolution, half of the grading distance was used, 2.5 mm. Figure 2.4 illustrates the classification for the separation distance based on the lag value.

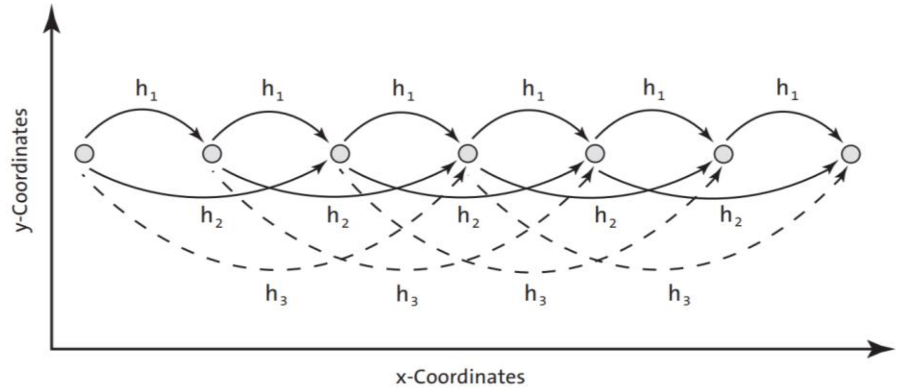

**Figure 2.4:** Classification of the separation distances for observations that are equally spaced. The lag interval is $h_1$, and $h_2$, $h_3$ etc. are multiples of the lag interval (Trauth, 2007)

The variogram estimator was calculated according to the following equation (Trauth, 2007):

$$\gamma_E(h) = \frac{1}{2 * N(h)} \cdot \sum_{i=1}^{N(h)} (z_{xi} - z_{xi+h})^2 \qquad (7)$$

where *N(h)* is the number of pairs with the lag interval *h* (2.5 mm).

After setting the lag value, a distance limit needs to be defined on the variogram analysis to avoid erratic behaviour due to scarce data at long distance. According to literature, there is no standard procedure in order to define the distance limit. The only statement is that the fewer the pairs, the less reliable (Clark, 1987). Therefore, the distance limit should be defined based on the number of pairs for each lag. In this study, three quarters of the maximum distance was selected as distance limit.

Step 2: The lag value was set at 2.5 mm and the limit distance was calculated as three quarters of the maximum distance. The separation distances were then classified and the classical variogram estimator was calculated, where "*SEL*" was the selection matrix defined by the lag classes in "*LAG*", "*DE*" was the lag mean, "*PN*" was the number of pairs and "*GE*" was the variogram estimator. The last part of the script is shown below:

```
lag= 2.5;
hmd = max(D(:))*0.75
hmd = 52.23
max_lags = floor(hmd/lag)
max_lags =20
LAGS = ceil(D/lag);
for i = 1 : max_lags
SEL = (LAGS == i);
DE(i) = mean(mean(D(SEL)));
```

```
PN(i) = sum(sum(SEL == 1))/2;
GE(i) = mean(mean(G(SEL)));
end
```

#### 2.5.3.2 Geometric and zonal anisotropy

Directional variograms were calculated in two perpendicular directions for some faces in order to explain part of the trends observed in the omnidirectional variogram. This calculation was performed step by step in Microsoft Excel without using the script in order to verify the obtained results. The directions were selected by visual inspection of the rock surface, identifying the copper veins and selecting one perpendicular and one parallel to the vein direction.

## 2.6 Color mapping

The two-color maps were constructed using MATLAB® software (MathWorks, Nattick, MA, USA). The mapping data were arranged in a matrix by following the known location for each point, and the Contour function in Matlab was applied to the matrix for each face.

The maps were developed using the Matlab function: Contour in filling mode. Selection of grade level for contour line construction is explained in the Results and Discussion Section. Photos were edited using the GNU Image Manipulation Program.

# 3. RESULTS AND DISCUSSION

## 3.1 Surface XRF mapping procedure

This section presents the method developed for XRF mapping of run of the mine rocks and its application to two porphyry copper ore samples. As explained in Methodology Section, the rocks mapping was performed using an XRF handheld device. Figure 3.1 shows the system configuration and sampling design, as well as an example of the points sampled for one rock face.

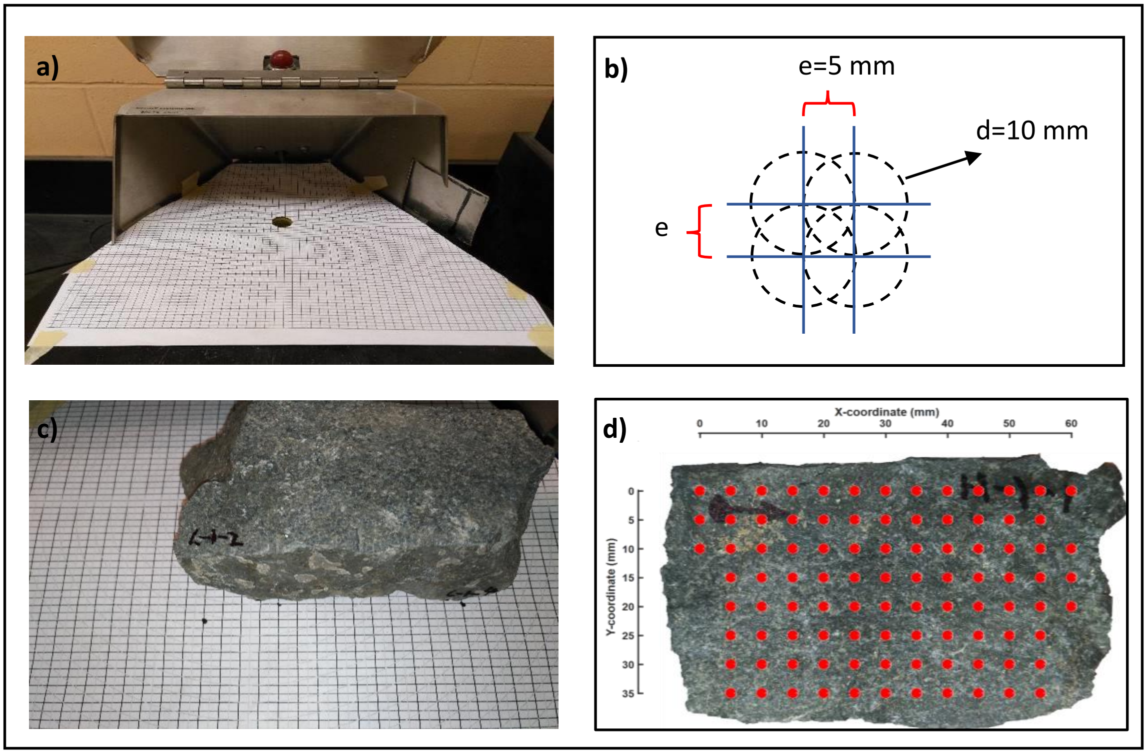

**Figure 3.1: a)** Benchtop workstation of the XRF device with grid for position tracking; **b)** scheme of sampling configuration, showing spacing grid (*e*) and equipment spot size (*d*); **c)** rock sample during testing; **d)** points sampled for one rock face.
(Note: the red dots indicate the center of the sampling position, not the actual area sampled).

Ten rocks were analyzed, 5 rocks from the HG sample and 5 rocks from the LG sample, with a total of forty faces being mapped. The criterion for rock selection was particle size, with rocks in the range of 3 cm to 10 cm. The code selected for labeling was X-Y-Z, where X represents the identification of the sample, H for HG sample and L for LG sample, Y represents the rock number, from 1 to 5, and Z represents the face number, from 1 to 4.

The entire area of each rock face was analyzed spot by spot. For location tracking during testing, a regular grid, with a spacing of 5 x 5 mm, was attached to the table of the benchtop workstation of the XRF device, as shown in Figure 3.1a. The spacing of the grid was selected to cover every point at the rock surface based on the equipment spot size. Although there was sampling area overlapping with this configuration, the grid spacing was selected in order to test every mineral grain at the rock surface (see Figure 3.1b).

The larger faces of each rock were selected. The flatness of the rock surfaces was an important variable while testing, since this was crucial for precision of sampling location tracking. For rough rock surfaces, a small external device was used to fix their position. The location was tracked in *x* and *y* directions, to ensure precise positioning (see Figure 3.1c). The reading number and the coordinates *x* and *y* were recorded, and then the information was compiled. There was an inherent error while tracking the position since the rock was manually moved between analyses. Table 3.1 shows the number of sampling points and the estimated area per rock face, as well as the mass of each rock.

**Table 3.1:** Summary of mapping results, showing estimated area, number of sampling points for each rock face and mass of each rock.

| **Sample ID** | **Face ID** | **Area ($mm^2$)** | **# Sampling points** | **Mass (g)** | **Sample ID** | **Face ID** | **Area ($mm^2$)** | **# Sampling points** | **Mass (g)** |
|---|---|---|---|---|---|---|---|---|---|
| *H1* | *H-1-1* | 2,950 | 95 | | *L1* | *L-1-1* | 3,825 | 128 | |
| | *H-1-2* | 2,425 | 76 | | | *L-1-2* | 2,825 | 90 | |
| | *H-1-3* | 1,100 | 29 | | | *L-1-3* | 1,625 | 46 | |
| | *H-1-4* | 2,075 | 62 | | | *L-1-4* | 1,425 | 39 | |
| | *Total* | 8,550 | 262 | 212.4 | | *Total* | 9,700 | 303 | 280.7 |
| *H2* | *H-2-1* | 2,500 | 66 | | *L2* | *L-2-1* | 3,450 | 52 | |
| | *H-2-2* | 1,850 | 55 | | | *L-2-2* | 2,650 | 85 | |
| | *H-2-3* | 2,100 | 66 | | | *L-2-3* | 1,925 | 52 | |
| | *H-2-4* | 1,125 | 29 | | | *L-2-4* | 725 | 17 | |
| | *Total* | 7,575 | 216 | 187.0 | | *Total* | 8,750 | 212 | 240.1 |
| *H3* | *H-3-1* | 3,375 | 110 | | *L3* | *L-3-1* | 3,250 | 106 | |
| | *H-3-2* | 3,150 | 106 | | | *L-3-2* | 2,500 | 78 | |
| | *H-3-3* | 2,500 | 78 | | | *L-3-3* | 1,725 | 50 | |
| | *H-3-4* | 2,900 | 94 | | | *L-3-4* | 1,775 | 50 | |
| | *Total* | 11,925 | 388 | 406.2 | | *Total* | 9,250 | 284 | 351.6 |
| *H4* | *H-4-1* | 3,175 | 103 | | *L4* | *L-4-1* | 3,625 | 120 | |
| | *H-4-2* | 3,375 | 89 | | | *L-4-2* | 3,575 | 114 | |
| | *H-4-3* | 2,475 | 77 | | | *L-4-3* | 2,475 | 78 | |
| | *H-4-4* | 2,375 | 73 | | | *L-4-4* | 3,175 | 103 | |
| | *Total* | 11,400 | 342 | 485.1 | | *Total* | 12,850 | 415 | 643.5 |
| *H5* | *H-5-1* | 3,175 | 100 | | *L5* | *L-5-1* | 4,650 | 158 | |
| | *H-5-2* | 3,250 | 106 | | | *L-5-2* | 3,300 | 99 | |
| | *H-5-3* | 2,575 | 81 | | | *L-5-3* | 4,050 | 136 | |
| | *H-5-4* | 1,975 | 59 | | | *L-5-4* | 3,175 | 103 | |
| | *Total* | 10,975 | 346 | 429.5 | | *Total* | 15,175 | 496 | 683.7 |

The smallest face analyzed had an area of 725 mm$^2$ and the largest one was 4650 mm$^2$, which implies a face of approximately 25 mm and 70 mm width length, respectively. In total, 3246 analyses were performed in this study, with an average of 325 analyses per rock. The rate, expressed in analyses per hour, was 60. Based on the analyses performed per hour and the average of analyses per rock, the total testing time per rock was estimated to be 6 hours.

The rock face area shown in Table 3.1, represents an estimation of the total area of each face, not of the actual area tested. The estimation was carried out based on the total number of analyses per rock, as well as the location at where the analyses were performed. One of the limitations of the procedure was that it was impossible to cover the entire face of the rocks. The analysis was not performed if the equipment spot size was not fully covered by the rock. Because of this, when approaching the edge of each rock, for reliable testing, a small portion of the total rock area was not analysed. The effect of this decision can be observed in Figure 3.1d, where part of the area close to edge was not tested. Furthermore, because of the overlapping in sampling areas, small areas at the center of the rock were tested four times (see Figure 3.1b). This overlapping effect could have been avoided if the XRF device had had a rectangular beam. In the XRF device used, the equipment spot size was fixed and it could not be adjusted as in other similar devices, which are normally assembled with a collimator that can narrow the XRF beam.

The resolution achieved, an analysis every 5 mm, was considered acceptable for assessing ore sorting potential. The sensor-based sorters are designed to handle rocks in the particle size range of 20 mm to 250 mm. There is a trade-off between the resolution achieved and the time invested in analysis. In this case, any conclusion that can be generated at a particle size below 10 mm could be considered *a priori* not useful for sensor-based sorting technology.

The mapping technique developed was not validated or compared with other mapping techniques including elemental analysis. However, the data obtained was validated by visual inspection. Features of each rock face such as vein position, or zones rich in pyrite or other iron rich zones were compared to the data obtained. For example, it was expected that the points with higher copper grade where located at the chalcopyrite rich veins.

Two options are proposed for the validation of the mapping technique. The first one is to prepare and to test a synthetic rock face, composed by more than one zone, with each zone made by rock powder of known concentration of the valuable mineral. The second one is to assemble small (2 x 2 cm) rectangular sections, that can be tested using the mapping technique presented in this study.

The sections can then be disassembled and sent for grade mapping analysis by other mapping techniques (e.g. scanning electron microscope (SEM) with energy disperse spectroscopy (EDS)).

## 3.2 Sample characterization

The mineralization of the selected rocks matched with the description presented in the Methodology Section. Chalcopyrite and bornite were the copper minerals observed in most of the rocks.

For high grade samples (HG), in rocks H-1 and H-5, fine grained black mineral was observed, which possibly was magnetite, along with some visible strands of chalcopyrite and disseminated pyrite, with a concentration estimated from 1 to 5% by weight. In rock H-2, disseminated pyrite, about 10 to 15% by weight, with stockwork texture containing bornite and chalcocite was observed. Rocks H-3 and H-4 were rich in pyrite with chalcopyrite mineralization.

Regarding low grade samples (LG), rocks L-1 and L-2 were similar, with low amounts of pyrite mineralization, and no observed copper minerals. In rock L-3, a brown mineral was seen that may be limonite or hematite, and pyrite mineralization in the range of 1 to 5%. In rock L-4 high pyrite and chalcopyrite mineralization were observed on two faces. On the other two faces, neither pyrite nor chalcopyrite were observed. Finally, in rock L-5, pyrite mineralization was low (<1%), and copper minerals were not observed in this rock.

Multi-element ICP analysis and fire assay results are shown in Appendix A – Elemental composition of each rock. Table 3.2 shows the elements that are considered the most relevant for this work.

**Table 3.2:** Concentration of the most relevant elements for each rock.

| ***Element*** | ***Unit*** | ***SAMPLE ID*** | | | | | | | | | |
|---|---|---|---|---|---|---|---|---|---|---|---|
| | | ***H1*** | ***H2*** | ***H3*** | ***H4*** | ***H5*** | ***L1*** | ***L2*** | ***L3*** | ***L4*** | ***L5*** |
| *Au* | *ppm* | 0.005 | 0.050 | 0.023 | <0.005 | 0.026 | 0.088 | <0.005 | 0.008 | 0.073 | 0.013 |
| *Ag* | *ppm* | 0.6 | 1.4 | 0.7 | 0.3 | 0.6 | 0.7 | <0.2 | 0.3 | 0.4 | 0.2 |
| *Cu* | *ppm* | 1975 | 4540 | 2492 | 707 | 1555 | 1920 | 67 | 981 | 1185 | 490 |
| *Fe* | *%* | 4.37 | 5.04 | 2.54 | 5.50 | 6.29 | 1.14 | 0.65 | 5.26 | 6.17 | 0.73 |
| *S* | *%* | 2.33 | 3.48 | 1.40 | 1.91 | 0.95 | 0.42 | 0.09 | 2.60 | 0.67 | 0.20 |

Relatively low gold and silver grades were detected on both samples. Copper grades vary from 67 to 4540 ppm. The higher copper grades were observed in the high-grade samples (HG). There was a high variability in the iron concentration, and no direct correlation was observed between iron and copper or sulfur and copper.

## 3.3 Surface particle grade distribution analysis

In this section, the results from the univariate statistical analysis are presented, with the aim of evaluating how well the experimental data fits to the most common data distribution models used in geochemistry, namely normal and lognormal. As mentioned before, only copper and iron grade were analyzed, since they are part of the valuable minerals of the ore used in this work, chalcopyrite and bornite.

The first step in the data analysis, recommended in the literature, is to carefully study the distribution of the measured variable. There is more than one approach to studying the data distribution, but the most common is by using graphs in order to have a good one-dimensional insight into the data structure. Typical graphs include the histograms, the density trace, the boxplot and one-dimensional scattergram.

The main objective of this first step is to evaluate if the data distribution follows a normal distribution. Many of the classical statistical tests assume normal data distribution. For example, the most common parameters used to measure the central tendency and dispersion of the data, arithmetic mean and standard deviation, respectively, assume normal distribution.

Real world data are rarely as well-behaved as assumed by classical statistical tests. As an example, in mining and geology, the data used for resource estimation rarely follow a normal distribution. The presence of some samples with unusual high concentrations of valuable metal is a very common characteristic of such data set. Thus, the data distribution is strongly skewed.

In a much broader aspect, geochemical data have a spatial dependence and, in general, are not normally distributed. Sampling, sample preparation and chemical analysis have many potential sources of error, that can generate unusual low or high elemental concentrations affecting the data distribution analysis. In addition, the precision of the analysis can change with the element concentration and the chemical analysis technique selected (Reimann & Filzmoser, 2000).

### 3.3.1 Copper

For this work, box and whisker plots were selected as a first approach in order to characterize the copper grade distribution for the HG and LG samples. Figure 3.2 and Figure 3.3 show the box and whisker plots for the data generated by the mapping technique developed in this work. The data is grouped by face and rock.

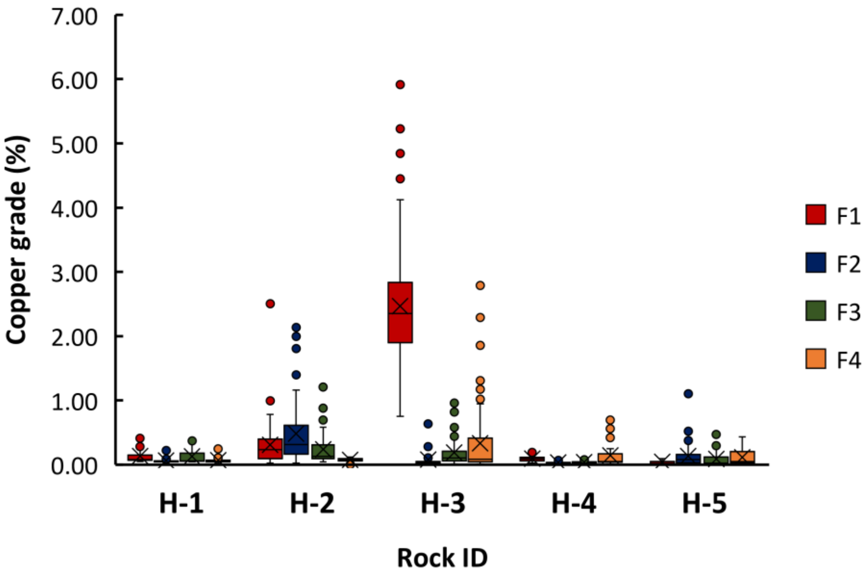

**Figure 3.2:** Box and whisker plots of copper grades for HG sample. Note: F denotes face.

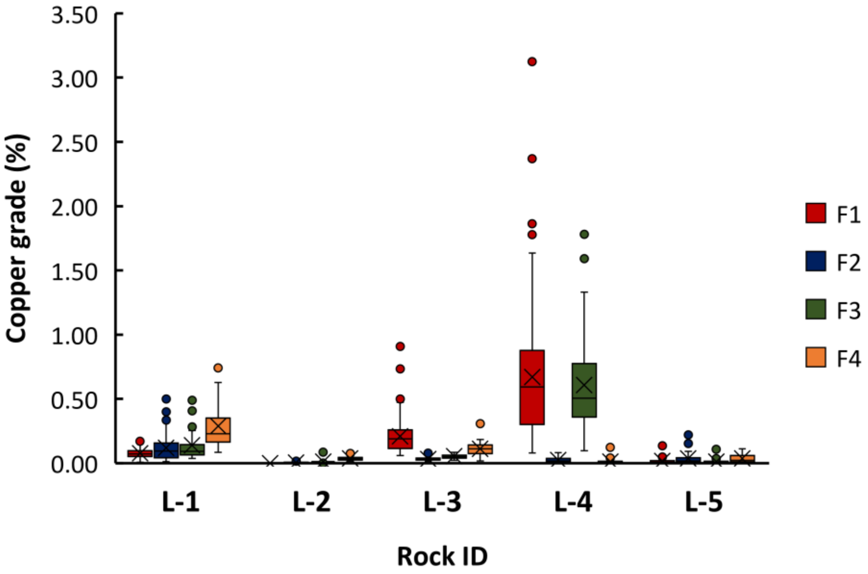

**Figure 3.3:** Box and whisker plots of copper grades for LG sample. Note: F denotes face.

As can be observed in Figure 3.2, for rocks H-1, H-4 and H-5, copper grades at the rock surface were lower than 1%, with most of the values located below 0.25%. For these rocks the copper grades of the faces were similar. However, the range of values observed for rocks H-2 and H-3 were higher than the others (H-1, H-4 and H-5), and there was a greater difference between faces within these two rocks. For example, for rock H-3, the minimum copper grade measured on face 1 was higher than the maximum copper grade measured in face 2. This difference indicates a degree of intraparticle heterogeneity for this rock, which is relatively high when comparing to the other rocks. The maximum copper grade value measured for HG sample was 5.9%, and it was measured in face 1 for sample H-3.

Furthermore, it can be observed in Figure 3.2 that the majority of the data were located on the lower side of each box, and the average was higher than the median for almost all the faces. In other words, the data were right skewed.

Regarding the LG sample, as shown in Figure 3.3, the copper grade values measured were, on average, lower than those for the HG sample. Copper was not detected on face 1 of rock L-2, and low concentrations were measured for the other faces of the same rock. This is a clear indication that this rock may be classified as waste. Low copper grades were found for rock L-5, with the copper grade distribution between faces located within the same range. The copper grades for rocks L-1 and L-3 were similar, with the median for each face located at 0.25%. Higher values of copper grades were detected in rock L-4, which had two faces with high copper grade (> 0.25%), and two faces with low copper grades (< 0.25%). The distribution for all the faces were right skewed, as was found for the HG samples.

Outliers were identified for almost all the faces analyzed for the HG and LG samples. These outliers were not discarded for further analysis since they were considered part of the grade texture of the rock, and were associated with zones of high concentration of copper minerals. The presence of outliers was further evidence that the data were right skewed for both the HG and LG samples. This observation indicates that the copper grade distribution may not follow a normal distribution model.

An important variable that needs to be considered when comparing the data for different rocks and faces, is the total area for each face. It could be assumed that, the larger the face area, the higher the data spread. In order to evaluate the effect of the total face area on the spread of the copper grade distribution, the coefficient of variation (CV) for each face was calculated. The faces were grouped into bins of equal area, and the CV of each bin was calculated as the average of the CV for each face. Figure 3.4 shows the correlation between face area and CV for both samples combined. The average area and CV for the bins were plotted.

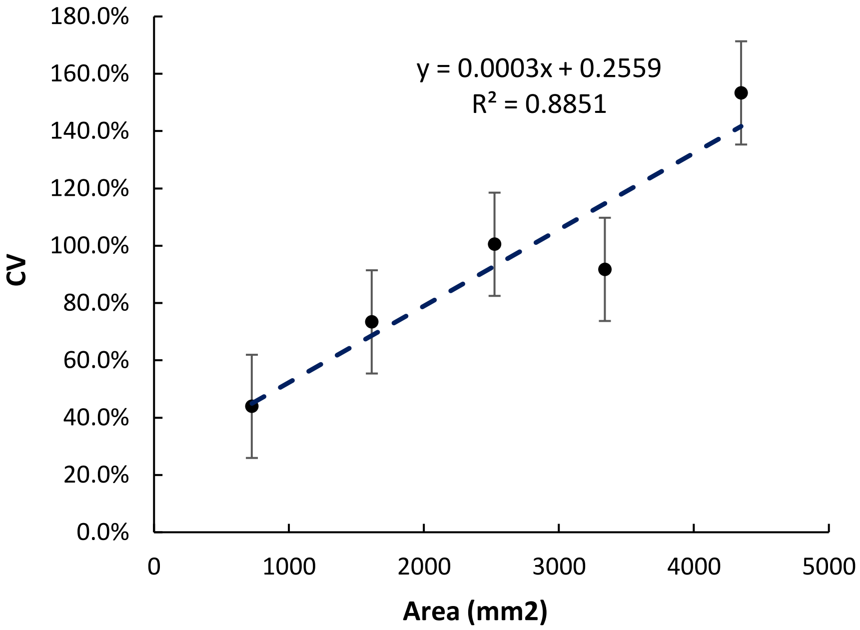

**Figure 3.4:** Correlation between face area and coefficient of variation (CV) of copper grade for HG and LG samples combined.

From Figure 3.4, it can be observed that, with increasing face area, the data dispersion was higher, which was reflected in a higher coefficient of variation. The standard deviation was not plotted for this analysis, since the objective was to determine the relationship between face area and copper grade distribution, and the standard deviation is highly influenced by the average grade of each rock. An important observation from Figure 3.4 is that for all the samples the coefficients of variation were higher than 40%. Such high coefficients are not common in normal distributions. This observation indicates that the copper grade distribution may be non-normal.

Repeatability tests were performed with the handheld XRF to determine how much of the variability detected in the experimental data was due to the method of analysis. The copper grade of a rock sample was measured 8 times at the same spot under identical conditions, and a coefficient of variation of 2.11% for copper was obtained. This low value shows that the dispersion found at the rock surface was mainly due to the rock heterogeneity and not to the method of analysis used.

Based on the results discussed above, it can be concluded that the data distribution was right skewed, with outliers at high grades, and with relatively high variability of copper grade within each face. For further analysis, an example of a histogram graph is shown in Figure 3.5 for rock H-4 face 1. The shape of the distribution in the histogram for this face is typical of other faces. Thus, this face was selected to display and discuss the results presented in this section.

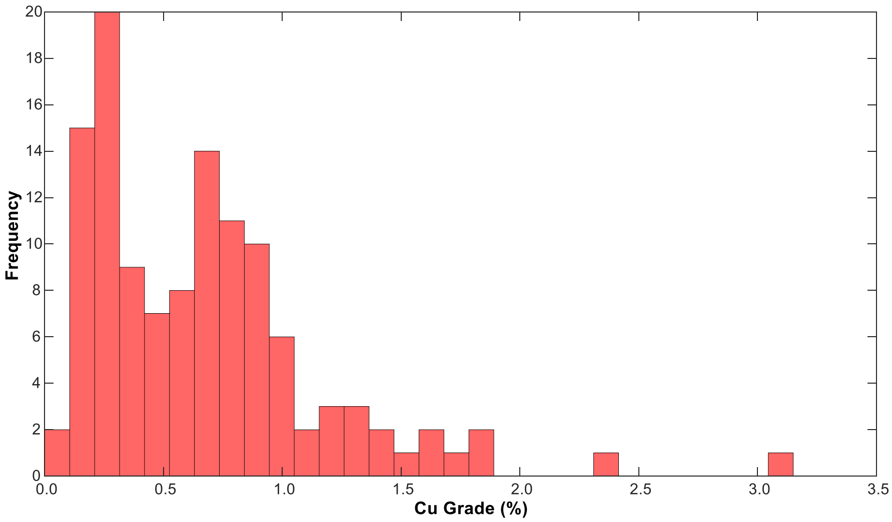

**Figure 3.5:** Histogram of copper grade for rock H-4, Face 1.

The histogram in Figure 3.5 was produced from 103 observations. The graph shows that the data distribution was right skewed. There was a high concentration of data at low copper grades (lower than 0.5%), and a long tail to the right. The majority of values were located in the low-grade range (lower than 1%), with very few values located in the high-grade range (higher than 1%). The data distribution was centered around 0.5% with high variability, given that the approximate range reached 3%. In this case, a bimodal trend can be observed.

In order to summarize the shape of the data distribution for the other samples, Figure 3.6 and Figure 3.7 show the histograms for the skewness and kurtosis calculated for each face, respectively.

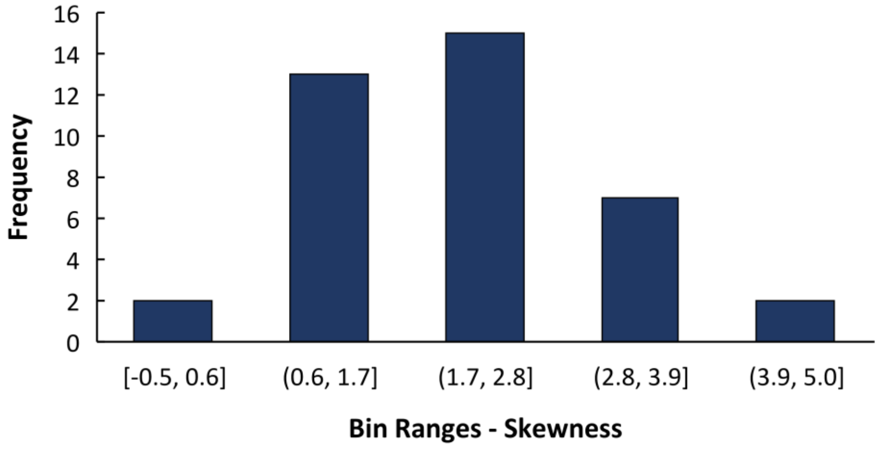

**Figure 3.6:** Skewness histogram for copper data, with 38 faces being analyzed.

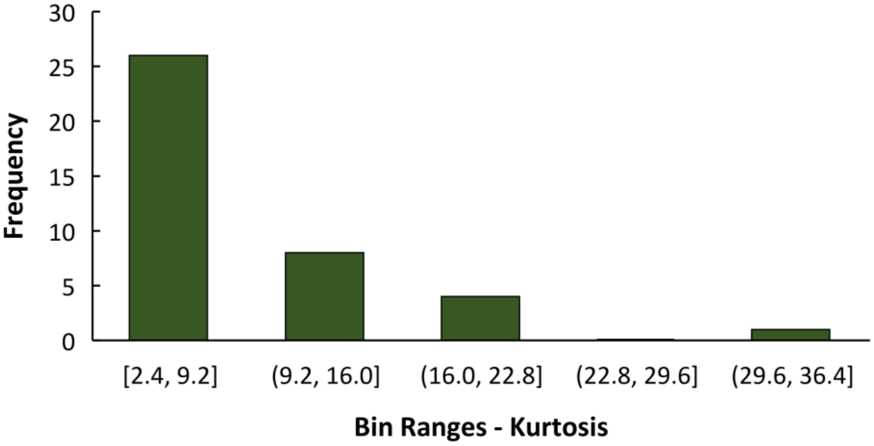

**Figure 3.7:** Kurtosis histogram for copper data, with 38 faces being analyzed.

Data sets with a high proportion of measurements below detection levels are very difficult to treat. In cases where there is a high number of values below detection limits (e.g. >25%), there is no chance to compare results with other data sets (Reimann & Filzmoser, 2000). The rock 2, face 1 and face 2 were not included in skewness and kurtosis histograms, as well as in the following analyses, since more than 25% of the measurements were below the detection level of the XRF device. In all the other cases, where only a few measurements were below the detection limit, these were set to one half of the detection limit to allow the use of these samples for further statistical analysis.

As can be observed in Figure 3.6, most of the data distributions had a positive value for skewness, which means that the data distributions were right-skewed. There were two faces, rock H-2 face 4 and rock L-2 face 4, that had a skewness value close to zero, which is the value expected for normal distributions. Both faces had small analyzed areas, with a total number of measurements of approximately 30. This indicates that the face area may affect the shape of the distributions.

Figure 3.7 summarizes the kurtosis values calculated for each face shown in a histogram. When compared to skewness, kurtosis measures a different type of departure from normality by indicating the extent of the peak, or the degree of flatness near its center. For a normal distribution, a kurtosis value close to 3 is expected. The faces analyzed showed a high kurtosis value when compared with the value of a normal distribution. Distributions with a kurtosis higher than 3 are called *leptokurtic*. Any distribution within this category is associated with thick tails and very thin and tall peaks.

Based on the evidence shown above including high coefficient of variation, positive skewness, and kurtosis higher than 3, it was decided to perform a normality test for each face. The Anderson-Darling test was carried out in order to test whether there was a departure from normality or not in the data sets (Anderson & Darling, 1954). Table 3.3 summarizes the results obtained after the application of the Anderson-Darling test for normality. The normality test results for each face are presented in Appendix C – Summary of Anderson-Darling normality test results – copper.

**Table 3.3:** Anderson-Darling test results for raw copper data.

| | **Raw data** |
|---|---|
| ***Total faces analyzed*** | 38 |
| ***Positive faces*** | 2 |
| ***%Positive faces*** | 5% |

According to the results obtained from the normality test, the null hypothesis was approved only for two faces, which means that in the data for these 2 faces no significant departure from normality was found. The null hypothesis was rejected at a 5% significance level for the other 36 faces. Figure 3.8 shows the normal probability plot for rock H-4 face 1, whose histogram was already shown in Figure 3.5. The two faces with positive results correspond to the same two faces mentioned before (rock H-2 face 4 and rock L-2 face 4), which present skewness close to zero, kurtosis close to 3 and lower coefficients of variation.

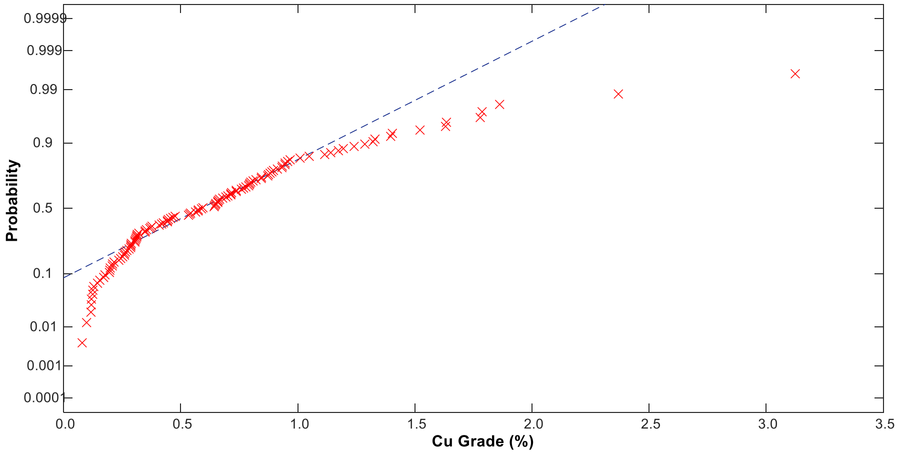

**Figure 3.8:** Normal probability plot for copper grades of rock H-4 face 1.

The departure from normality was measured mainly for low copper (< 0.25%) and high copper grades (>1%), as can be observed in the example shown in Figure 3.8. According to the statistical tests applied, only data sets with few observations, less than 30, showed not significant departure from normality at a 5% significance level.

Normality of geochemistry data is widely discussed in the literature. Large data sets from regional geochemical and environmental data have been tested for normal distribution. In general, almost all the cases showed non-normal distribution (Reimann & Filzmoser, 2000). Several papers and even books addressed this and, in most of them, the lognormal distribution is proposed for geochemical studies. A log-transformation is thus most frequently used for data processing. However, in those cases, lognormal distribution is assumed but not tested or proved.

Box-Cox transformation is a useful data transformation technique applied to improve the normality of the data, by stabilizing the variance. This transformation is known as a family of power transformations, which has only one parameter to estimate (Box & Cox, 1964). The expression for this transformation was presented in the Methodology Section. The Box-Cox transformation coefficient (λ) can be calculated using a statistical software. In this work, Matlab was used, which calculates the parameter λ by maximizing the Log-Likelihood Function (LLF) (Aldrich, 1997).

The parameter λ can have infinite values, however, there are many traditional transformations in this family, as it is shown below:

$$\lambda = 1.00; no\ transformation\ needed$$
$$\lambda = 0.50; square\ root\ transformation$$
$$\lambda = 0.33; cube\ root\ transformation$$
$$\lambda = 0.25; fourth\ root\ transformation$$
$$\lambda = 0.00; natural\ log\ transformation$$
$$\lambda = -0.50; inverse\ square\ root\ transformation$$
$$\lambda = -1.00; inverse\ transformation$$

**Figure 3.9** displays the results of the estimated parameter λ for each face in a histogram.

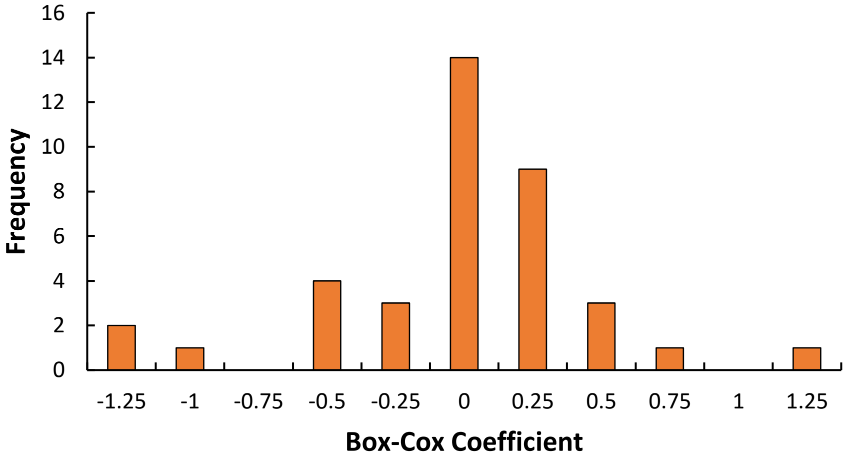

**Figure 3.9**: Histogram of Box-Cox transformation estimated parameter λ for copper grades.

As can be observed in Figure 3.9, most of the estimated coefficients were close to zero, within a range from - 0.75 to 0.75, which is the value expected when the data are drawn from a lognormal distribution. However, there was high variability between faces; the same variability that was observed for skewness and kurtosis values. Based on this variability, it was decided to perform two tests for normality of the transformed data. One test after log-transformation and another after using the coefficient calculated in the Box-Cox transformation. Figure 3.10 shows the histogram for the log-transformed copper grade data, which corresponds to the same face shown in Figure 3.5.

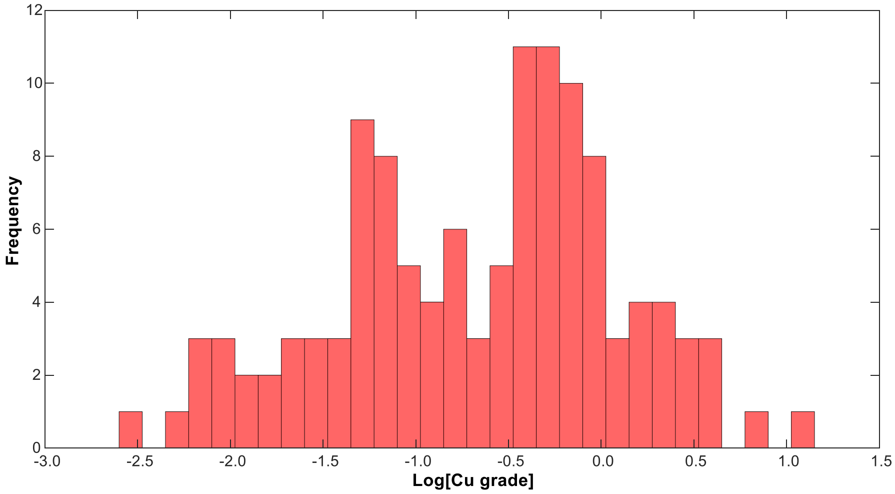

**Figure 3.10:** Histogram of log-transformed copper grade for rock H-4 face 1.

The histogram of the log-transformed copper grade data shown in Figure 3.10, presents better symmetry than the one observed from the raw data (see Figure 3.5) and has shorter tails. Table 3.4 shows a summary of the results obtained from the Anderson-Darling tests performed to log-transformed and power-transformed data. The Box-Cox coefficient was used to calculate the power-transformed data. The normality test results for each face are presented in Appendix C – Summary of Anderson-Darling normality test results – copper.

**Table 3.4**: Anderson-Darling test results for log-transformed and power-transformed copper data.

| | *Log-transformed data* | *Power-transformed data* |
|---|---|---|
| ***Total faces analyzed*** | 38 | 38 |
| ***Positive faces*** | 13 | 18 |
| ***%Positive faces*** | 34% | 47% |

According to the Anderson-Darling test of normality, only one-third of the data sets had no significant departure from normality after applying the logarithmic transformation of the copper grade values. However, better results were obtained for power-transformed data, since departure from normality was not detected in half of the data sets. Figure 3.11 shows the normal probability tests of the log-transformed copper grade data for rock H-4 face 1.

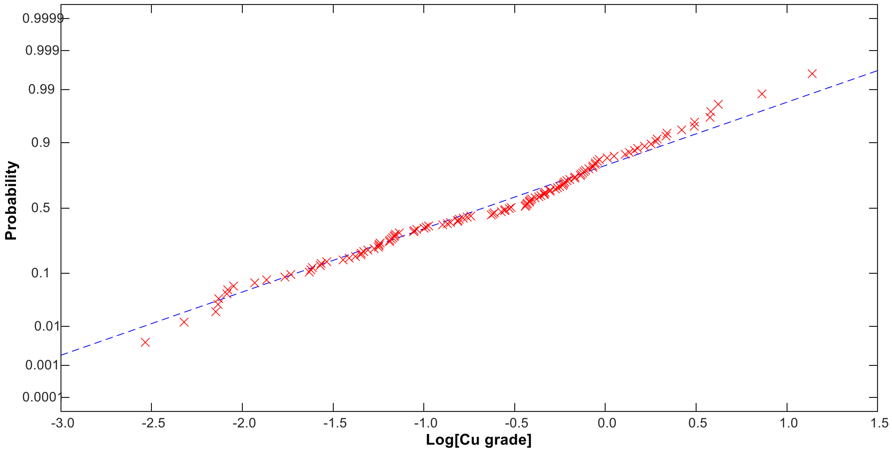

**Figure 3.11:** Normal probability plot of the log-transformed data for rock H-4 face 1.

A change in the probability trend after applying the logarithmic transformation is observed in Figure 3.11, when comparing to the normal probability plot of the raw data (see Figure 3.8). The departure from normality found in the raw data case, with probabilities lower than the ones expected for a normal distribution at low and high copper grades, has now been improved. The log-transformed data present a smoother linear trend.

#### 3.3.1.1 Summary

The copper data distributions of both samples, HG and LG, were highly right skewed, with a long tail for high copper grade values. Normality was not discarded for only two data sets, which have a low number of observations (<30). It was concluded that copper data distributions for these samples do not follow a normal distribution.

Two data transformations were analyzed, logarithmic and power transformation, in which the power coefficient was different for each rock face and calculated using Box-Cox transformation. For the first transformation, only one third of the data sets did not show significant departure from normality. For the second one, half of the data sets followed normal distribution after transformation. Both transformations did not demonstrate a feasible solution to represent the data distribution for copper grades.

### 3.3.2 Iron

The same analysis procedure, as the one presented above for the copper grade data, was followed in order to analyze the iron grade data obtained from the mapping technique. Figure 3.12 and Figure 3.13 show the box and whiskers plot where the data was grouped by face and rock.

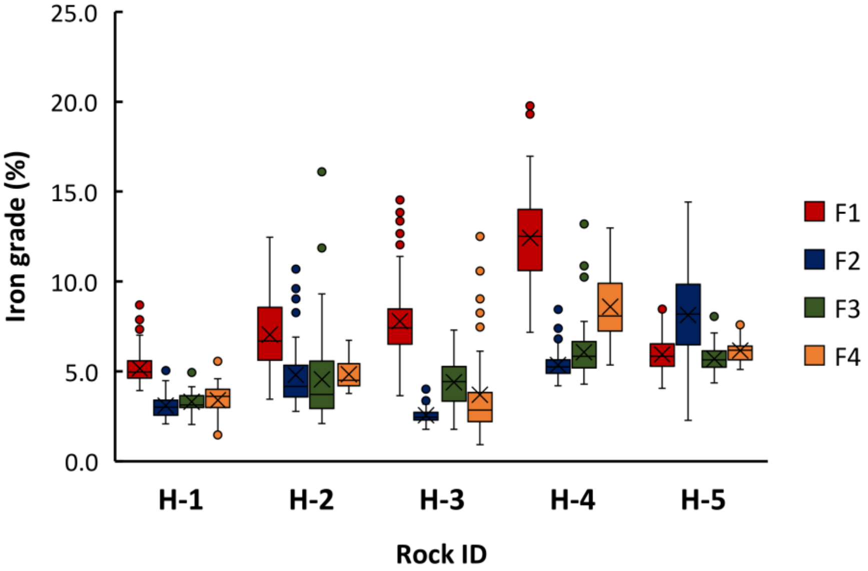

**Figure 3.12:** Box and whisker plots of iron grades for HG sample. Note: F denotes face.

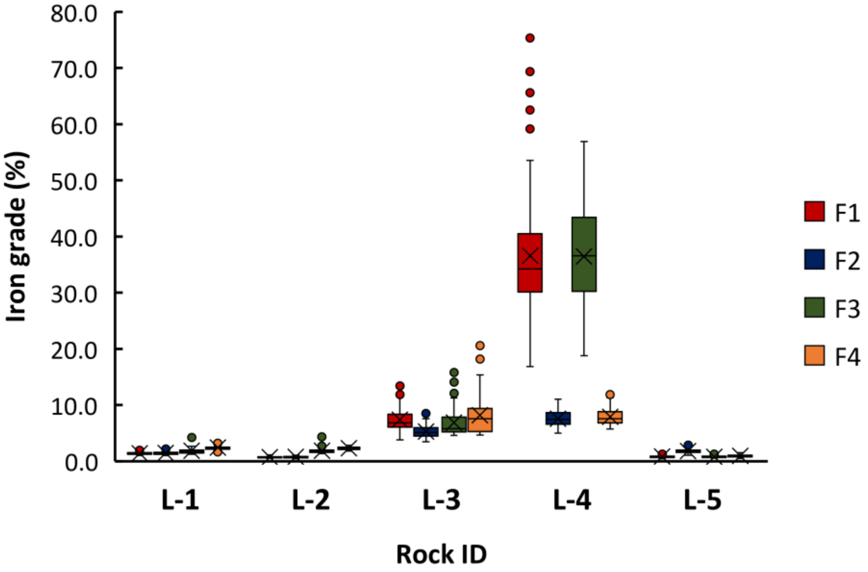

**Figure 3.13:** Box and whisker plots of iron grades for LG sample. Note: F denotes face.

As can be observed in Figure 3.12, for HG sample, iron grades at the rock surface were within a range from 1% to 20%, with most of the values located around 5 to 10%. When comparing between faces and rocks, the spread of the distributions for the iron grades were lower than the copper grades.

This observation indicates a lower heterogeneity for iron grades within the rock faces. As an example, the degree of copper grades heterogeneity for rock H-3 was high, however that high degree of heterogeneity was not observed for iron grades.

Besides differences in heterogeneity when comparing copper and iron grades, the shape of the distribution for iron grade data was different from the one for copper grade. For iron, it can be observed in Figure 3.12 that the average was close to the median which was not the case for copper. Based on the box and whisker plots, the iron grades were not as right skewed as the copper grades.

Regarding the LG sample, as shown in Figure 3.13, the measured iron grade values were, on average, in the same range of values as HG sample. The exception was for rock L-4 where extremely high iron grades were measured. These high iron grade values were even higher than expected from pure oxide or sulphide mineral containing iron, (> 60%). For this reason, they were attributed to errors of the XRF. This errors seem to be present only for high grade concentrations, since this deviation was not observed when the XRF assay results were compared to ICP results for iron grades up to 10%. The same level of heterogeneity observed for copper in rock L-4 was observed for iron. Face 1 and 3 were rich in copper and iron on this rock. However, face 2 and 4 were not as rich as the other two faces. For the HG sample, the distribution of iron grades for all the faces were not as right skewed as was found for copper grades.

Outliers were identified in almost all the faces analyzed for both HG and LG samples. However, there were not as many outliers as for the copper grades. These outliers were not discarded for further analysis since they were considered part of the grade texture of the rock, as was assumed for copper. The presence of fewer outliers for iron, when compared to copper, contributed to the fact that the iron data distributions were not as right skewed as the copper distributions. This observation indicates that the iron grade distribution may follow a normal distribution.

As explained for the copper analysis, the total area of each face represents a significant variable that needs to be considered when comparing the data obtained for different rocks and faces. The same procedure, as the one explained for copper, was followed in order to correlate the face area to the coefficient of variance (CV). Figure 3.14 shows the correlation between face area and CV for both HG and LG samples combined, where the average area and CV of the bins were plotted.

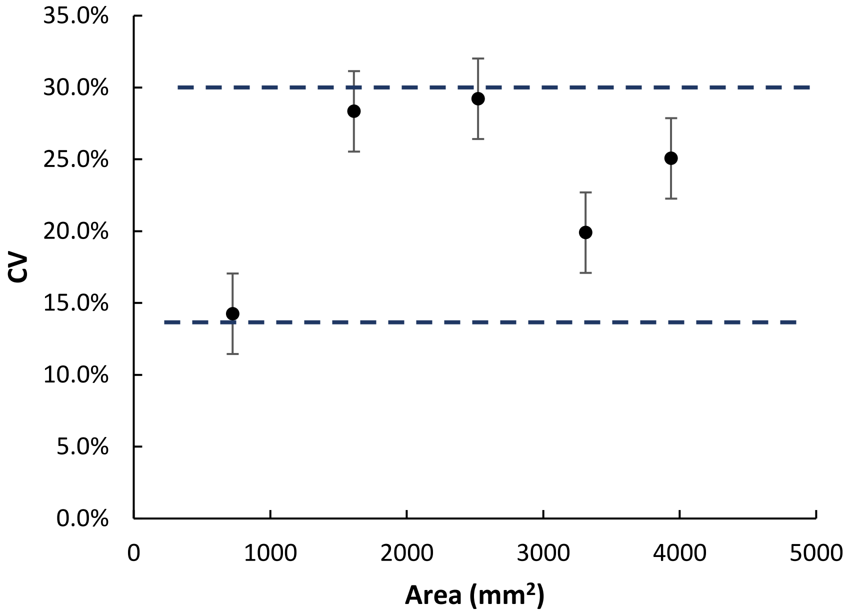

**Figure 3.14:** Correlation between face area and coefficient of variation (CV) of iron grade for HG and LG samples combined.

As can be seen in Figure 3.14, there was no correlation between CV and face area for iron data, at this particle size range. The trend observed for copper data was not present for iron data. The CV values varied within a range from 13% to 30%. Another significant difference in the CV values, between copper and iron data, was that the CV values for iron were considerably lower than the ones calculated for copper, which means that the grade variability was lower. The ranges of CV values seen for iron data were low enough to associate iron data distribution to a normal distribution.

Repeatability tests were performed for iron grade to determine how much of the grade variability detected was introduced by the method of elemental analysis. The iron grade of a rock sample was measured 8 times at the same spot under identical conditions, and a coefficient of variation of 1.37% for iron grade was obtained. This CV value represents between 5 to 10% of the total variability measured at the rock surface for iron grade (from 13% to 30%), which was considered acceptable.

Based on the analysis presented above, it can be concluded that the iron data distribution was not as right skewed as the copper distribution. Fewer outliers were detected and there was lower variability of iron grade within each face, when compared to copper analysis. An example of a histogram is shown in Figure 3.15 for rock H-4 face 1. As explained for the copper analysis, this face was selected in order to display and discuss the results presented in this section.

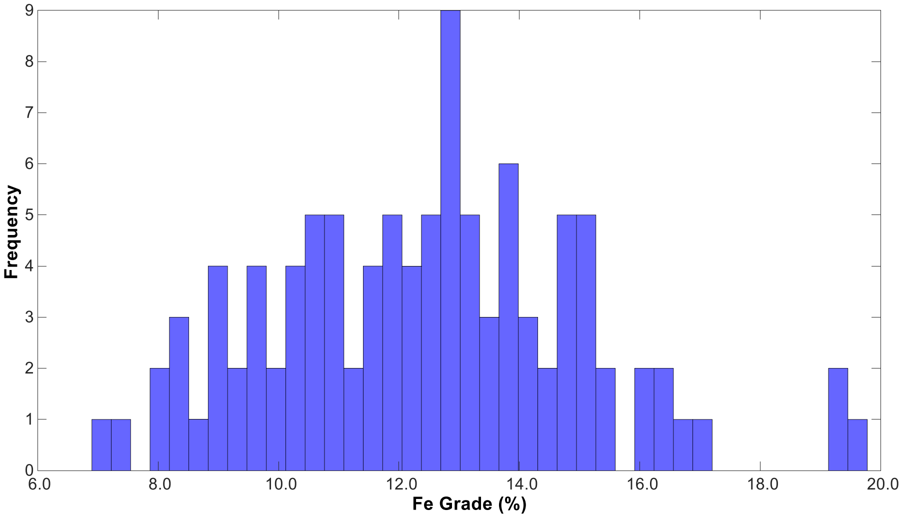

**Figure 3.15:** Histogram of iron grade for rock H-4 face 1.

The histogram shown in Figure 3.15 was generated from 103 measurements. The data distribution was highly symmetric and centered around 13%, with low to medium variability. To summarize the shape of the iron distribution data for the other samples, Figure 3.6 and Figure 3.7 show the skewness and kurtosis histograms calculated for each face, respectively.

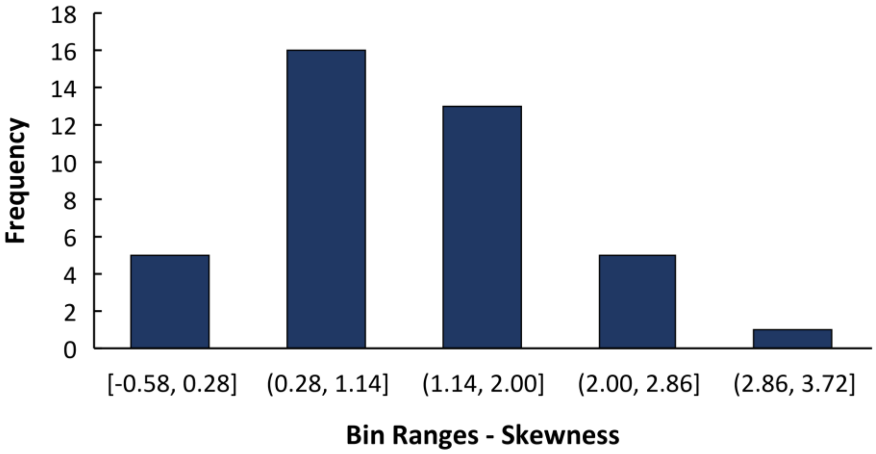

**Figure 3.16:** Skewness histogram for iron data, with 40 faces being analyzed.

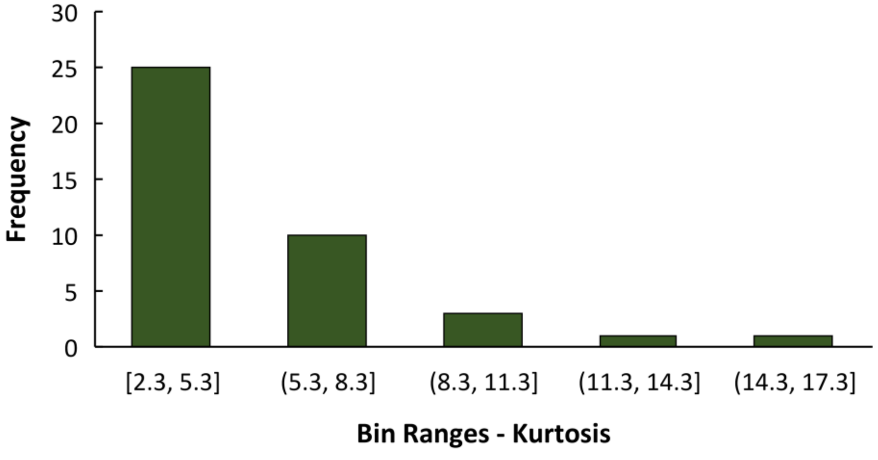

**Figure 3.17:** Kurtosis histogram for iron data, with 40 faces being analyzed.

Since iron was above the limit of detection for all the faces, all of them (40) were analyzed. The histogram of skewness values, presented in Figure 3.16, shows that iron data distributions were, in general, symmetric, with some of them slightly right skewed and with skewness values close to 0. Furthermore, there were a few other distributions that had a negative skewness values, which means that they were slightly left skewed.

Figure 3.17 is a histogram showing the kurtosis values calculated for each face based on the iron data. The data distributions were generally symmetric, with kurtosis values close to 3. However, there were also a few exceptions to this trend. Data distributions with kurtosis values close to 3 are called *mesokurtic*. These data distributions have tails shaped in roughly the same way as any normal distribution.

Based on the evidences presented above, showing low to medium coefficient of variation, symmetric distributions, and kurtosis values close to 3, the iron data distributions measured may be drawn from a normal distribution. The Anderson-Darling test was carried out in order to evaluate normality. Table 3.5 summarizes the results obtained after the application of the Anderson-Darling test. The test results for each face are presented in Appendix D – Summary of Anderson-Darling normality test results – iron.

**Table 3.5:** Anderson-Darling test results for iron raw data.

| | **Raw data** |
|---|---|
| ***Total faces analyzed*** | 40 |
| ***Positive faces*** | 12 |
| ***%Positive faces*** | 30% |

Although the evidence listed above showed that iron data distributions may be closer to the shape of a normal distribution, only 30% of the faces had a positive normality, which means that no significant departure from normality was found. The normality was rejected at a 5% significance level for the other faces. Figure 3.18 shows the normal probability plot for rock H-4 face 1, whose histogram was shown in Figure 3.15.

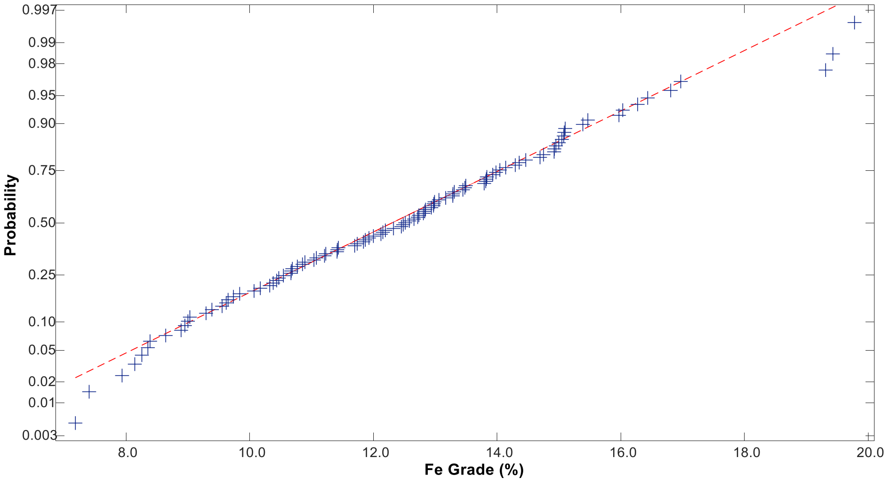

**Figure 3.18:** Normal probability plot for iron grades of rock H-4 face 1.

Although a departure from normality was observed in Figure 3.18 for rock H-4 face 1, the Anderson-Darling test for this face showed that there was no significant departure from normality with a *p-value* of 0.755.

Based on the results obtained from the normality test, the Box-Cox transformation was evaluated for iron data. Figure 3.19 summarizes the results of the estimated parameter λ for each face in a histogram.

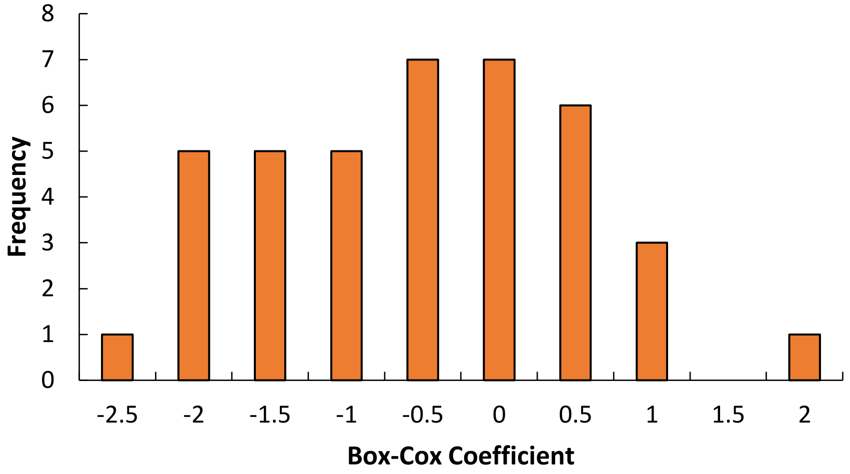

**Figure 3.19:** Histogram of Box-Cox transformation estimated parameter λ for iron grades.

There was a high variability in the estimated parameters, which varied within a range from – 2.5 to 2 and were homogeneously distributed over this range. Based on this variability, it was decided to carry out two tests for normality; one for log-transformed data and another one for power-transformed data. Figure 3.20 shows the histogram for the log-transformed iron grade data, which corresponds to the same face shown in Figure 3.15.

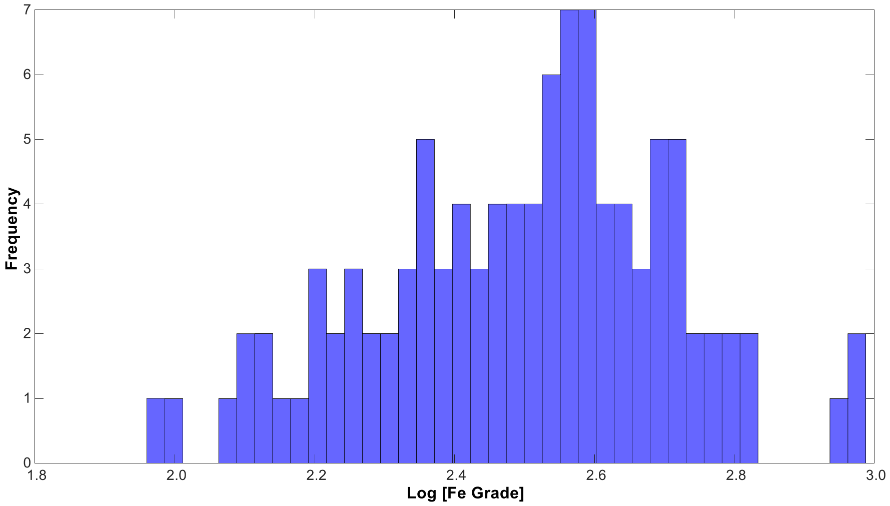

**Figure 3.20:** Histogram of log-transformed iron grade for rock H-4 face 1.

The histogram of the log-transformed copper grade data shown in Figure 3.20, presents almost the same symmetry as the one generated with the raw data (see Figure 3.15) but with shorter tails. Table 3.6 shows a summary of the results obtained from the Anderson-Darling tests performed to log-transformed and power-transformed data for iron. The Box-Cox coefficient was used to calculate power-transformed data. The normality test results for each face are presented in Appendix D – Summary of Anderson-Darling normality test results – iron.

**Table 3.6:** Anderson-Darling test results for log-transformed and power-transformed iron data.

| | *Log-transformed data* | *Power-transformed data* |
|---|---|---|
| ***Total faces analyzed*** | 40 | 40 |
| ***Positive faces*** | 18 | 35 |
| ***%Positive faces*** | 45% | 88% |

According to the Anderson-Darling test for normality, for almost half of the data sets, there was no significant departure from normality after applying the logarithmic transformation. However, better results were obtained for power-transformed data, where in 88% of the data sets significant departure from normality was not detected. Figure 3.21 shows the normal probability plot of the log-transformed iron grade data for rock H-4 face 1.

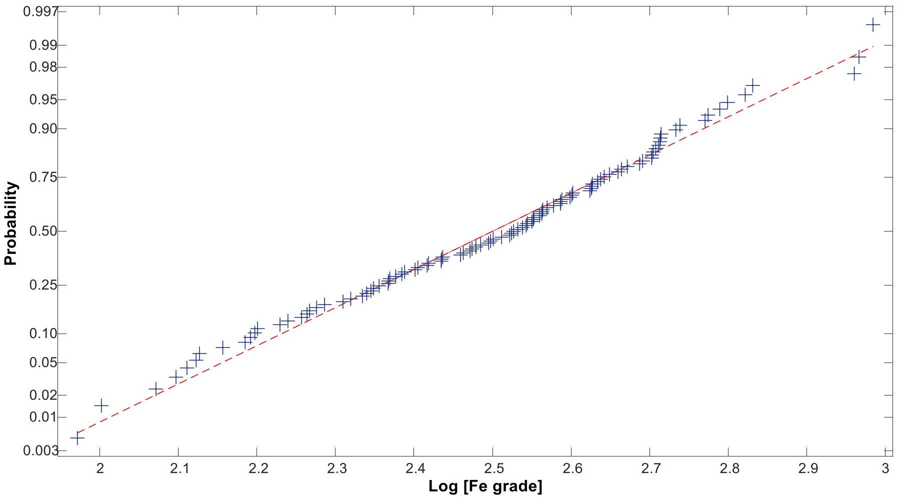

**Figure 3.21**: Normal probability plot of the log-transformed data for rock H-4 face 1.

The probability plot after applying the logarithmic transformation slightly changed from the plot of the raw data (see Figure 3.18). Both of them have a smooth lineal trend. The Anderson-Darling test showed that there was no significant departure from normality for the log-transformed data, as for the raw data.

### 3.3.2.1 Summary

The iron data distributions of both samples, HG and LG, showed evidence to associated them to normal distributions, with skewness values close to 0 and kurtosis values close to 3. However, only one third of the data sets did not show significant departure from normality.

The same two data transformations, the logarithmic and power transformations, that were studied for copper, were analyzed for iron. Better results were achieved for iron than for copper. Almost half of the data sets showed no significant departure from normality after log transformation. The results were even better for the power transformation, where 90% of the data sets followed normal distribution after transformation. The results may indicate that iron grades follow a power distribution with a variable power coefficient.

The difference in the grade distributions for iron grades when compared to copper grades indicates a dependency of the grade distribution with the element analyzed and its mineral source. For the porphyry copper ore, the mineral source for copper is mainly chalcopyrite with some contributions from bornite. However, the minerals containing iron, such as chalcopyrite, bornite, pyrite, hematite and magnetite, are more diverse, abundant, and widely distributed in the deposit.

## 3.4 Particle grade estimation and one-dimensional assessment of intraparticle heterogeneity

The observation that copper and iron grade distributions do not approach normal or lognormal distribution has serious consequences on further statistical analysis of the data sets. These consequences are often neglected by scientists when processing geochemistry data. The main consequence is that the geometric mean and median are better estimator of the central tendency than the commonly used arithmetic mean.

A normality analysis of four geochemical and environmental data sets, with more than 50 elements, showed that those data sets did not follow a normal distribution (Reimann & Filzmoser, 2000). In the same work, it was shown that transformations such as log, ln or square root, did not result in a normal distribution. The arithmetic mean and standard deviation were not the best parameters for central tendency and spread, respectively. The median was the best measure of the central tendency in that analysis, and the geometric mean was an acceptable alternative but problematic in some cases. Furthermore, the median absolute deviation (mad) or the hinge-spread were suggested as a measure of spread, instead of using the standard deviation. (Reimann & Filzmoser, 2000).

In this section, the correlation between rock surface grade, obtained from the XRF mapping, and bulk rock grade, generated by chemical assays of the entire rock, is analyzed for copper and iron for the ten rocks. The arithmetic and geometric mean as well as the median, are compared as estimators for the central tendency of the surface grade. For the correlation analysis, both samples are combined in order to cover a wider range of grades. Furthermore, intraparticle heterogeneity is quantified by calculating the median absolute deviation for each rock based on the median of each face, for both HG and LG samples. The results are discussed in terms of the type of mineralization observed in each rock.

### 3.4.1 Copper

Figure 3.22, Figure 3.23 and Figure 3.24 show the correlation between surface copper grades and bulk copper grade, where the surface grade was calculated as arithmetic mean, geometric mean and median, respectively. All the copper grades measured for each rock from both HG and LG samples were used for this analysis. As it was explained before, the spots where copper grade was below the detection limit of the XRF device were replaced by half of the detection limit. This change was critical for the geometric mean calculation, since zero values generate zero as result. The values used in the following graphs are presented in Appendix E – Central tendency parameter values per rock – copper.

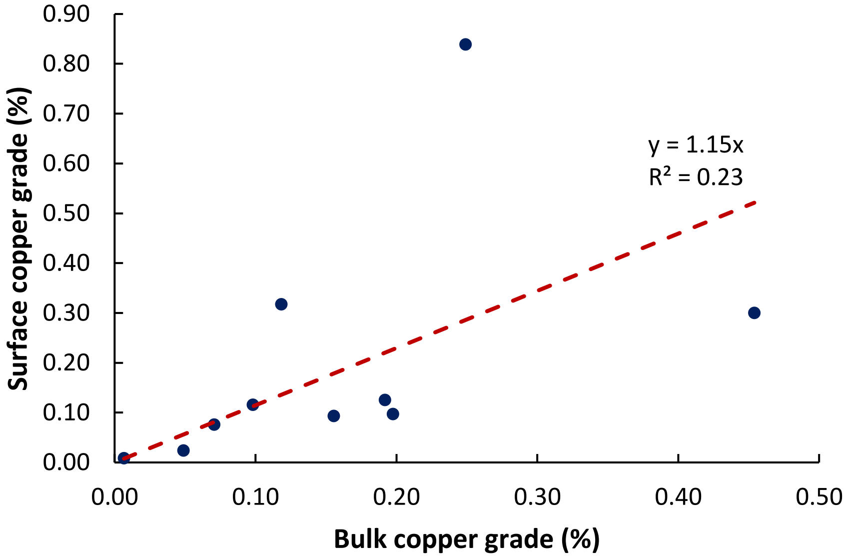

**Figure 3.22:** Correlation between surface copper grades and bulk copper grade using the arithmetic mean for surface grade calculation.

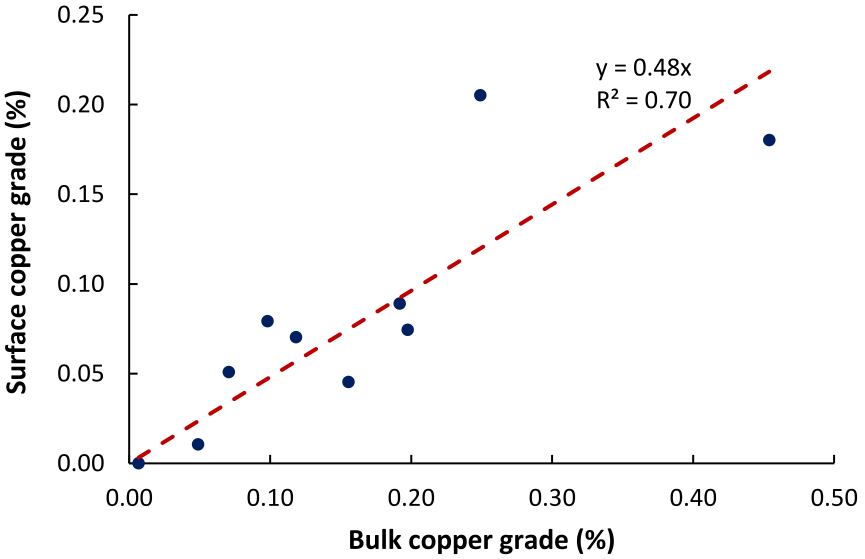

**Figure 3.23:** Correlation between surface copper grades and bulk copper grade using geometric mean for surface grade calculation.

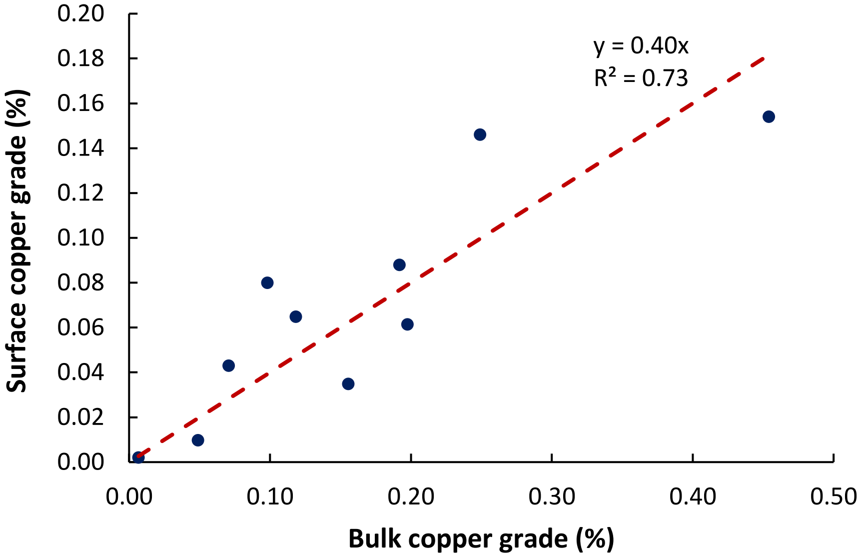

**Figure 3.24:** Correlation between surface copper grades and bulk copper grade using the median for surface grade calculation.

The correlation was assumed linear with the intersection in the ordinate set at zero. The copper detection limit values, for surface and bulk assays, were of the same order of magnitude. Copper should not be detected at the rock surface, if it is not detected in the bulk assay.

The coefficient of determination, denoted as "$R^2$", was selected to compare the correlation between surface and bulk copper grades. For the samples analyzed, a considerable improvement was observed when the geometric mean and median were used over the arithmetic mean to estimate the central tendency of the surface grade (see Figure 3.22, Figure 3.23 and Figure 3.24). A better correlation between rock surface and bulk copper grade was achieved when using the geometric mean and median, with coefficients of determination of 0.70 and 0.73, respectively. This improvement was consistent with the outcome of the data distribution analysis. Copper grade distributions did not follow a normal distribution, and were right skewed.

The influence of high copper grade values on the arithmetic mean can be observed in the value of the slope from linear regression. A higher slope of 1.15 was obtained for the arithmetic mean case than for the geometric mean and median case, for which slope values were 0.48 and 0.40, respectively.

When sensing four faces of each rock with a handheld XRF device and using a univariate linear regression approach, the correlation achieved using the median of the surface grades showed that these two samples may be sorted based on their copper surface grades. The implementation of these results in a larger scale highly depends on the capabilities of the XRF sensors used in industrial scale sorters to detect copper at the range values evaluated in this work.

Since better correlation between rock surface and bulk copper grades was achieved when using the median of the surface grades, the median and the median absolute deviation were selected to quantify intraparticle heterogeneity in one dimension. Figure 3.25 and Figure 3.26 present the surface grade of each face and the entire rock, using the median for its calculation, for HG and LG samples, respectively.

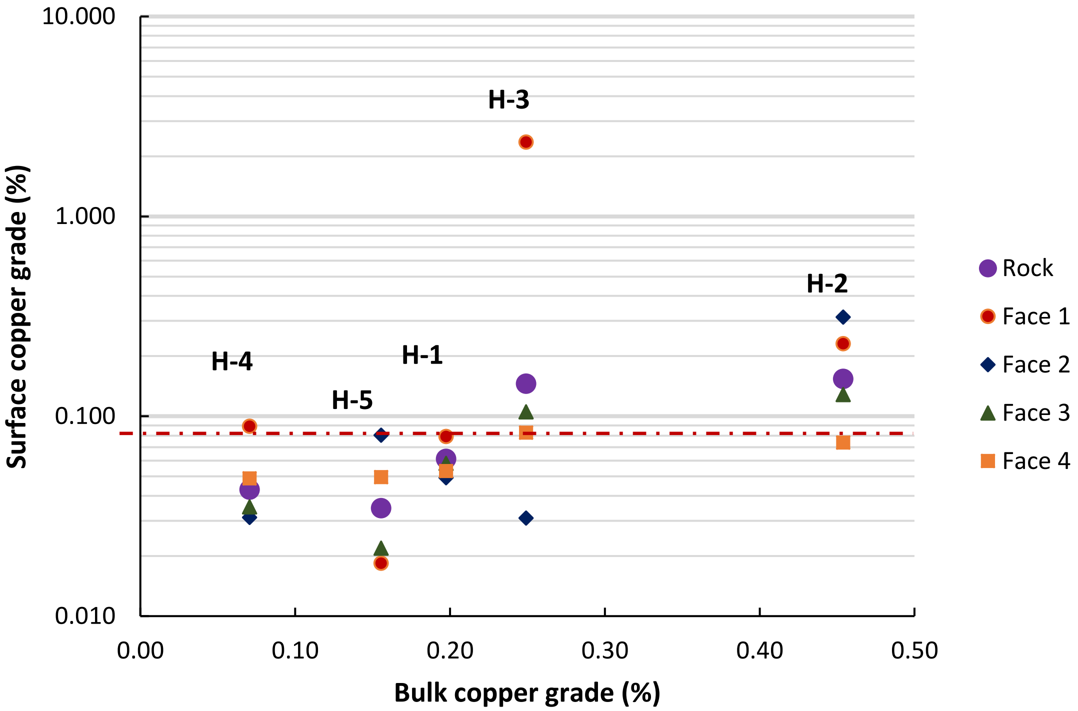

**Figure 3.25:** Surface copper grade of each face and the entire rock for HG sample, using the median for surface grade calculation. Note: logarithmic scale is used for surface grade axis.

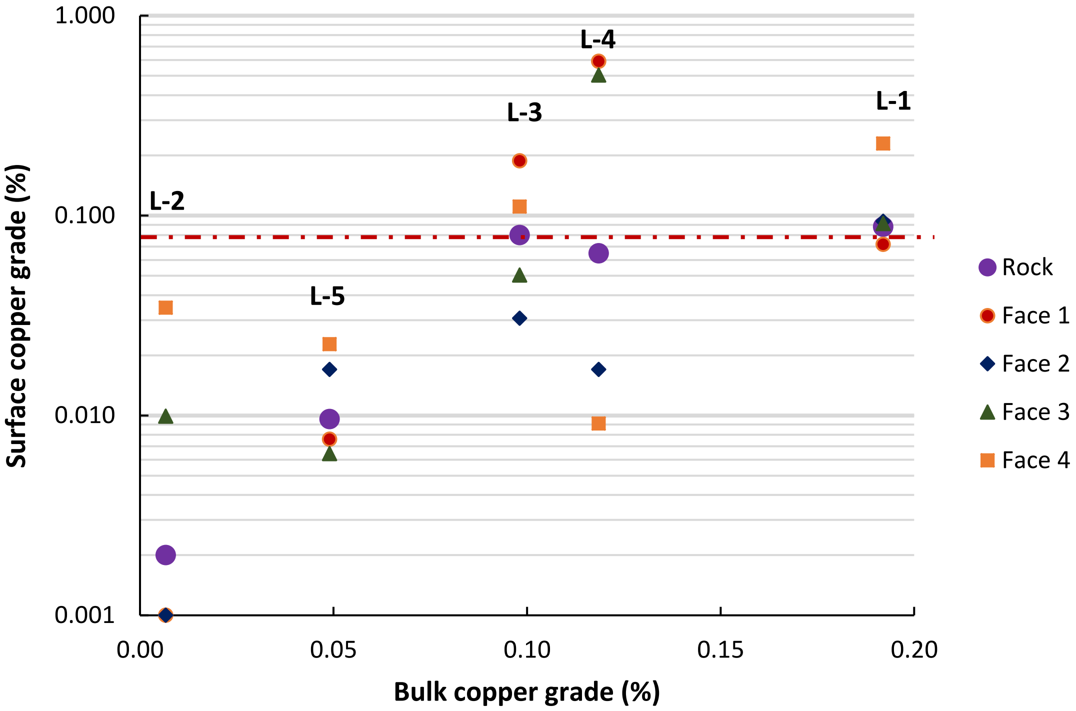

**Figure 3.26:** Surface copper grade of each face and the entire rock for LG sample, using the median for surface grade calculation. Note: logarithmic scale is used for surface grade axis.

A logarithmic scale was used for the rock surface grade axis in both figures due to the high spread of the surface copper grade values present within each rock. The highest spread was observed for rock H-3 and rock L-4, where the largest median face grade was almost 20 times higher than the lowest median face grade (see Figure 3.25 and Figure 3.26). The lowest spread for rock surface grades was observed in rock H-1, where the face grade medians were within a small copper grade range, of 0.5% to 0.8%.

Since in an XRF sorter only part of the surface is scanned, the intraparticle heterogeneity present in each rock is an important variable. A high degree of intraparticle heterogeneity, which can be reflected in this case in a high spread of rock face medians, may generate results that are not reproducible, thus affecting the performance of the equipment.

For a better understanding of the effect of intraparticle heterogeneity on the performance of an XRF sorter, a case scenario is presented. In this case scenario, the linear regression of the correlation between rock surface and bulk grade observed in Figure 3.24 was selected to sort the 10 rocks analyzed in this work. The current cut-off grade applied in the mine, which corresponds to 0.19% copper, was defined as the bulk copper grade value used to decide whether each rock was ore or waste. Then, based on the linear regression previously selected using medians ([%Cu Surf] = 0.40 x

[%Cu Bulk]), the threshold value for the XRF sorter in terms of surface copper grade was 0.08%. This value was plotted in Figure 3.25 and Figure 3.26 as a horizontal dash red line.

For this cut-off grade, rocks H-1, H-2, H-3, and L-1 should be sorted as ore. However, each of these rocks has at least one face with a median copper grade value lower than the threshold of 0.08%. In other words, if the surface copper grade of one face was used for sorting, the rocks could be rejected even though, based on the bulk grade, four of them should be classified as ore. In the opposite case, it was possible to classify eight rocks as ore, since each of these rocks had at least one face with a copper grade median higher than 0.08% (see Figure 3.25 and Figure 3.26).

The scenario presented shows how the reproducibility of the results from a XRF sorter can be affected by the intraparticle heterogeneity due to its limitation to scan only part of the surface of each rock. In this case, for the threshold value selected, there was a probability of discarding all the rocks and at the same time, of accepting eight of them.

The same limitation presented, in this work, for surface copper grade could be found in other surface testing techniques, such as photometric sensing. Therefore, it is considered that an analysis of intraparticle heterogeneity should be included in the assessment of the sorting potential of an ore by using all surface sensing techniques.

After showing the importance of intraparticle heterogeneity to XRF sorter, it is necessary to understand how this heterogeneity varies between rocks, as a function of variables such as particle size, lithology or type of mineralization. Based on the analysis of the data distribution and the results obtained for the regression analysis, the median and the median absolute deviation of the mapping data were selected to estimate the copper grade and the intraparticle heterogeneity, respectively. These values are presented in Table 3.7 for the rocks of both HG and LG samples.

A single median was calculated with all the measurements collected for a rock. The median absolute deviation was calculated using four medians, one per face. Also, the ratio between the median and the median absolute deviation is shown in Table 3.7 to compare rocks at different copper grades.

**Table 3.7:** Rock surface copper grade median and median absolute deviation values, and ratio between them.

| | ***Rock surface copper grade median ($m$) [%]*** | ***Rock surface copper grade median absolute deviation ($MAD$) [%]*** | $^{m}/_{MAD}$ ***[%]*** |
|---|---|---|---|
| *H-1* | 0.061 | 0.010 | 16.6% |
| *H-2* | 0.154 | 0.079 | 51.1% |
| *H-3* | 0.146 | 0.089 | 61.0% |
| *H-4* | 0.043 | 0.010 | 22.7% |
| *H-5* | 0.035 | 0.016 | 44.9% |
| *L-1* | 0.088 | 0.011 | 12.5% |
| *L-2* | 0.002 | 0.004 | 222.5% |
| *L-3* | 0.080 | 0.040 | 50.3% |
| *L-4* | 0.065 | 0.248 | 382.8% |
| *L-5* | 0.010 | 0.005 | 54.9% |

As can be observed in Table 3.7, the highest value for median absolute deviation was obtained for rocks L-4, H-3 and H-2. In these rocks, copper was found in veins as described in the Sample characterization Section. The highest median absolute deviation of rock L-4 can be explained based on how copper is distributed at the rock surface. Two faces of this rock were along copper veins, with a high copper grade, while the other faces were perpendicular to the veins, with a low copper grade. This observation indicates that mineralization in veins was associated with a higher degree of intraparticle heterogeneity for copper grades. In this case, this higher degree of intraparticle heterogeneity was reflected in a higher median absolute deviation.

#### 3.4.1.1 Summary

It was shown that for these two samples, the median of the surface grade data was the best estimator to correlate surface grade to bulk grade for copper, with a coefficient of determination of 0.73. This result was consistent with the outcome of the distribution analysis, which showed that copper data distribution was non-normal, highly right skewed and with long tails due to high copper values. The correlation achieved using the median of the surface grade showed that these two samples might be sorted based on their copper surface grade, when sensing four faces per rock with a handheld XRF device and applying an univariate linear regression model. The implementation of these results at a larger scale depends highly on the capabilities of the XRF sensors used in industrial scale sorters to detect copper at the range of values evaluated in this work.

A scenario was described to demonstrate the relationship between reproducibility of an XRF results and the degree of intraparticle heterogeneity. For this copper ore, with mainly vein type mineralization, the assessment showed a high degree of intraparticle heterogeneity, which may generate poor reproducibility when sensing only one face of each rock. Finally, the median and median absolute deviation were proposed as the best estimators for surface grade and intraparticle heterogeneity, respectively, and should therefore be used to summarize copper data for the XRF mapping.

### 3.4.2 Iron

The correlations between surface copper grades and bulk iron grade are shown in Figure 3.27, Figure 3.28 and Figure 3.29. The surface grades were calculated as arithmetic mean, geometric mean and median, respectively. Iron was detected in all the spots analysed. The values used in the following graphs are presented in Appendix F – Central tendency parameter values per rock – iron.

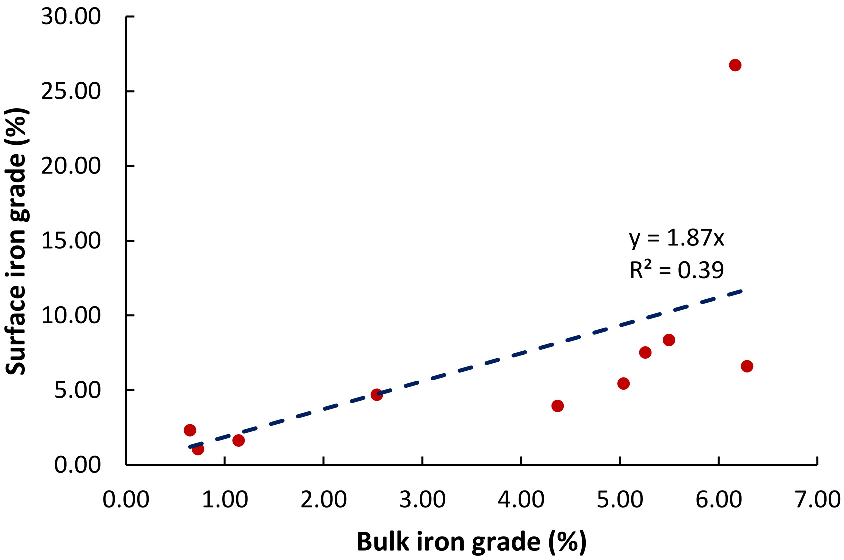

**Figure 3.27:** Correlation between surface iron grades and bulk iron grade using the arithmetic mean for surface grade calculation.

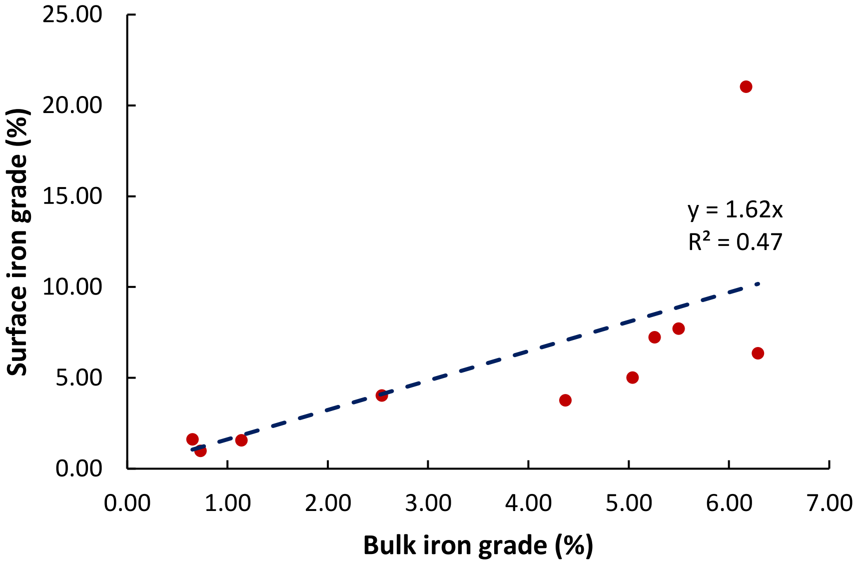

**Figure 3.28:** Correlation between surface iron grades and bulk iron grade using the geometric mean for surface grade calculation.

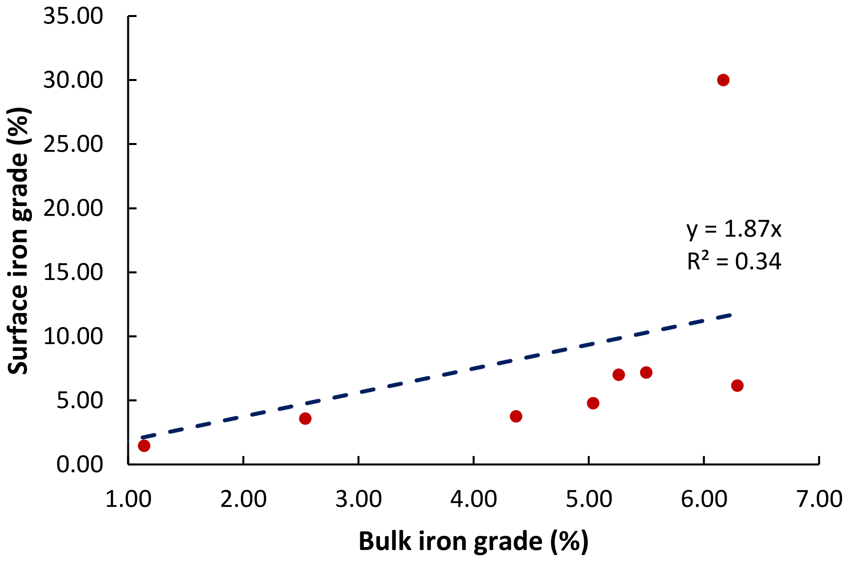

**Figure 3.29:** Correlation between surface iron grades and bulk iron grade using the median for surface grade calculation.

Linear regression was selected to evaluate the correlation between the surface and bulk grade. The intersection in the ordinate was set to zero, since the iron grade at the surface should be zero if the bulk iron grade is zero. As shown in Figure 3.27, Figure 3.28 and Figure 3.29, poor correlations between surface and bulk iron grades were achieved. In all cases, the main reason for this poor correlation was explained by one of the rocks, which had a surface grade significantly higher than the bulk grade. After reviewing the data, it was found that rock L-4 was the rock with the highest grades. As explained in the Sample description Section, this rock was different from the others, with two faces that were along of veins rich in sulphides – pyrite and chalcopyrite – showing extremely high copper and iron grades. Also, the iron values obtained for one of the rock faces showed extremely high iron grades (>60%) that may be an error of the XRF sensor. In order to show the influence of this sample on the analysis for iron, the correlation was evaluated without considering this particular rock. Table 3.8 shows the results of the analysis excluding Rock L-4, the arithmetic and geometric mean, and median were evaluated.

**Table 3.8:** Regression analysis for iron grade excluding rock L-4.

| | ***Slope value*** | ***$R^2$*** |
|---|---|---|
| ***Arithmetic mean*** | 1.24 | 0.77 |
| ***Geometric mean*** | 1.17 | 0.84 |
| ***Median*** | 1.12 | 0.86 |

A considerable improvement in the correlation is observed in Table 3.8 after excluding rock L-4 from the regression analysis. The values for the coefficient of determination were approximately two times higher than those calculated when using all the rocks. The best correlation was obtained when the median was used to estimate the central tendency of the iron surfaces grade. However, in the case of iron, the improvement of the median over the arithmetic mean was not as significant as the copper case. This observation is consistent with the outcome from the distribution analysis. The iron grade distribution showed a symmetric shape, with low skewness and kurtosis values, similar to a normal distribution and the arithmetic mean is the best estimator of the central tendency when the distribution is normal.

When analysing the slope values shown in Table 3.8, the effect of high iron grades on the arithmetic mean can be observed. A higher slope value was obtained when the arithmetic mean was used to estimate the central tendency of the surface grade. This effect was also observed for copper grade. However, for iron, the slope values were significantly higher than the ones obtained for copper, where bulk grade was two times higher, on average, than surface grade. In the case of iron, the correlation between surface grade and bulk grade was almost one to one.

The same approach used to assess intraparticle heterogeneity for copper in one dimension was selected for iron. Figure 3.30 and Figure 3.31 shows the iron surface grade of each face and the entire rock, calculated using the median, for the HG and LG samples, respectively.

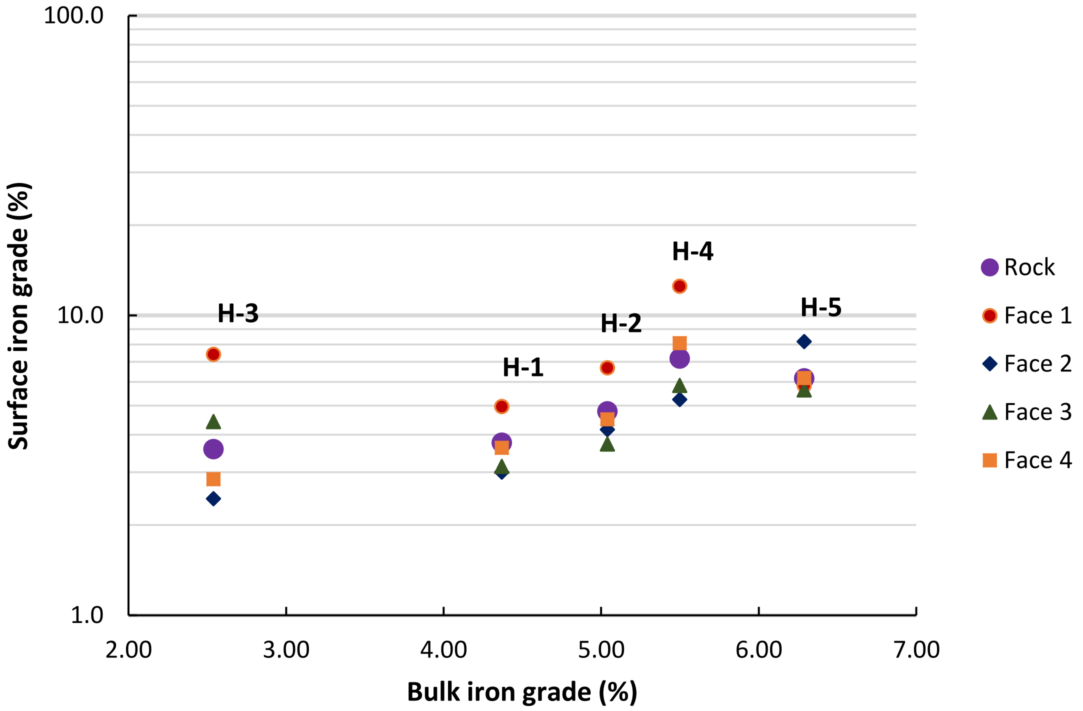

**Figure 3.30:** Surface iron grade of each face and the entire rock for HG sample, using the median for surface grade calculation. Note: logarithmic scale is used for surface grade axis.

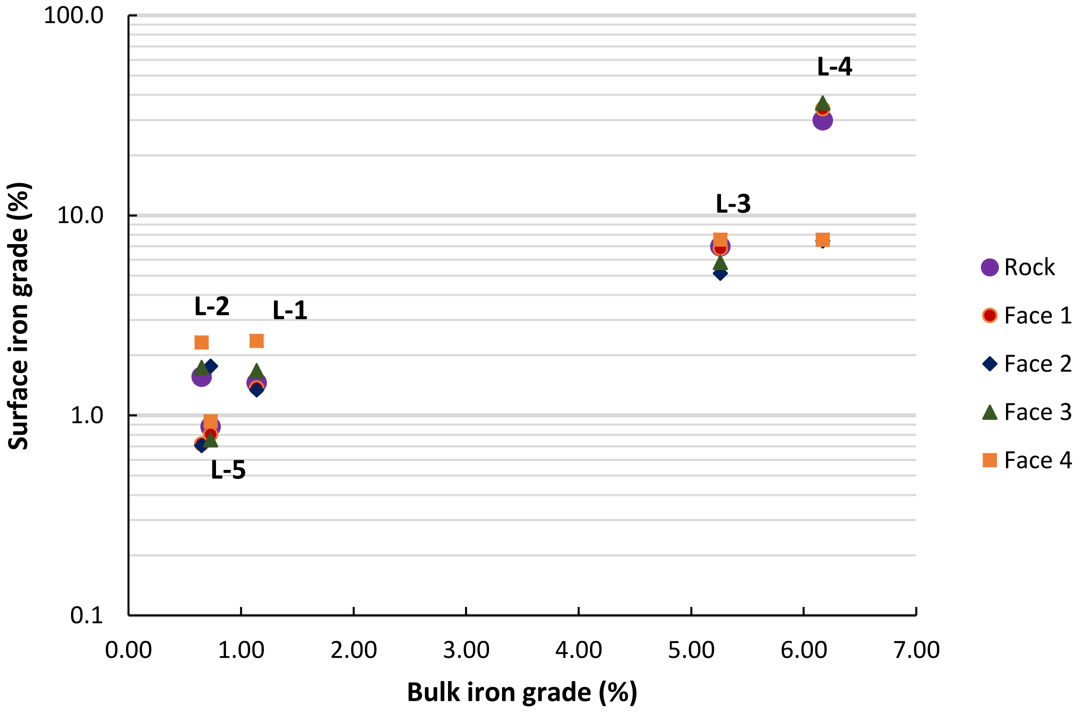

**Figure 3.31:** Surface iron grade of each face and the entire rock for LG sample, using the median for surface grade calculation. Note: logarithmic scale is used for surface grade axis.

A logarithmic scale was used for the rock surface grade axis in both figures. In this case, the log scale was not due to the high spread of the surface copper grade values present within each rock, but because of the variability between rocks. Lower variability in the iron grades than in the copper grades within each rock was observed. The higher spread was observed for rock L-4, where the largest median face grade was almost four times higher than the lowest median face grade (see Figure 3.30 and Figure 3.31 ). It should be mentioned that this high spread may be generated by erroneously high iron grades introduced by the XRF device. The narrowest distribution for rock surface grades was observed for Rock L-5, which also had the lowest iron grades.

The lower variability observed in iron grades when compared to copper grades indicates a dependency of the intraparticle heterogeneity with the element analyzed and its mineral source. For the porphyry copper ore, the mineral source for copper is mainly chalcopyrite with some contributions from bornite. However, the minerals containing iron are more diverse including chalcopyrite, bornite, pyrite, hematite and magnetite.

Table 3.9 presents the median and the median absolute deviation of the mapping data, as well as their ratio of median and median absolute deviation.

**Table 3.9:** Rock surface iron grade median and median absolute deviation values, and ratio between them.

| | ***Rock surface iron grade median ($m$)*** | ***Rock surface iron grade median absolute deviation ($MAD$)*** | $^{m}/_{MAD}$ |
|---|---|---|---|
| *H-1* | 3.76 | 0.69 | 18.4% |
| *H-2* | 4.78 | 0.84 | 17.6% |
| *H-3* | 3.58 | 0.99 | 27.6% |
| *H-4* | 7.17 | 1.63 | 22.8% |
| *H-5* | 6.16 | 0.42 | 6.8% |
| *L-1* | 1.46 | 0.16 | 11.3% |
| *L-2* | 1.57 | 0.80 | 51.2% |
| *L-3* | 7.01 | 0.88 | 12.5% |
| *L-4* | 30.00 | 14.50 | 48.3% |
| *L-5* | 0.88 | 0.10 | 11.4% |

Low values of the ratio between median and median absolute deviation for iron grade were obtained when compared to the ratio values for copper grade (see Table 3.7). The rock L-2 and the rock L-4 showed the highest values for this ratio. This observation shows that iron grade variability is not linearly correlated to the iron grades. The iron grade median for rock L-4 was twenty times higher than the iron grade median for rock L-2, but the median absolute deviation values were similar for both rocks.

The absolute values for the iron grade were higher than the copper grade, this makes the iron easier to be detected by XRF sensor of an industrial scale sorter. Also, the variability for iron grades was lower than for copper grades. Based on these two observations it was decided to evaluate iron surface grade as an estimator of copper bulk grade. However, a poor correlation between iron surface grades and bulk copper grades was achieved, with a coefficient of determination value of -0.30. Then, the iron surface grade was not a good estimator for the copper bulk grade of each rock when applying linear regression.

#### 3.4.2.1 Summary

For the HG and LG samples, the median and the geometric mean of the surface grade data were the best estimators to correlate surface grade to bulk grade for iron, with a coefficient of determination of 0.86 and 0.84, respectively. These results were consistent with the outcome of the distribution analysis performed on the iron data, which showed that the iron data distribution was non-normal.

The median and median absolute deviation were proposed as the best estimators for surface grade and intraparticle heterogeneity, respectively. These parameters can be used to summarize the iron grade data generated with the XRF mapping method designed.

The assessment of intraparticle heterogeneity for iron grade showed a lower variability than the variability detected for copper grade. The iron surface grade was evaluated as an estimator of the bulk copper grade, but a poor correlation was achieved. Therefore, iron was not suitable as a proxy for bulk copper grade for the ore tested.

## 3.5 Variography for two-dimensional intraparticle heterogeneity assessment

### 3.5.1 Variogram analysis

The variogram is a widely used tool which has been proposed to describe the spatial correlations of punctual spatial observations. The objective of this tool is pattern evaluation of a given variable in space. In this work, experimental variograms for copper and iron grade were constructed using Matlab software. The results were analyzed and compared to the description obtained from visual inspections of the rocks. As explained in the Introduction Section, Lyman proposed the sill and the range of the variogram as a measure of the in-situ heterogeneity for rock texture analysis (Lyman, 2011). In this section, the variogram is evaluated to assess intraparticle heterogeneity for the samples analysed.

In geostatistical applications, the variogram usually exhibits a typical curve, in which the values are low at small lags (close to the origin), and they directly increase until reaching a plateau (sill) which is similar to the population variance. This trend indicates that there is no spatial dependency over longer distances, but there is a spatial correlation at short distances. When fitting a variogram model to the data, theoretical exponential and spherical models are often employed to represent the experimental data. Before describing the results obtained in this work, it must be understood that these models are theoretical, which means that there is a strong probability that these models will not fit exactly to the data under study.

To begin with the analysis, inspection of the data was carried out. A “proportional effect” was found due to a wide range of concentrations detected within the rocks. For some rock faces, values as high as 5% in copper were detected, however, copper was not detected at all in other rock faces. To overcome this “proportional effect”, the experimental variogram was divided by the square of the grade average of each face. This correction produces a “relative variogram”, implying that all the values are now relative to the local mean, which is the mean for the face. It has not been proved how well the process of correcting experimental variograms for the proportional effect works, but it represents a useful tool to compare the experimental variogram to the population variance (Clark, 1987).

Visual inspection was useful for getting an insight in the variogram trends. The typical curve described above was observed only in one rock face for copper. However, repetitions of other patterns were observed. To summarize the results obtained for all faces and to organize the discussion, the variogram curves observed were classified into four types. A detail description of each type and a table with the type of curve observed in each face are presented below. A schematic representation of each curve type is shown in Figure 3.32. The variogram plots of each face for copper and iron are presented in Appendix G – Experimental variograms for copper grade and Appendix H – Experimental variograms for iron grade.

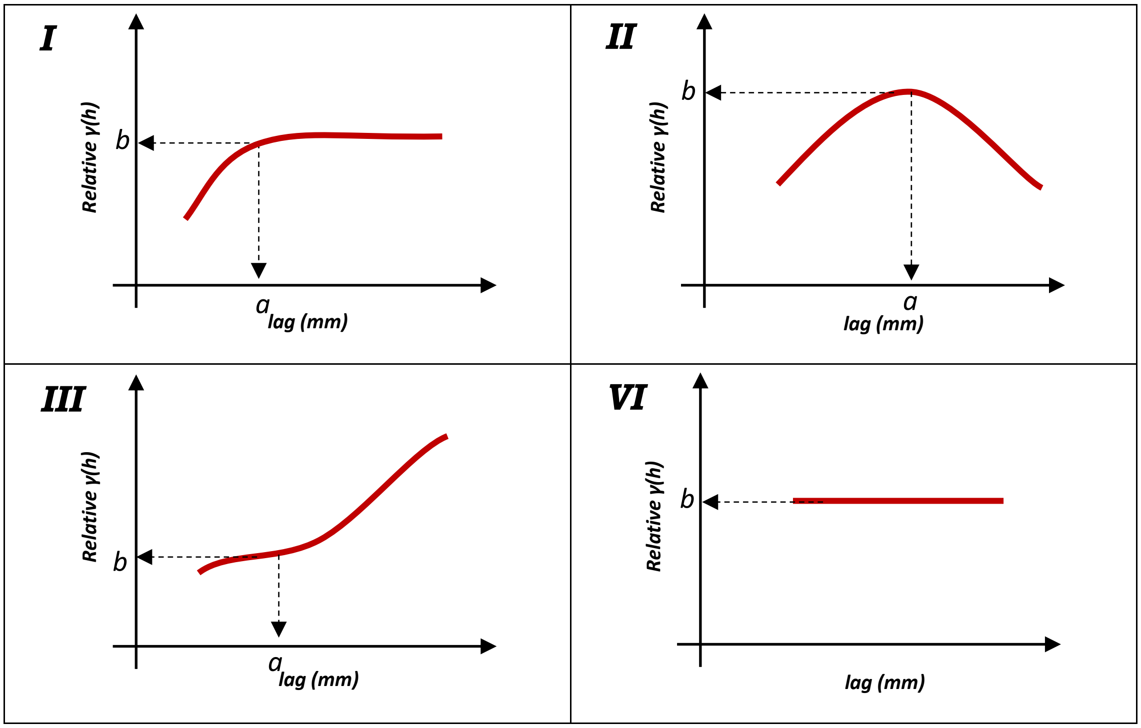

**Figure 3.32:** Patterns observed in the experimental variogram.

### ***Variogram type I:***

The discussion presented in the Introduction Section was based on this type of curve, in which the value for the variogram increases for low lag distances up to a lag value, known as range, where the variogram reaches a plateau, that is known as the sill. This type of curve can be modeled using the exponential or spherical equation described in the Methodology Section. Lyman proposed the range and sill of this type of curve, as a measure of the heterogeneity. The range and sill were denoted as "a" and "b" in Figure 3.32 $I$, respectively. The suitability of the range and sill value for assessing intraparticle heterogeneity could not be evaluated since this type of curve was observed in a few rock faces. This type of variogram was detected in only one rock face for copper grade and for five rock faces for iron grade.

### ***Variogram type II:***

This type of curve was observed for a few faces, mainly in faces with copper mineral veins. This is an example of how the variogram is influenced by a structure present in the texture as was mentioned by Lyman. The veins can be modeled as a banded structure, where the variogram increases up to a maximum value and then decreases to a value close to zero. For a better understanding of this type of curve, an example of one rock face analysed is presented in Figure 3.33.

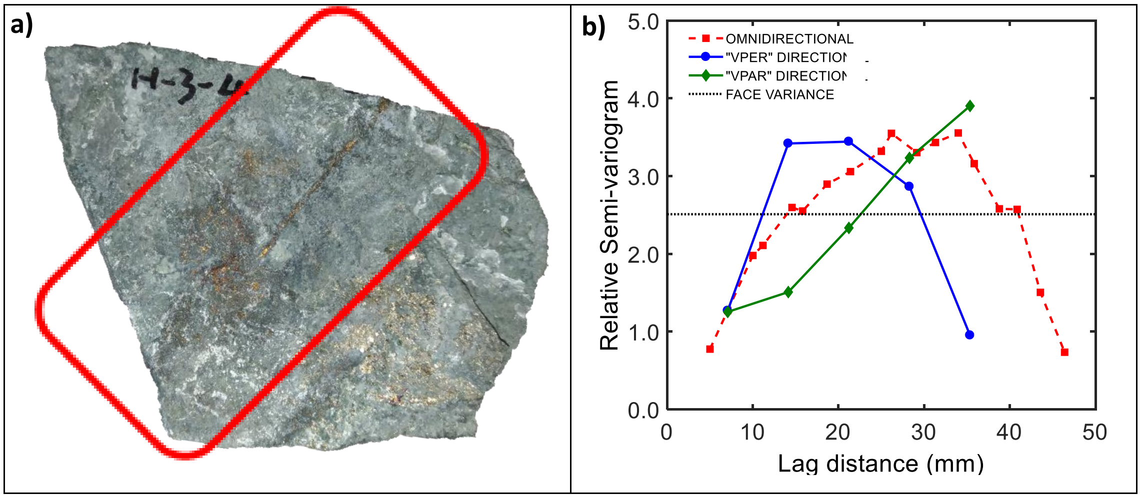

**Figure 3.33**: **a)** Copper vein denoted in a red box for Rock H-3 Face 4; **b)** Variogram plot showing the omnidirectional, two directional variograms (one parallel and another one perpendicular to the vein observed in (a)), and the face variance for rock H-3 face 4.

Thus far, when calculating the omnidirectional variograms, the direction of the separation vector was ignored, assuming that the structure of spatial correlation was independent of direction. In a more thorough analysis, the variogram should be analyzed not only in lag distance but also in direction (Clark, 1987). When plotting directional variograms, frequently in two or four directions, different ranges, known as geometric anisotropy, different scales, known as zonal anisotropy, and different shapes or trends, can be observed.

Two directional variograms were calculated for rock H-3 face 4, one in parallel and another in perpendicular direction to the copper vein that is shown in red in Figure 3.33a. As can be observed in Figure 3.33b, the curve obtained for the parallel variogram presents a different shape when comparing to the perpendicular variogram. The parallel variogram continuously increases for the lag range plotted. However, the perpendicular variogram is similar to the one obtained for the omnidirectional variogram, which increases for small lags up to a point where it reaches a maximum and then decreases to a value close to the one obtained for small lags. The lag value where the curve reaches its maximum can be attributed to the "influence" zone of the vein, since copper was not only detected at the vein, but also in a band adjacent to the vein. This thorough analysis showed geometric anisotropy in this type of curve.

The value "a" marked in Figure 3.32 $II$, represents the distance where the curve reaches its maximum and is equal to a half width of the copper vein band. For most of the faces, this value varies between 20 to 30 mm, indicating that copper veins band were between 40 to 60 mm in width. According to the mapping data, it was observed that copper was concentrated in vein bands, which is consistent to the mineralization pattern present in these two samples, where copper is mainly in veinlets or veins. This result may indicate that the optimum particle size for sorting is equal to the band width. However, there are some conditions that can affect this, such as the vein densities, in other words, the distance between veins. The other factor that should be mentioned is that only 10 rocks were analyzed, thus, it is not possible to generalize the results from this work to the entire deposit. The aim of this work was to develop and to design a method for XRF mapping, not to evaluate the sortability of the ore analysed.

Regarding value "b", it shows the maximum variance reached by the curve. It was observed in most of the faces that this value depends on the copper content of the veins; the higher the copper content, the higher the value "b".

### ***Variogram type III:***

The spatial structures described by the curves type $I$ and $II$ are relatively simple and the correlation of the data points is at one scale. However, it might be possible to have nested models to fit to the data. In fact, there might be multiple spatial structures within the field at different spatial scales. The curve type $III$ is an example of multiple spatial structures, since for this type of curve, two structures are observed, one for short lag distances and another one for longer lag distances. Figure 3.34 shows rock L-5 face 1, and the omnidirectional and two directional variograms, as well as the face variance.

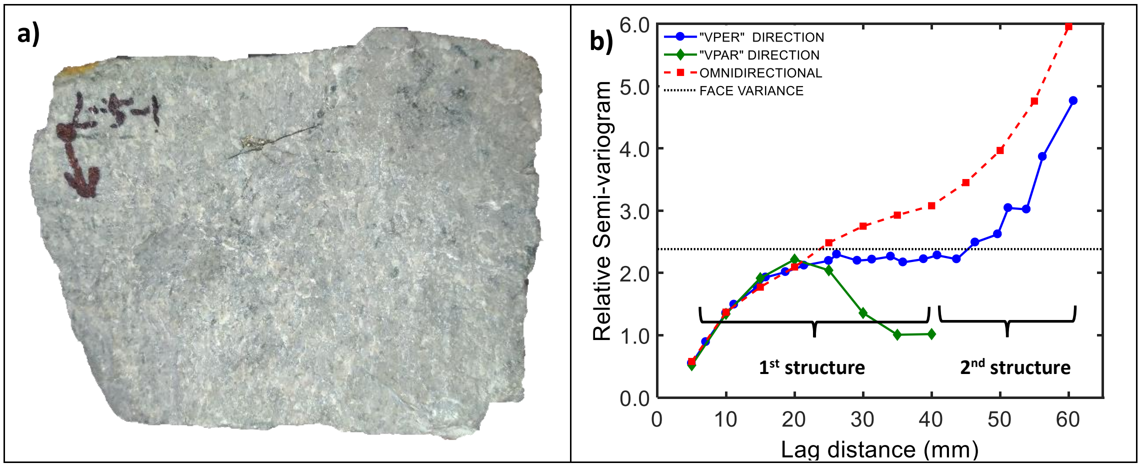

**Figure 3.34: a)** Mineral texture for Rock H-5 Face 1; **b)** variogram plot showing the omnidirectional, two directional variograms, in perpendicular directions, and the face variance for rock H-5 face 1. Note: the ranges of the two structures detected in this variogram type are shown in black.

The omnidirectional variogram for rock H-5 face 1 shows two structures. The first one is similar to curve type $I$, and covers lag distances from 0 to 40 mm. The second one is represented by an increasing slope up to the maximum lag distance plotted. In the literature, this type of curve is explained as two structures taking place at the same time but at different scales. For the second structure, only part of the curve is observed since the lag distances analyzed were not long enough in order to cover the full range of this structure. For this curve, the value “a” indicates the lag distance at which the limit between the first and the second structure was found. The value “b” represents the relative variogram value at which the change from one structure to the other one was observed. These two structures at different lag range values indicate the presence of zonal anisotropy for copper and iron grade in the rock faces, for which this kind of curve was observed.

When analyzing the directional variograms shown in Figure 3.34b, different trends were observed depending on the variogram direction. For that rock face, the directions were randomly selected since no spatial arrangement was observed through the visual inspection of the rock. Despite this lack of spatial arrangement, in the parallel direction curve type $II$ was detected, which means that in the parallel direction the copper grades were present in a band structure. However, in the perpendicular direction, the trend detected was the same as the trend observed in the omnidirectional variogram. In this direction, the structures described above for the omnidirectional are even more pronounced, with a sill value at the same value as the face variance. The difference in trend for these two perpendicular directions showed geometric anisotropy for copper and iron grade in the rock faces, for which this kind of curve was observed.

### ***Variogram type $\mathbf{IV}$:***

The type $IV$ variogram is shown in Figure 3.32 $IV$, and is represented by a horizontal line. In this case, there is no spatial structure at the scale analyzed, which means that the process is random. There is either too much noise in the data or the variable effectively does not exhibit any spatial correlation at the scale plotted and under the conditions used to collect the data. This variogram type is generally attributed to what is known as a “nugget effect”.

The nugget effect can be explained by measurement errors, spatial sources of variation at distances smaller than the sampling interval, or sample size. Measurement error occurs due to the error inherent in measuring devices, but in this work, it was shown that the error introduced by the XRF device is smaller than the variability detected in copper and iron grade. Natural phenomena like copper and iron distribution can vary spatially over a range of scales, as explained with the type $III$ curve, and autocorrelation at scales smaller than the sampling distances will not appear in the variogram. In those cases, the horizontal trend detected can be attributed to the sill of the first curve type presented in this section. The influence of the sample size was discussed in the Introduction Section, based on the work done by Lyman.

The type of variogram observed for each rock face for copper data is presented in Table 3.10, along with its corresponding values for constant “a” and “b”, as shown in Figure 3.32 .

**Table 3.10:** Type of variogram for copper data in each rock face, with its corresponding "a" and "b" value.

| Face ID | Variogram Type | a (mm) | b | Face ID | Variogram Type | a (mm) | b |
|---|---|---|---|---|---|---|---|
| *H-1-1* | III | 14 | 0.39 | *L-1-1* | IV | ----- | 0.24 |
| *H-1-2* | III | 18 | 0.41 | *L-1-2* | II | 16 | 1.05 |
| *H-1-3* | III | 19 | 1.00 | *L-1-3* | IV | ----- | 0.90 |
| *H-1-4* | III | 22 | 0.40 | *L-1-4* | IV | ----- | 0.30 |
| *H-2-1* | II | 26 | 1.90 | *L-2-1*[a] | ----- | ----- | ----- |
| *H-2-2* | III | 23 | 0.80 | *L-2-2* | III | 30 | 2.20 |
| *H-2-3* | III | 15 | 0.65 | *L-2-3* | III | 32 | 1.10 |
| *H-2-4* | IV | ----- | 0.11 | *L-2-4* | IV | ----- | 0.17 |
| *H-3-1* | II | 39 | 0.17 | *L-3-1* | II | 19 | 0.60 |
| *H-3-2* | II | 26 | 4.25 | *L-3-2* | II | 27 | 1.60 |
| *H-3-3* | IV | ----- | 1.25 | *L-3-3* | II | 19 | 0.21 |
| *H-3-4* | II | 31 | 3.5 | *L-3-4* | III | 25 | 0.22 |
| *H-4-1* | II | 38 | 0.29 | *L-4-1* | III | 40 | 0.50 |
| *H-4-2* | II | 25 | 0.25 | *L-4-2* | II | 41 | 1.35 |
| *H-4-3* | III | 26 | 0.30 | *L-4-3* | IV | ----- | 0.32 |
| *H-4-4* | II | 25 | 2.60 | *L-4-4* | III | 12 | 0.60 |
| *H-5-1* | II | 25 | 2.50 | *L-5-1* | III | 44 | 2.20 |
| *H-5-2* | III | 20 | 1.00 | *L-5-2* | III | 13 | 1.50 |
| *H-5-3* | III | 28 | 2.00 | *L-5-3* | III | 43 | 3.10 |
| *H-5-4* | II | 30 | 1.40 | *L-5-4* | I | 22 | 0.82 |

[a] Copper was not detected.

As explained above, the type of variogram curve was assigned to the variogram calculated for each rock face, based on the trend observed in each case. For copper grade, variogram type II and III were the types detected in most cases, as shown Table 3.10. The observation that variogram type II was the most observed was consistent with the type of copper mineralization, which is in veins.

High variability was observed for the values "a" and "b", within each rock and between rocks, which contributes to the observation related to the high degree of intraparticle heterogeneity within each rock, present in both samples. In one rock, rock H-1, the same type of variogram was assigned to all its rock faces.

Table 3.11 shows the type of variogram observed in each rock face for the iron data, along with its corresponding values for constant "a" and "b", as shown in Figure 3.32.

**Table 3.11**: Type of variogram for iron data in each rock face, with its corresponding “a” and “b” value.

| Face ID | Variogram Type | a (mm) | b | Face ID | Variogram Type | a (mm) | b |
|---|---|---|---|---|---|---|---|
| *H-1-1* | III | 35 | 0.027 | *L-1-1* | III | 23 | 0.022 |
| *H-1-2* | III | 30 | 0.060 | *L-1-2* | II | 19 | 0.110 |
| *H-1-3* | III | 22 | 0.038 | *L-1-3* | II | 15 | 0.190 |
| *H-1-4* | II | 21 | 0.092 | *L-1-4* | IV | ----- | 0.040 |
| *H-2-1* | II | 26 | 1.900 | *L-2-1* | IV | ----- | 0.070 |
| *H-2-2* | IV | ----- | 0.170 | *L-2-2* | III | 30 | 0.080 |
| *H-2-3* | I | 22 | 0.350 | *L-2-3* | IV | ----- | 0.090 |
| *H-2-4* | III | ----- | ----- | *L-2-4* | III | ----- | ----- |
| *H-3-1* | II | 38 | 0.110 | *L-3-1* | II | 17 | 0.110 |
| *H-3-2* | IV | ----- | 0.033 | *L-3-2* | III | 37 | 0.045 |
| *H-3-3* | II | 34 | 0.140 | *L-3-3* | II | 16 | 0.190 |
| *H-3-4* | I | 26 | 0.530 | *L-3-4* | I | 25 | 0.260 |
| *H-4-1* | III | 40 | 0.048 | *L-4-1* | II | 32 | 0.120 |
| *H-4-2* | II | 23 | 0.027 | *L-4-2* | I | 24 | 0.028 |
| *H-4-3* | III | 27 | 0.050 | *L-4-3* | III | 22 | 0.045 |
| *H-4-4* | III | 22 | 0.029 | *L-4-4* | II | 22 | 0.035 |
| *H-5-1* | II | 23 | 0.035 | *L-5-1* | III | 29 | 0.060 |
| *H-5-2* | III | 20 | 0.080 | *L-5-2* | II | 33 | 0.060 |
| *H-5-3* | II | 30 | 0.023 | *L-5-3* | II | 25 | 0.067 |
| *H-5-4* | III | 18 | 0.009 | *L-5-4* | I | 23 | 0.068 |

The same variability described above for the variograms of the copper data was observed for the variograms of the iron data, as can be seen in Table 3.11. Variogram type $II$ and $III$ were the types assigned in most cases for iron variograms. In this case, there was no rock with the same variogram type assigned to all its faces, which shows how heterogenous the rocks were. However, when comparing iron data variograms to copper data variograms, it can be observed that the “b” values were lower for iron. This difference was expected considering the results obtained in the intraparticle heterogeneity assessment in one dimension, where the variability for copper data was higher than the variability for iron data.

### 3.5.2 Summary

The omnidirectional variograms were calculated for copper and iron data. Four types of variograms were observed. The range and sill of the typical variogram curve could not be evaluated, for the conditions of analysis, as a measure of heterogeneity since this type of curve was only observed for a few rock faces. The conditions include the distance between sampling points, the sample area and the size of the rocks. This fact does not imply that there was no autocorrelation between the samples but other structures were identified. Variogram type $II$ was one of the most observed, which was consistent with the type of copper mineralization found in the two samples analyzed, HG and LG. The mineralization is structurally controlled with copper occurring mainly as chalcopyrite in trending veins, vein stockworks and fracture fillings. Copper bands of 40 to 60 mm in width were identified at the veins. Geometric and zonal anisotropies were also identified, associated to the copper mineralization of the rocks.

## 3.6 Evaluation of ore sorting with color mapping

### 3.6.1 Two-color mapping

Maps are a key component of many engineering applications and are very important when it comes to results analysis, as well as to displaying the collected data. Color mapping provides a simple method for determining spatial distributions of elements in a sample. The equipment designed for mineral texture analyses apply color mapping to display their results. These maps provide a simple method for determining mineral association and particle size. The minerals are identified based on the elemental composition analysis at the surfaces (Friel & Lyman, 2006) .

In this work, color mapping was selected to graphically present the data collected for both samples, HG and LG. The color display decision was not as straightforward as when using color in other mapping techniques, since at the scale of mapping of this work, no liberated mineral particles were observed. The elemental composition obtained from each analysis comes from a mixture of minerals and not an individual mineral, which is the case for mapping techniques designed to work with particle sizes below 500 µm.

A two-color map was selected to display the copper data obtained for each spot of the rock face. This mapping method was only applied to the copper data, since this is the valuable metal for the ore analyzed, but this method could be applied to other elements. The aim of this two-color map was to delineate the high and low copper grade zones within each rock face. A threshold value was defined to identify zones with low and high copper grade. This threshold value depends mainly on the sample analyzed and the application or the process that is under evaluation. In this work, the samples were from a low-grade ore, having copper as the main valuable mineral, and the application was sensor-based sorting.

The threshold in copper grade for both samples, HG and LG, was set at 0.08%, which was the copper surface grade that correlates to the cut-off grade (0.19%) of the mine. The correlation applied in this case was calculated using the median grade for each rock (see Figure 3.24). The threshold value was the same that was used in the scenario presented above to understand the importance of intraparticle heterogeneity for XRF sorting. The data points where the copper grade was higher than 0.08% were considered as high grade, and the red color was assigned to them. The data points where the copper grade was lower than 0.08% were considered as low grade, and the blue color was assigned to them.

The contour function of Matlab software was used in order to create a smoother mapping and to delimit high and low-grade zones, with the copper contour line for 0.08% defined as the limit between the zones. The contour line was calculated by interpolation of the lattice data. The area of each rock face was delimited based on the data points collected; it did not recreate the shape of each rock face. The maps were plotted to scale and a scale bar was added to each one.

The color maps were plotted for all the rock faces for copper grade (see Appendix I– Two-color mapping for copper grade (Red color for copper grades higher than 0.08%, blue color for copper grades lower than 0.08%)). Figure 3.35 shows face 1 and 3 of rock H-5 and their corresponding color mapping.

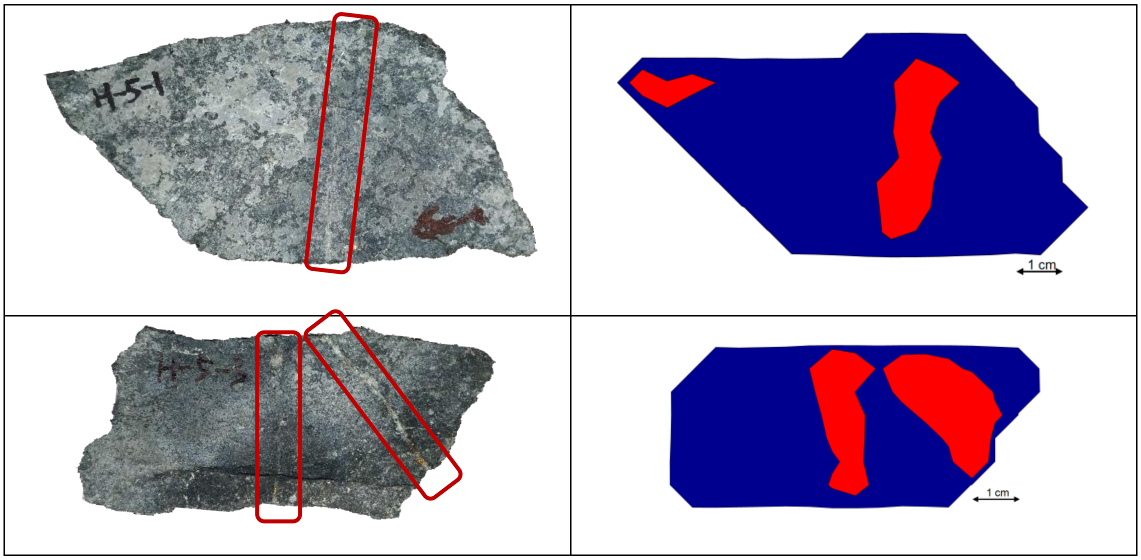

**Figure 3.35**: Face 1 (top) and 3 (bottom) of rock H-5 and their corresponding color mapping Note: red represents high grade and blue represents low grade.

The copper minerals in rock H-5 were found mainly in veins which are shown in red in Figure 3.35. As can be observed, the high-grade zones (red color zones) match with the location of the veins for both faces. As explained above, when discussing the mapping technique, the limitations of the procedure designed was the impossibility to cover the entire face of the rock. The analysis was not performed if the equipment spot size was not fully covered by the rock. Because of this, when approaching the edge of each rock, a small portion of the total rock face area was not analysed. The consequence of this limitation can be observed in the color maps shown in Figure 3.35, for which there is no continuity of the red zone from the center to the edge of the rock face. The red zone should continue to the contour of the rock face.

Figure 3.36 shows another example of the color mapping, for rock L-1 face 1. In this case the copper mineralization is not as clear as in the previous examples presented.

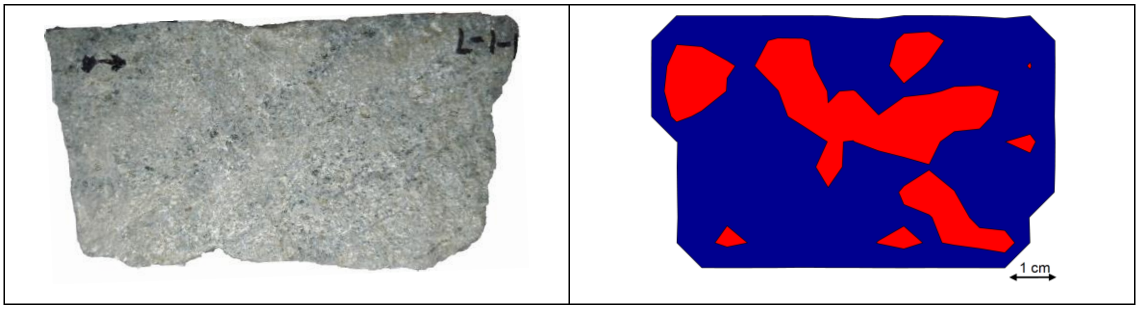

**Figure 3.36**: Face 1 of rock L-1 and its corresponding color mapping. Note: red represents high grade and blue represents low grade.

For rock L-1 face 1, high grade zones are distributed in the rock face in a disseminated arrangement, as can be observed in Figure 3.36. This rock face is an example of how the color mapping can be applied to evaluate the distribution of an element in cases where the mineral spatial arrangement is not directly observable on the rock face.

Another application of the color mapping is to evaluate intraparticle heterogeneity. As previously discussed, intraparticle heterogeneity is an important variable for an XRF sorter, since in this equipment only part of the rock surface is scanned. The variability in copper grade between faces of the same rock can affect the reproducibility of the results obtained in an XRF sorter. To explain this application, the color maps for the four faces of rock L-4 are shown in Figure 3.37.

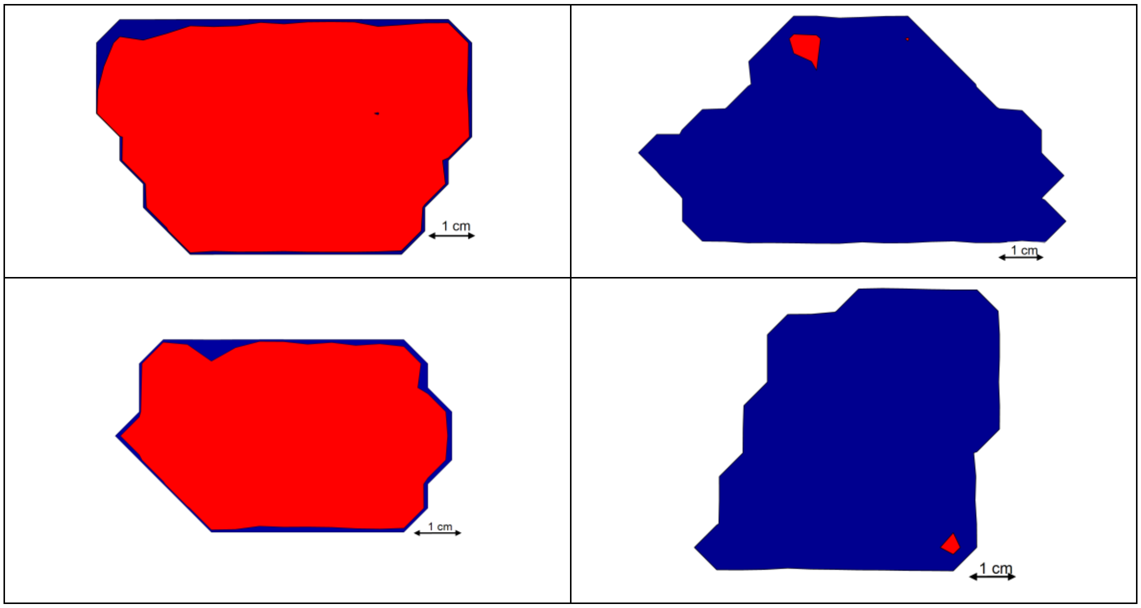

**Figure 3.37:** Color mapping for the four faces mapped of rock L-4. Note: red represents high grade and blue represents low grade.

The variability of rock L-4 is demonstrated in the color mapping when comparing the faces within this rock. Two of them were almost completely red and the other two blue. When detecting this type of response from the color mapping, a potential source of error for a XRF sorter can be inferred.

This color mapping may also be applied to evaluate how size reduction can improve the sorting performance. This evaluation can be interpreted as an analogy of the mineral liberation analysis performed at a smaller particle size. In sensor-based sorting, the target is not to liberate the valuable mineral because this liberation takes place at a much smaller particle size, but to liberate fragments of the rock where the valuable mineral is concentrated. The information shown only refers to the rock surface, which means that it is not a 3D evaluation, but in some cases this information may be enough to evaluate the liberation described. This application is not only for XRF sorting, it could be used for other sensors since the actual element distribution is analyzed. If the valuable element is concentrated in only part of the rock, it may imply that, by breaking the rock, the intraparticle heterogeneity will be reduced and the interparticle heterogeneity will be increased, which improves the sensor-based sorting performance.

### 3.6.2 Summary

Two-color mapping was selected to display the copper data collected for both samples. High and low copper grade zones within each rock face were identified by the red and blue colors, respectively. The threshold value to divide high and low copper grade (0.08%) was calculated from the correlation between surface and bulk copper grade generated with the median copper grade of each rock. Three potential applications of the two-color mapping were presented, 1. characterization of the spatial arrangement of the valuable element, 2. assessment of intraparticle heterogeneity, and 3. evaluation of particle size reduction in sensor-based sorting.

# 4. CONCLUSIONS

The primary motivation of this work was to design and develop a method for rock surface mapping in order to assess intraparticle heterogeneity and to evaluate the correlation between surface grade and bulk grade for run of the mine or primary crushed rocks. The mapping technique developed, as well as the procedure selected to analyse the mapping data, were described and applied to two porphyry copper ore samples, HG and LG. The analysis was focused on copper and iron data since they were part of the valuable minerals of the ore samples, namely chalcopyrite and bornite. The conclusions from this work are summarized below:

- The XRF mapping technique designed and developed was able to scan the rock surfaces of the two porphyry copper ore samples analyzed for the size range selected.
- Evaluation of the data distribution applying univariate statistical analysis was proposed as a first step for the analysis of the surface data obtained by the XRF mapping. For the samples analyzed, copper and iron data distributions did not follow either normal or lognormal distributions. Copper data distributions were highly right skewed, with a long tail for high copper grade values. Iron data distributions were, in general, symmetric, and some were slightly right skewed and with short tails.
- The median and median absolute deviation were proposed as the best parameters to summarize the surface grade and intraparticle heterogeneity, respectively, for the copper and iron data generated by the mapping technique developed in this thesis. The median surface grade was the best parameter to correlate surface grade to bulk grade for copper and iron, with coefficients of determination of 0.73 and 0.86, respectively. The good linear correlation achieved showed that the two samples analyzed might be sorted based on their copper surface grade, when sensing four faces of each rock with a handheld XRF device and applying an univariate linear regression model. The implementation of these results at a larger scale highly depends on the capabilities of the XRF sensors used in industrial scale sorters and their ability to detect copper at the range values evaluated in this work. For the copper ore used in this work, with mainly vein type mineralization, the one-dimensional heterogeneity assessment showed a high degree of intraparticle heterogeneity, which may generate poor reproducibility when sensing only one face of each rock.
- The omnidirectional variograms were calculated for copper and iron surface data. Four types of variograms were observed. The range and sill of the typical variogram curve could not be

evaluated as a measure of heterogeneity since this type of variogram was only observed in a few rock faces. Copper grade bands of 40 to 60 mm in width were identified at the veins. Geometric and zonal anisotropies were also identified, associated to the copper mineralization of the rocks.

- Two-color mapping method was selected to display the data collected in the XRF mapping for both samples analyzed. High and low copper grade zones within each rock face were identified by the red and blue color, respectively. The threshold value to divide in high and low grade (0.08%) was calculated from the correlation between surface and bulk copper grade generated with the median copper grade of each rock. Three potential applications of the two-color mapping were presented: characterization of the spatial arrangement of the valuable element, assessment of intraparticle heterogeneity, and evaluation of particle size reduction in sensor-based sorting.
- The methods developed in this thesis involved the use of XRF sensors. However, the methods can be applied to other surface sensors such as optical, and laser induced breakdown spectroscopy.

# 5. RECOMMENDATIONS

The research carried out in this thesis may be used as the basis for a wide variety of potential research projects in the future. Technical improvements could also enhance the quality of the results obtained. A list of the recommendations is presented below:

- One of the technical limitation mentioned in this work, was the equipment spot size, which was large. The selection of an XRF handheld device with a collimator to adjust the sampling area will generate higher resolution than the achieved in this work.
- Validation of the data generated by the mapping method developed should be performed. Options that could be applied are mentioned in Results and Discussion Section.
- Another technical improvement that could be analyzed in the future is the automatization of the XRF scanning. This improvement would lead to more reproducible results as well as to reduce the labor hours required to perform the test.
- The application of the method developed in this thesis into a practical, reproducible lab setup and procedure requires more work in terms of collecting a reasonable amount of data to build a robust understanding of the results.
- As shown in the Results and Discussion Section, the degree of intraparticle heterogeneity plays an important role on the accuracy of the grade prediction and should be included into the particle sortability assessments. The design of a protocol to assess ore amenability to sorting is a key challenge for the development sensor based sorting application.
- In terms of the distribution analysis, comparison of the results of this type of copper ore, where copper mineralization was mainly observed in veins, against other type of ores such as one with disseminated copper mineralization may be applicable to evaluate the median as a parameter to summarize the data obtained. Also, this type of test may be useful to evaluate the relation between intraparticle heterogeneity and type of mineralization.

  Modelling of sortability based on probability curves. The development of a correlation of intraparticle heterogeneity to sorting efficiency would lead to a better understanding of the sorting assessment and to generate robust numbers for the economic analysis to the application of sensor based sorting.

# References

Aldrich, J. (1997). R. A. Fisher and the Making of Maximum Likelihood 1 912-1922. *Statistical Science*, *12*(3), 162–176.

Anderson, T., & Darling, D. (1954). A test of goodness-of-fit. *Journal of the American Statistical Association*, *49*(268), 765–9.

Bamber, A., Klein, B., & Scoble, M. J. (2006). Integrated Mining and Processing of Massive Sulphide Ores. In *Proceedings, 39th Annual General Meeting of the Canadian Mineral Processors*. Ottawa, Canada.

Bamber, A., Klein, B., & Stephenson, M. (2006). A methodology for mineralogical evaluation of underground pre-concentration systems and a discussion of potential process concepts. In *Proceedings XXXIII International Mineral Processing Congress* (pp. 253–258). Istanbul, Turkey.

Box, G. E. P., & Cox, D. R. (1964). An Analysis of Transformations. *Journal of the Royal Statistical Society*, *26*(2), 211–252.

Clark, I. (1987). *Practical Geostatistics* (First). Elsevier.

*Copper Mountain Commemorative Book*. (2011). Glacer Media Group.

Friel, J. J., & Lyman, C. E. (2006). Tutorial Review: X-ray Mapping in Electron-Beam Instruments. *Microscopy and Microanalysis*, *12*(1), 2–25.

Gu, Y. (2003). Automated Scanning Electron Microscope Based Mineral Liberation Analysis An Introduction to JKMRC/FEI Mineral Liberation Analyser. *Journal of Minerals and Materials Characterization and Engineering*, *2*(1), 33–41.

Gy, P. (1979). *Sampling of Particulate Materials Theory and Practice* (First). Amsterdam, The Netherlands: Elsevier.

Holbek, P. M., Richard, J., & Frost, G. (2015). NI 43-101 Technical report on resources and reserves of the Copper Mountain Mine , Princeton , British Columbia. *Sedar*, *1*(1), 112.

Jenkins, R., & De Vries, J. L. (1969). *Practical X-Ray Spectrometry* (Second). Eindhoven: N.V. Philips.

Journel, A. G., & Huijbregts, C. J. (2003). *Mining Geostatistics*. Blackburn Press.

Klein, B., & Bamber, A. (2017). Mineral Sorting - Course Notes MINE 508. Vancouver: UBC.

Lyman, G. J. (2011). In situ and particulate material heterogeneity. *5th World Conference on Sampling and Blending*, 3–22.

Matheron, G. (1963). Principles of geostatistics. *Economic Geology*, *58*(8), 1246–1266.

Mazhary, A., & Klein, B. (2015). HETEROGENEITY OF LOW-GRADE ORES AND AMENABILITY TO SENSOR-BASED SORTING. In *47th Annual Meeting og the Canadian Mineral Processors* (pp. 386–400). CIM.

MineSense Technologies Ltd. (2015). Retrieved July 1, 2017, from http://www.minesense.com

Reimann, C., & Filzmoser, P. (2000). Normal and lognormal data distribution in geochemistry: Death of a myth. Consequences for the statistical treatment of geochemical and environmental data. *Environmental Geology*, *39*(9), 1001–1014.

Richter, T. O., van der Gaast, S., Koster, B., Vaars, A., Gieles, R., de Stigter, H. C., … van Weering, T. C. E. (2006). The Avaatech XRF Core Scanner: technical description and applications to NE Atlantic sediments. *Geological Society, London, Special Publications*, *267*(1), 39–50.

Robben, C., Wotruba, H., Robben, M., von Ketelhodt, L., & Kowalczyk, M. (2013). Potential of sensor-based sorting for the gold mining industry. *CIM Journal*, *4*(3), 191–200.

Salter, J. D., & Wyatt, N. P. G. (1991). Sorting in the minerals industry: Past, present and future. *Minerals Engineering*, *4*(7–11), 779–796.

Trauth, M. H. (2007). *MATLAB?? recipes for earth sciences: Third edition*. *MATLAB Recipes for Earth Sciences (Third Edition)* (Third). Potsdam, Germany: Springer.

Wilkie, G. J. (2016). *Rapid Assessment of the Sorting Potential of Copper Porphyry Ores through Modelling of Textures and Grade Distributions - PhD Thesis*. The University of Queensland.

Wotruba, H. (2006). Sensor sorting technology – is the minerals industry missing a chance? *XXIII International Mineral Processing Congress*, 21–29.

Wyman, R. A. (1972). *Selective Electronic Mineral Sorting to 1972*. Ottawa, Canada: Department of Energy, Mines and Resources. Canada.

# APPENDICES

## Appendix A – Elemental composition of each rock

| ***ELEMENT*** | ***UNIT*** | ***SAMPLE ID*** | | | | | | | | | |
|---|---|---|---|---|---|---|---|---|---|---|---|
| | | **H1** | **H2** | **H3** | **H4** | **H5** | **L1** | **L2** | **L3** | **L4** | **L5** |
| *Au* | *ppm* | 0.005 | 0.05 | 0.023 | <0.005 | 0.026 | 0.088 | <0.005 | 0.008 | 0.073 | 0.013 |
| *Ag* | *ppm* | 0.6 | 1.4 | 0.7 | 0.3 | 0.6 | 0.7 | <0.2 | 0.3 | 0.4 | 0.2 |
| *Al* | *%* | 2.66 | 2.22 | 2.88 | 2.88 | 2.79 | 1.58 | 1.6 | 1.85 | 2.89 | 0.74 |
| *As* | *ppm* | 17 | 10 | 12 | 3 | 5 | 5 | 4 | 8 | <2 | 4 |
| *B* | *ppm* | <10 | <10 | 15 | 11 | <10 | <10 | <10 | <10 | <10 | <10 |
| *Ba* | *ppm* | 35 | 19 | 27 | 41 | 62 | 28 | 33 | 21 | 110 | 38 |
| *Be* | *ppm* | <0.5 | <0.5 | 0.5 | <0.5 | <0.5 | 0.7 | 0.8 | <0.5 | <0.5 | 0.6 |
| *Bi* | *ppm* | <2 | <2 | <2 | <2 | 3 | <2 | <2 | 3 | <2 | <2 |
| *Ca* | *%* | 3.42 | 2.53 | 3.64 | 2.38 | 1.49 | 1.91 | 2.6 | 1.48 | 1.73 | 1.34 |
| *Cd* | *ppm* | 0.7 | <0.5 | <0.5 | <0.5 | <0.5 | <0.5 | <0.5 | <0.5 | <0.5 | <0.5 |
| *Co* | *ppm* | 47 | 92 | 30 | 25 | 26 | 9 | 3 | 85 | 28 | 5 |
| *Cr* | *ppm* | 41 | 54 | 35 | 39 | 36 | 47 | 50 | 124 | 45 | 27 |
| *Cu* | *ppm* | 1975 | 4540 | 2492 | 707 | 1555 | 1920 | 67 | 981 | 1185 | 490 |
| *Fe* | *%* | 4.37 | 5.04 | 2.54 | 5.5 | 6.29 | 1.14 | 0.65 | 5.26 | 6.17 | 0.73 |
| *Ga* | *ppm* | 14 | 11 | 10 | 16 | 19 | <10 | <10 | 11 | 15 | <10 |
| *Hg* | *ppm* | <1 | <1 | <1 | <1 | <1 | <1 | <1 | <1 | <1 | <1 |
| *K* | *%* | 0.19 | 0.17 | 0.15 | 0.24 | 0.76 | 0.15 | 0.17 | 0.11 | 1.19 | 0.2 |
| *La* | *ppm* | <10 | <10 | <10 | <10 | <10 | <10 | <10 | <10 | <10 | <10 |
| *Mg* | *%* | 1.56 | 0.9 | 1.34 | 1.56 | 2.74 | 0.97 | 0.91 | 0.93 | 2.07 | 0.79 |
| *Mn* | *ppm* | 420 | 317 | 333 | 413 | 648 | 202 | 230 | 315 | 222 | 137 |
| *Mo* | *ppm* | 2 | 1 | 2 | 1 | <1 | 3 | 4 | 1 | 2 | 23 |
| *Na* | *%* | 0.28 | 0.24 | 0.23 | 0.42 | 0.14 | 0.13 | 0.14 | 0.19 | 0.29 | 0.13 |
| *Ni* | *ppm* | 24 | 24 | 16 | 16 | 15 | 15 | 6 | 100 | 26 | 16 |
| *P* | *ppm* | 1698 | 1576 | 1758 | 1767 | 1851 | 2033 | 1953 | 1078 | 1172 | 1512 |
| *Pb* | *ppm* | 13 | 12 | 10 | 10 | 11 | 12 | 9 | 8 | 10 | 6 |
| *S* | *%* | 2.33 | 3.48 | 1.4 | 1.91 | 0.95 | 0.42 | 0.09 | 2.6 | 0.67 | 0.2 |
| *Sb* | *ppm* | 2 | <2 | 6 | 3 | <2 | <2 | <2 | <2 | 4 | 3 |
| *Sr* | *ppm* | 152 | 151 | 147 | 182 | 85 | 65 | 73 | 88 | 101 | 62 |
| *Ti* | *%* | 0.35 | 0.32 | 0.26 | 0.32 | 0.41 | 0.19 | 0.18 | 0.27 | 0.46 | 0.12 |
| *Tl* | *ppm* | <10 | <10 | <10 | <10 | <10 | <10 | <10 | <10 | <10 | <10 |
| *V* | *ppm* | 202 | 140 | 127 | 228 | 301 | 134 | 97 | 112 | 283 | 76 |
| *W* | *ppm* | <10 | <10 | <10 | <10 | <10 | <10 | <10 | <10 | <10 | <10 |
| *Zn* | *ppm* | 83 | 68 | 59 | 37 | 88 | 47 | 32 | 40 | 24 | 27 |
| *Zr* | *ppm* | 17 | 17 | 14 | 16 | 10 | 9 | 7 | 9 | 10 | 9 |

## Appendix B – Wet analysis and XRF assays comparison

The accuracy of the XRF testing, for copper and iron, was tested by comparing the XRF results, obtained from the powder after pulverizing, to the ICP results**. Figure 1** and **Figure 2** shows the correlation curves for copper and iron respectively.

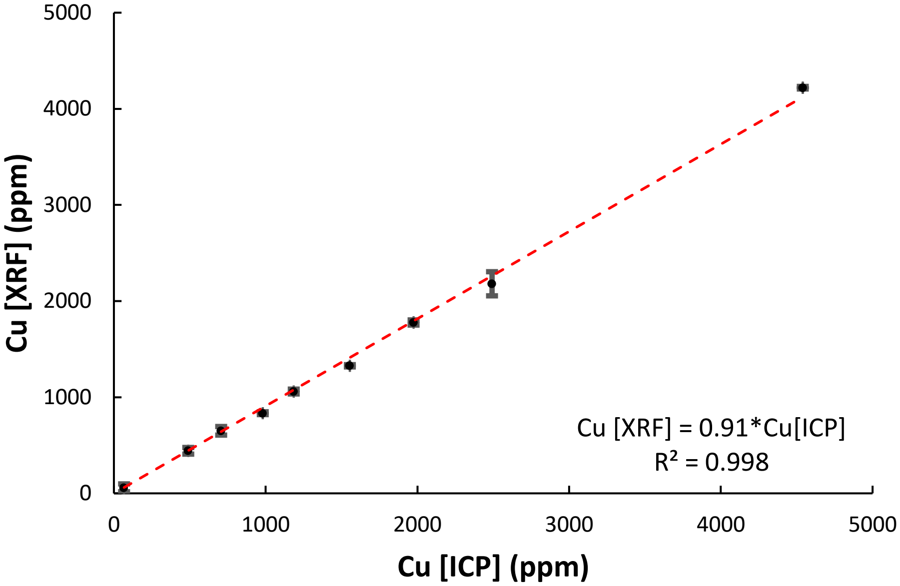

**Figure 1** Correlation curve of XRF copper analysis to ICP copper analysis.

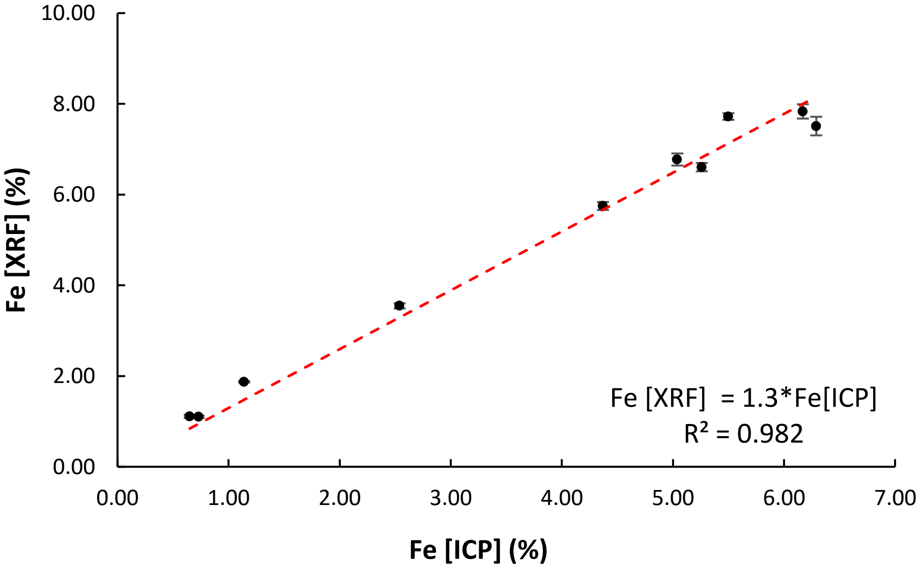

**Figure 2** Correlation curve of XRF iron analysis to ICP iron analysis.

A good fitting, in terms of proportionality, was achieved over the entire range of grades for both elements. XRF measurements were performed by quadruplicate.

# Appendix C – Summary of Anderson-Darling normality test results – copper

| **Face ID** | **Norm. Test / Raw Data** | | **Norm. Test / Log Data** | | **Norm. Test / Power Data** | | |
|---|---|---|---|---|---|---|---|
| | ***Test Result*** | ***p-value*** | ***Test Result*** | ***p-value*** | ***Coefficient*** | ***Test Result*** | ***p-value*** |
| *H-1-1* | 1 | 0.0005 | 1 | 0.0005 | -1.1 | 1 | 0.0005 |
| *H-1-2* | 1 | 0.0005 | 1 | 0.0005 | -1.3 | 1 | 0.0056 |
| *H-1-3* | 1 | 0.0005 | 1 | 0.0005 | -1.3 | 1 | 0.0005 |
| *H-1-4* | 1 | 0.0005 | 1 | 0.0005 | -0.6 | 1 | 0.0173 |
| *H-2-1* | 1 | 0.0005 | 0 | 0.1342 | 0.1 | 0 | 0.2959 |
| *H-2-2* | 1 | 0.0005 | 0 | 0.9900 | 0.1 | 0 | 0.9900 |
| *H-2-3* | 1 | 0.0005 | 1 | 0.0005 | -0.5 | 1 | 0.0279 |
| *H-2-4* | 0 | 0.3624 | 1 | 0.0005 | 1.2 | 0 | 0.4327 |
| *H-3-1* | 1 | 0.0005 | 0 | 0.2132 | 0.2 | 0 | 0.2905 |
| *H-3-2* | 1 | 0.0005 | 1 | 0.0005 | -0.6 | 0 | 0.2486 |
| *H-3-3* | 1 | 0.0005 | 0 | 0.4334 | 0.0 | 0 | 0.5595 |
| *H-3-4* | 1 | 0.0005 | 1 | 0.0005 | -0.1 | 1 | 0.0042 |
| *H-4-1* | 1 | 0.0031 | 0 | 0.2412 | 0.3 | 0 | 0.6933 |
| *H-4-2* | 1 | 0.0005 | 1 | 0.0281 | -0.1 | 1 | 0.0177 |
| *H-4-3* | 1 | 0.0005 | 0 | 0.1800 | -0.4 | 0 | 0.2509 |
| *H-4-4* | 1 | 0.0005 | 1 | 0.0005 | -0.2 | 1 | 0.0006 |
| *H-5-1* | 1 | 0.0005 | 1 | 0.0005 | -0.2 | 1 | 0.0008 |
| *H-5-2* | 1 | 0.0005 | 1 | 0.0421 | -0.1 | 1 | 0.0332 |
| *H-5-3* | 1 | 0.0005 | 1 | 0.0005 | -0.4 | 1 | 0.0005 |
| *H-5-4* | 1 | 0.0005 | 1 | 0.0005 | -0.2 | 1 | 0.0005 |
| *L-1-1* | 1 | 0.0491 | 1 | 0.0005 | 0.6 | 0 | 0.7841 |
| *L-1-2* | 1 | 0.0005 | 0 | 0.0629 | 0.1 | 0 | 0.2434 |
| *L-1-3* | 1 | 0.0005 | 1 | 0.0006 | -0.6 | 0 | 0.2697 |
| *L-1-4* | 1 | 0.0005 | 0 | 0.3694 | -0.2 | 0 | 0.6551 |
| *L-2-1* | ---- | ---- | ---- | ---- | ---- | ---- | ---- |
| *L-2-2* | ---- | ---- | ---- | ---- | ---- | ---- | ---- |
| *L-2-3* | 1 | 0.0005 | 1 | 0.0005 | -0.2 | 1 | 0.0005 |
| *L-2-4* | 0 | 0.6377 | 0 | 0.5334 | 0.4 | 0 | 0.8602 |
| *L-3-1* | 1 | 0.0005 | 0 | 0.3005 | -0.2 | 0 | 0.2857 |
| *L-3-2* | 1 | 0.0006 | 0 | 0.6751 | -0.1 | 0 | 0.6565 |
| *L-3-3* | 1 | 0.0012 | 0 | 0.6668 | -0.2 | 0 | 0.8198 |
| *L-3-4* | 1 | 0.0005 | 1 | 0.0067 | 0.3 | 1 | 0.0257 |
| *L-4-1* | 1 | 0.0005 | 1 | 0.0287 | 0.1 | 0 | 0.1453 |
| *L-4-2* | 1 | 0.0005 | 1 | 0.0005 | 0.2 | 1 | 0.0011 |
| *L-4-3* | 1 | 0.0005 | 0 | 0.6362 | 0.1 | 0 | 0.5831 |
| *L-4-4* | 1 | 0.0005 | 1 | 0.0005 | 0.0 | 1 | 0.0005 |
| *L-5-1* | 1 | 0.0005 | 1 | 0.0005 | -0.2 | 1 | 0.0005 |
| *L-5-2* | 1 | 0.0005 | 1 | 0.0013 | 0.0 | 1 | 0.0011 |
| *L-5-3* | 1 | 0.0005 | 1 | 0.0005 | -0.3 | 1 | 0.0005 |
| *L-5-4* | 1 | 0.0005 | 1 | 0.0005 | 0.2 | 1 | 0.0093 |
| *Total faces* | 38 | ---- | 38 | ---- | ---- | 38 | ---- |
| *Norm. positive* | 2 | ---- | 13 | ---- | ---- | 18 | ---- |
| *%Norm Positive* | 5% | ---- | 34% | ---- | ---- | 47% | ---- |

# Appendix D – Summary of Anderson-Darling normality test results – iron

| **Face ID** | **Norm. Test / Raw Data** | | **Norm. Test / Log Data** | | **Norm. Test / Power Data** | | |
|---|---|---|---|---|---|---|---|
| | ***Test Result*** | ***p-value*** | ***Test Result*** | ***p-value*** | ***Coefficient*** | ***Test Result*** | ***p-value*** |
| *H-1-1* | 1 | 0.0005 | 1 | 0.0039 | -2.3 | 0 | 0.6691 |
| *H-1-2* | 1 | 0.0017 | 0 | 0.2042 | -0.9 | 0 | 0.5465 |
| *H-1-3* | 1 | 0.0215 | 0 | 0.0627 | 0.0 | 0 | 0.0628 |
| *H-1-4* | 1 | 0.0005 | 1 | 0.0005 | 1.7 | 1 | 0.0183 |
| *H-2-1* | 0 | 0.2883 | 0 | 0.7586 | 0.3 | 0 | 0.8520 |
| *H-2-2* | 1 | 0.0005 | 1 | 0.0011 | -1.2 | 0 | 0.6777 |
| *H-2-3* | 1 | 0.0005 | 1 | 0.0016 | -0.9 | 0 | 0.2929 |
| *H-2-4* | 1 | 0.0005 | 1 | 0.0027 | -2.8 | 0 | 0.2413 |
| *H-3-1* | 1 | 0.0005 | 1 | 0.0057 | -0.2 | 1 | 0.0121 |
| *H-3-2* | 1 | 0.0005 | 1 | 0.0005 | -1.7 | 0 | 0.4114 |
| *H-3-3* | 0 | 0.5325 | 0 | 0.0600 | 0.7 | 0 | 0.5114 |
| *H-3-4* | 1 | 0.0005 | 1 | 0.0005 | -0.5 | 0 | 0.0756 |
| *H-4-1* | 0 | 0.7545 | 0 | 0.2907 | 0.4 | 0 | 0.7259 |
| *H-4-2* | 1 | 0.0005 | 1 | 0.0047 | -2.2 | 0 | 0.4871 |
| *H-4-3* | 1 | 0.0005 | 1 | 0.0181 | -1.5 | 0 | 0.3147 |
| *H-4-4* | 1 | 0.0098 | 0 | 0.3723 | -0.3 | 0 | 0.5643 |
| *H-5-1* | 0 | 0.5614 | 0 | 0.8141 | 0.1 | 0 | 0.8503 |
| *H-5-2* | 0 | 0.4479 | 1 | 0.0005 | 1.0 | 0 | 0.4326 |
| *H-5-3* | 0 | 0.5608 | 0 | 0.7319 | -0.1 | 0 | 0.6920 |
| *H-5-4* | 0 | 0.0575 | 0 | 0.2437 | -1.4 | 0 | 0.4489 |
| *L-1-1* | 0 | 0.4276 | 0 | 0.7410 | -0.2 | 0 | 0.6454 |
| *L-1-2* | 1 | 0.0005 | 1 | 0.0005 | -2.3 | 0 | 0.7415 |
| *L-1-3* | 1 | 0.0005 | 1 | 0.0005 | -1.9 | 0 | 0.7643 |
| *L-1-4* | 1 | 0.0005 | 1 | 0.0012 | -1.7 | 0 | 0.1124 |
| *L-2-1* | 1 | 0.0005 | 1 | 0.0158 | -1.1 | 0 | 0.1348 |
| *L-2-2* | 1 | 0.0005 | 1 | 0.0005 | -1.7 | 0 | 0.4962 |
| *L-2-3* | 1 | 0.0005 | 1 | 0.0005 | -2.3 | 0 | 0.9406 |
| *L-2-4* | 0 | 0.4334 | 0 | 0.8223 | -1.3 | 0 | 0.9585 |
| *L-3-1* | 1 | 0.0005 | 0 | 0.0589 | -0.3 | 0 | 0.1970 |
| *L-3-2* | 0 | 0.0513 | 0 | 0.5987 | -0.4 | 0 | 0.6878 |
| *L-3-3* | 1 | 0.0005 | 1 | 0.0005 | -2.1 | 1 | 0.0091 |
| *L-3-4* | 1 | 0.0005 | 1 | 0.0116 | -0.9 | 1 | 0.0159 |
| *L-4-1* | 1 | 0.0005 | 1 | 0.0170 | -0.2 | 1 | 0.0353 |
| *L-4-2* | 1 | 0.0335 | 0 | 0.0859 | 0.2 | 0 | 0.0840 |
| *L-4-3* | 0 | 0.8246 | 0 | 0.1362 | 0.9 | 0 | 0.8320 |
| *L-4-4* | 1 | 0.0052 | 0 | 0.0822 | -0.7 | 0 | 0.1820 |
| *L-5-1* | 1 | 0.0005 | 1 | 0.0121 | -0.7 | 0 | 0.3560 |
| *L-5-2* | 1 | 0.0005 | 0 | 0.0884 | -0.6 | 0 | 0.3205 |
| *L-5-3* | 1 | 0.0005 | 1 | 0.0020 | -1.3 | 0 | 0.8124 |
| *L-5-4* | 0 | 0.3916 | 0 | 0.2444 | 0.4 | 0 | 0.6745 |
| *Total faces* | 40 | ---- | 40 | ---- | ---- | 40 | ---- |
| *Norm. positive* | 12 | ---- | 18 | ---- | ---- | 35 | ---- |
| *%Norm Positive* | 30.00% | ---- | 45.00% | ---- | ---- | 87.50% | ---- |

# Appendix E – Central tendency parameter values per rock – copper

**ARITHMETIC MEAN**

HIGH GRADE SAMPLE

| | ***Bulk*** | ***Rock*** | ***Face 1*** | ***Face 2*** | ***Face 3*** | ***Face 4*** |
|---|---|---|---|---|---|---|
| *H-1* | 0.1975 | 0.0972 | 0.1332 | 0.0640 | 0.1276 | 0.0684 |
| *H-2* | 0.4540 | 0.2999 | 0.3104 | 0.4819 | 0.2365 | 0.0751 |
| *H-3* | 0.2492 | 0.8388 | 2.4667 | 0.0779 | 0.1872 | 0.3324 |
| *H-4* | 0.0707 | 0.0757 | 0.0929 | 0.0312 | 0.0394 | 0.1439 |
| *H-5* | 0.1555 | 0.0931 | 0.0445 | 0.1316 | 0.0885 | 0.1127 |

LOW GRADE SAMPLE

| | ***Bulk*** | ***Rock*** | ***Face 1*** | ***Face 2*** | ***Face 3*** | ***Face 4*** |
|---|---|---|---|---|---|---|
| *L-1* | 0.1920 | 0.1254 | 0.0759 | 0.1184 | 0.1390 | 0.2879 |
| *L-2* | 0.0067 | 0.0083 | 0.0010 | 0.0045 | 0.0130 | 0.0366 |
| *L-3* | 0.0981 | 0.1159 | 0.2083 | 0.0326 | 0.0538 | 0.1124 |
| *L-4* | 0.1185 | 0.3176 | 0.6688 | 0.0244 | 0.6083 | 0.0127 |
| *L-5* | 0.0490 | 0.0240 | 0.0170 | 0.0382 | 0.0131 | 0.0358 |

**GEOMETRIC MEAN**

HIGH GRADE SAMPLE

| | ***Bulk*** | ***Rock*** | ***Face 1*** | ***Face 2*** | ***Face 3*** | ***Face 4*** |
|---|---|---|---|---|---|---|
| *H-1* | 0.1975 | 0.0744 | 0.1059 | 0.0551 | 0.0889 | 0.0576 |
| *H-2* | 0.4540 | 0.1803 | 0.1917 | 0.3169 | 0.1645 | 0.0663 |
| *H-3* | 0.2492 | 0.2053 | 2.3152 | 0.0393 | 0.1171 | 0.1238 |
| *H-4* | 0.0707 | 0.0509 | 0.0834 | 0.0285 | 0.0357 | 0.0751 |
| *H-5* | 0.1555 | 0.0454 | 0.0229 | 0.0768 | 0.0377 | 0.0725 |

LOW GRADE SAMPLE

| | ***Bulk*** | ***Rock*** | ***Face 1*** | ***Face 2*** | ***Face 3*** | ***Face 4*** |
|---|---|---|---|---|---|---|
| *L-1* | 0.1920 | 0.0890 | 0.0653 | 0.0810 | 0.1050 | 0.2523 |
| *L-2* | 0.0067 | 0.0010 | 0.0010 | 0.0010 | 0.0103 | 0.0332 |
| *L-3* | 0.0981 | 0.0792 | 0.1773 | 0.0305 | 0.0501 | 0.0993 |
| *L-4* | 0.1185 | 0.0704 | 0.5150 | 0.0140 | 0.5265 | 0.0090 |
| *L-5* | 0.0490 | 0.0106 | 0.0079 | 0.0158 | 0.0065 | 0.0214 |

**MEDIAN**

HIGH GRADE SAMPLE

| | ***Bulk*** | ***Rock*** | ***Face 1*** | ***Face 2*** | ***Face 3*** | ***Face 4*** |
|---|---|---|---|---|---|---|
| *H-1* | 0.1975 | 0.0614 | 0.0792 | 0.0493 | 0.0583 | 0.0532 |
| *H-2* | 0.4540 | 0.1540 | 0.2313 | 0.3137 | 0.1284 | 0.0739 |
| *H-3* | 0.2492 | 0.1459 | 2.3541 | 0.0310 | 0.1054 | 0.0829 |
| *H-4* | 0.0707 | 0.0430 | 0.0893 | 0.0312 | 0.0352 | 0.0490 |
| *H-5* | 0.1555 | 0.0348 | 0.0184 | 0.0805 | 0.0219 | 0.0496 |

LOW GRADE SAMPLE

| | ***Bulk*** | ***Rock*** | ***Face 1*** | ***Face 2*** | ***Face 3*** | ***Face 4*** |
|---|---|---|---|---|---|---|
| *L-1* | 0.1920 | 0.0879 | 0.0718 | 0.0937 | 0.0913 | 0.2295 |
| *L-2* | 0.0067 | 0.0020 | 0.0010 | 0.0010 | 0.0099 | 0.0346 |
| *L-3* | 0.0981 | 0.0799 | 0.1880 | 0.0307 | 0.0504 | 0.1110 |
| *L-4* | 0.1185 | 0.0648 | 0.5919 | 0.0170 | 0.5052 | 0.0091 |
| *L-5* | 0.0490 | 0.0096 | 0.0076 | 0.0170 | 0.0065 | 0.0227 |

## Appendix F – Central tendency parameter values per rock – iron

### ARITHMETIC MEAN

HIGH GRADE SAMPLE

| | *Bulk* | *Rock* | *Face 1* | *Face 2* | *Face 3* | *Face 4* |
|---|---|---|---|---|---|---|
| *H-1* | 4.3700 | 3.9369 | 5.1666 | 3.0861 | 3.3019 | 3.3923 |
| *H-2* | 5.0400 | 5.4206 | 7.0476 | 4.8068 | 4.5606 | 4.8393 |
| *H-3* | 2.5400 | 4.6851 | 7.7922 | 2.5519 | 4.3864 | 3.7023 |
| *H-4* | 5.5000 | 8.3362 | 12.4249 | 5.3482 | 6.0736 | 8.5966 |
| *H-5* | 6.2900 | 6.5918 | 5.9402 | 8.1382 | 5.6949 | 6.1491 |

LOW GRADE SAMPLE

| | *Bulk* | *Rock* | *Face 1* | *Face 2* | *Face 3* | *Face 4* |
|---|---|---|---|---|---|---|
| *L-1* | 1.1400 | 1.6166 | 1.3833 | 1.4811 | 1.8518 | 2.4172 |
| *L-2* | 0.6500 | 2.3029 | 0.7513 | 0.7788 | 1.8866 | 2.3499 |
| *L-3* | 5.2600 | 7.5108 | 7.3838 | 5.2975 | 6.9091 | 8.1771 |
| *L-4* | 6.1700 | 26.7258 | 36.5521 | 7.5889 | 36.4729 | 7.8964 |
| *L-5* | 0.7300 | 1.0464 | 0.8347 | 1.8188 | 0.8093 | 0.9420 |

### GEOMETRIC MEAN

HIGH GRADE SAMPLE

| | *Bulk* | *Rock* | *Face 1* | *Face 2* | *Face 3* | *Face 4* |
|---|---|---|---|---|---|---|
| *H-1* | 4.3700 | 3.7513 | 5.1104 | 3.0252 | 3.2353 | 3.2585 |
| *H-2* | 5.0400 | 5.0091 | 6.7722 | 4.5370 | 4.1106 | 4.7708 |
| *H-3* | 2.5400 | 4.0125 | 7.5408 | 2.5169 | 4.1878 | 3.1317 |
| *H-4* | 5.5000 | 7.7029 | 12.1556 | 5.3020 | 5.9391 | 8.3947 |
| *H-5* | 6.2900 | 6.3429 | 5.8614 | 7.6198 | 5.6492 | 6.1144 |

LOW GRADE SAMPLE

| | *Bulk* | *Rock* | *Face 1* | *Face 2* | *Face 3* | *Face 4* |
|---|---|---|---|---|---|---|
| *L-1* | 1.1400 | 1.5499 | 1.3708 | 1.4346 | 1.7672 | 2.3743 |
| *L-2* | 0.6500 | 1.6041 | 0.7313 | 0.7479 | 1.8327 | 2.3287 |
| *L-3* | 5.2600 | 7.2284 | 7.1094 | 5.1938 | 6.5440 | 7.6073 |
| *L-4* | 6.1700 | 21.0253 | 35.1495 | 7.4915 | 35.3474 | 7.7961 |
| *L-5* | 0.7300 | 0.9656 | 0.8106 | 1.7827 | 0.7893 | 0.9141 |

### MEDIAN

HIGH GRADE SAMPLE

| | *Bulk* | *Rock* | *Face 1* | *Face 2* | *Face 3* | *Face 4* |
|---|---|---|---|---|---|---|
| *H-1* | 4.3700 | 3.7635 | 4.9629 | 3.0015 | 3.1381 | 3.6176 |
| *H-2* | 5.0400 | 4.7848 | 6.6937 | 4.1585 | 3.7264 | 4.5021 |
| *H-3* | 2.5400 | 3.5782 | 7.4131 | 2.4497 | 4.4232 | 2.8408 |
| *H-4* | 5.5000 | 7.1748 | 12.5149 | 5.2451 | 5.8364 | 8.0806 |
| *H-5* | 6.2900 | 6.1605 | 5.8434 | 8.1812 | 5.6446 | 6.1769 |

LOW GRADE SAMPLE

| | *Bulk* | *Rock* | *Face 1* | *Face 2* | *Face 3* | *Face 4* |
|---|---|---|---|---|---|---|
| *L-1* | 1.1400 | 1.4558 | 1.3740 | 1.3457 | 1.6754 | 2.3583 |
| *L-2* | 0.6500 | 1.5653 | 0.7205 | 0.7074 | 1.7370 | 2.3232 |
| *L-3* | 5.2600 | 7.0070 | 6.8509 | 5.1391 | 5.8223 | 7.5749 |
| *L-4* | 6.1700 | 29.9972 | 34.2503 | 7.4526 | 36.5747 | 7.5701 |
| *L-5* | 0.7300 | 0.8806 | 0.8052 | 1.7682 | 0.7553 | 0.9359 |

# Appendix G – Experimental variograms for copper grade

**H-1-1**

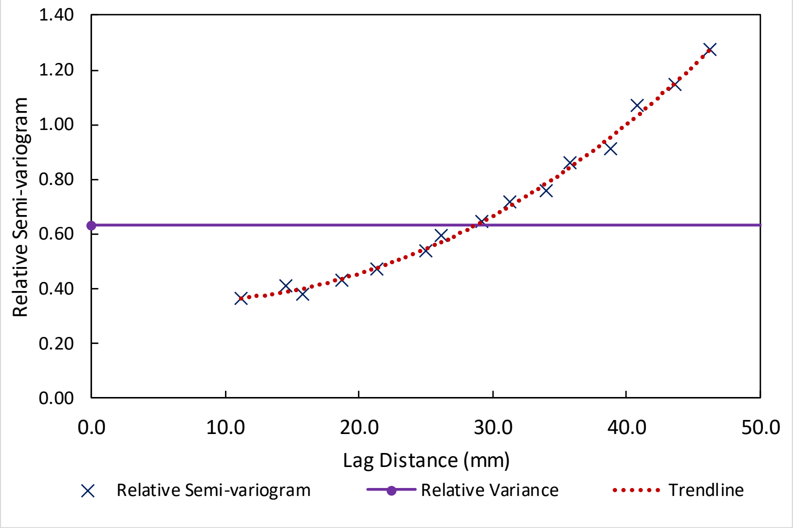

**H-1-2**

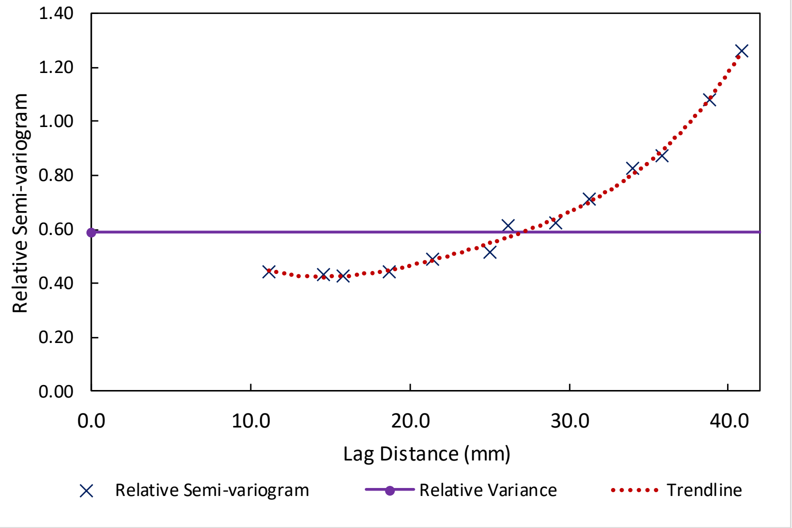

**H-1-3**

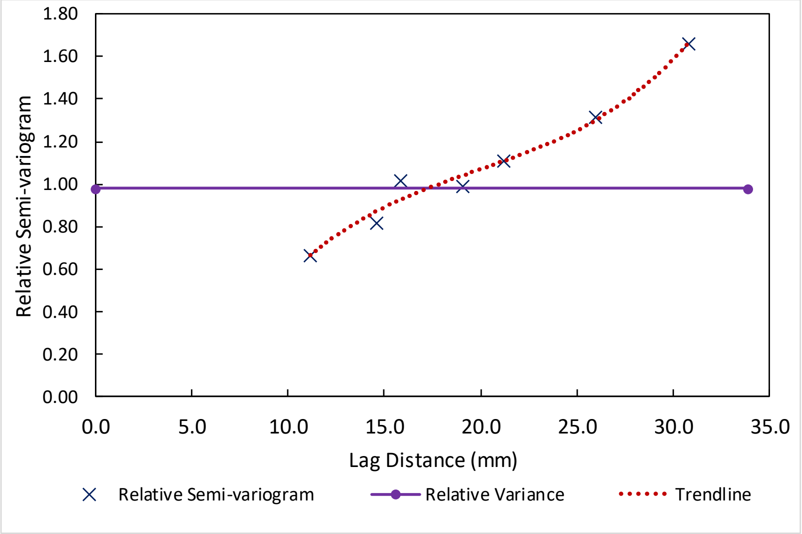

**H-1-4**

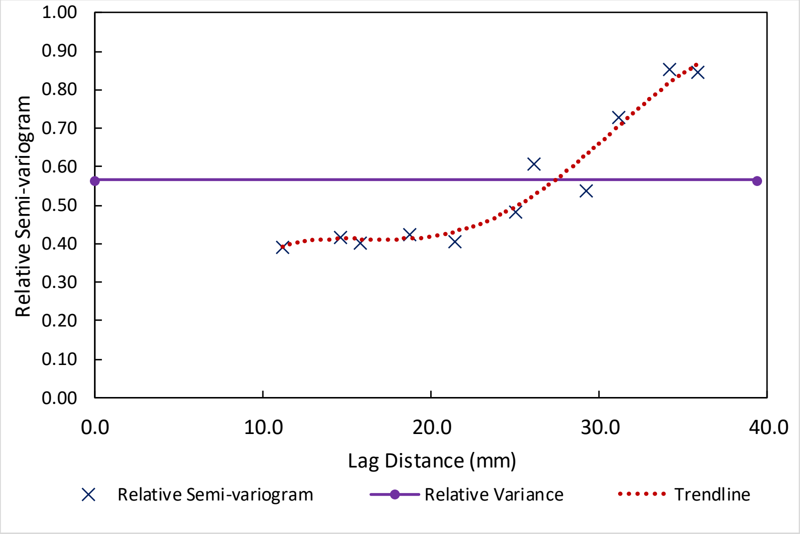

**H-2-1**

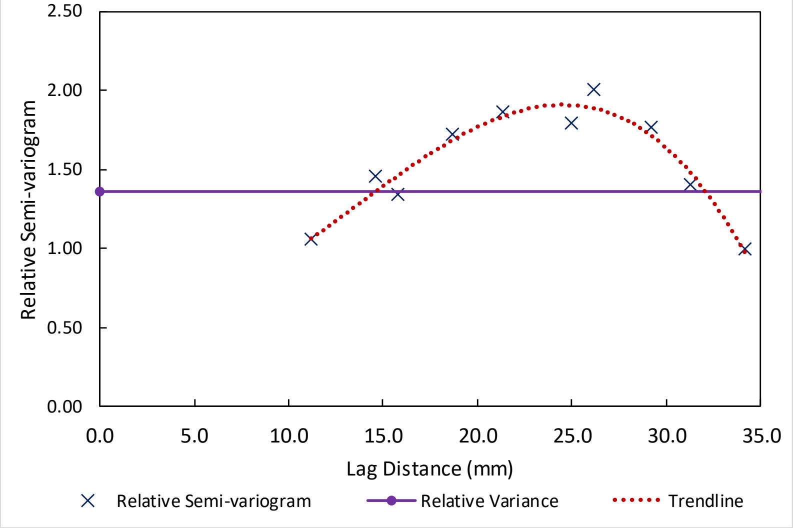

**H-2-2**

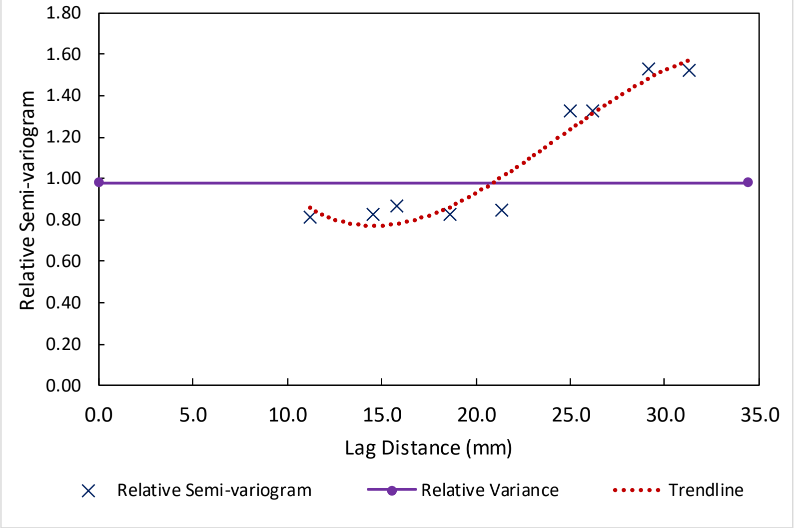

**H-2-3**

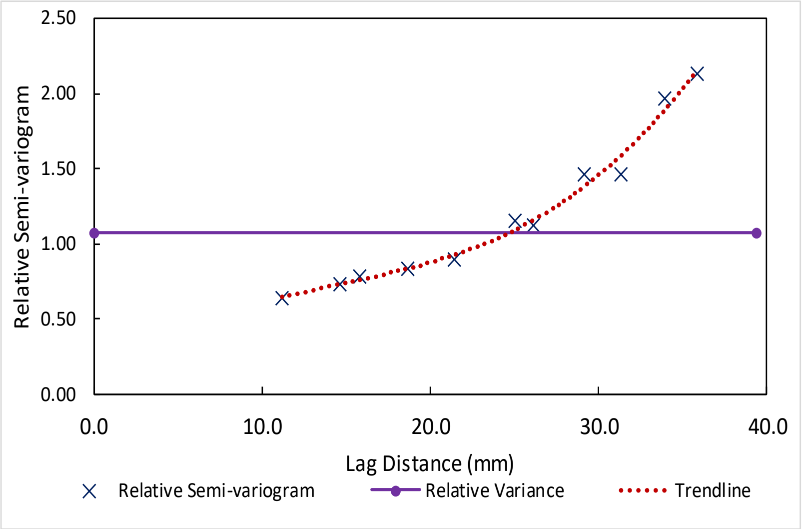

**H-2-4**

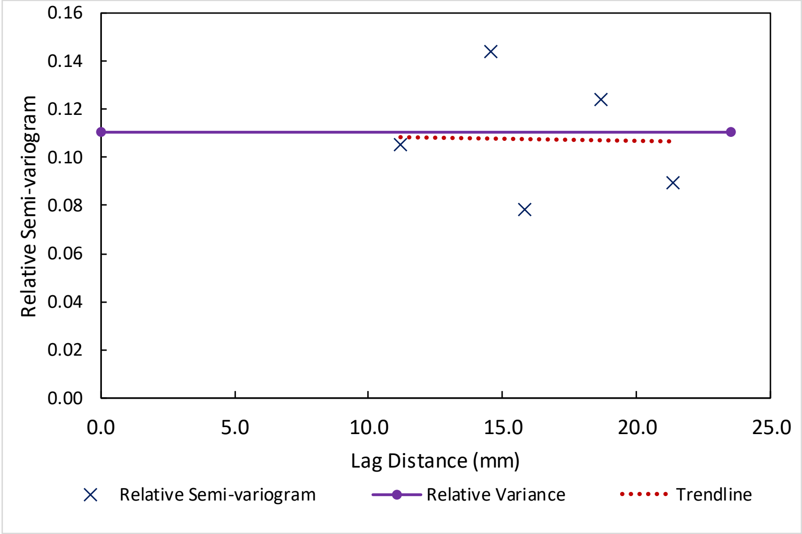

**H-3-1**

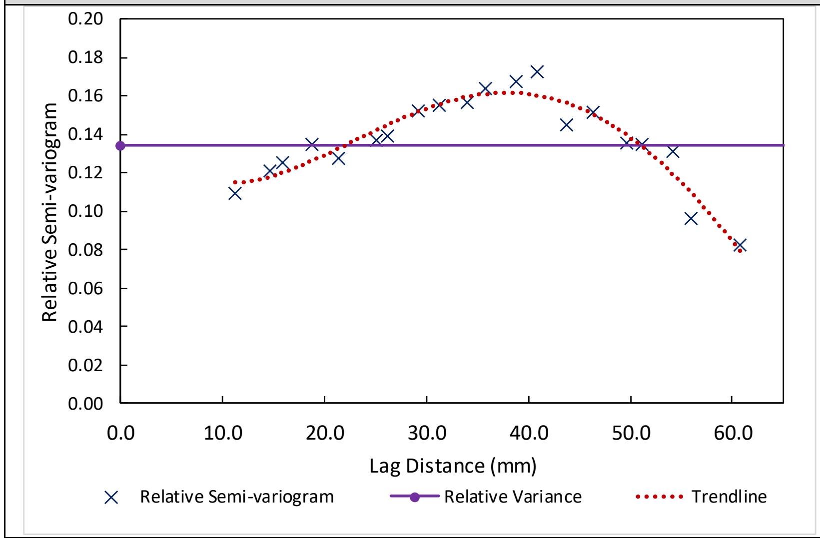

**H-3-2**

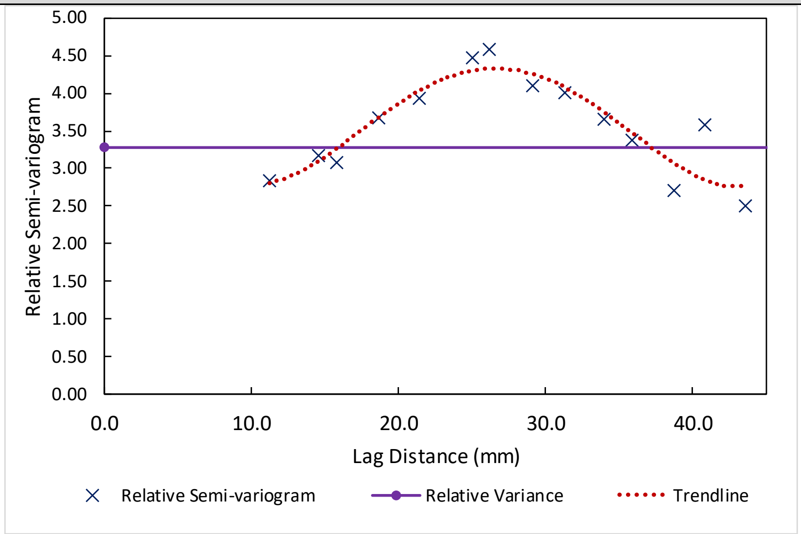

**H-3-3**

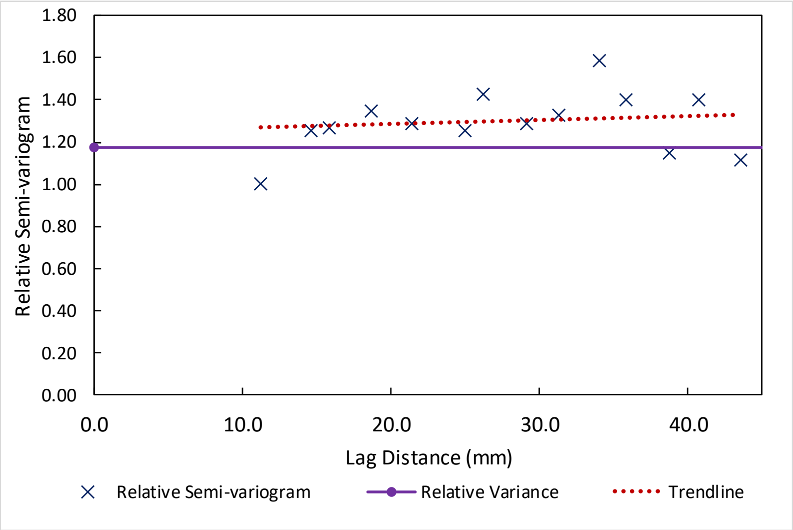

**H-3-4**

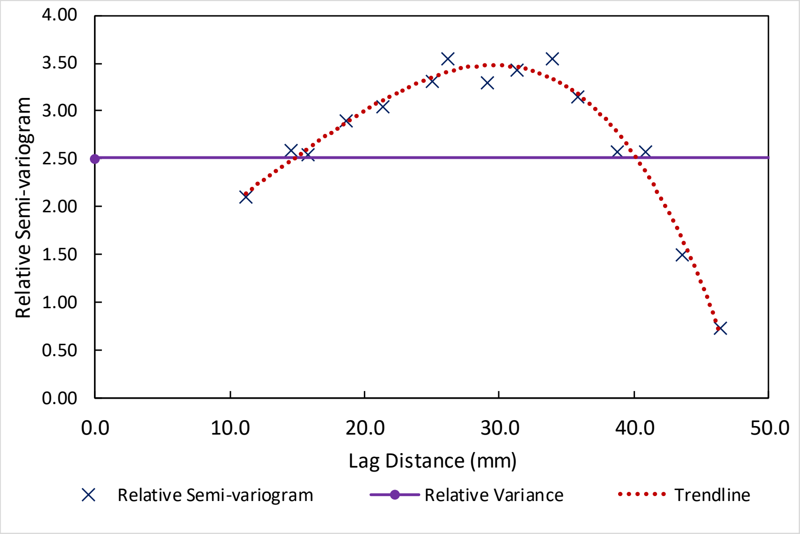

**H-4-1**

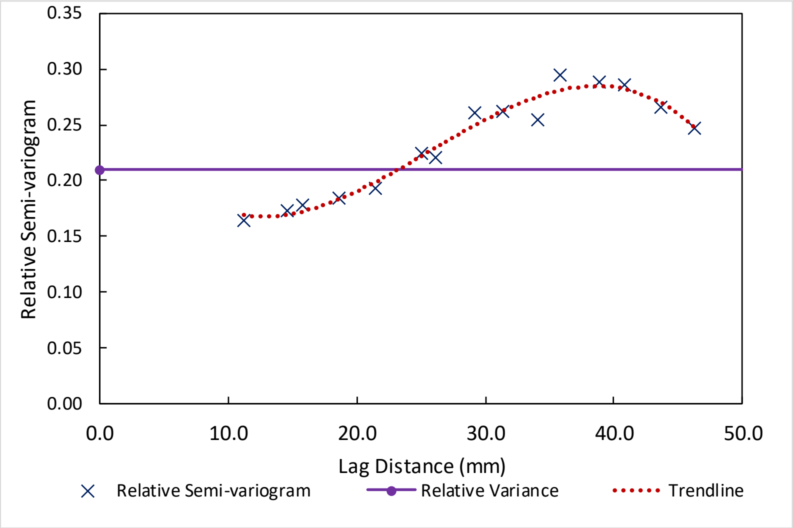

**H-4-2**

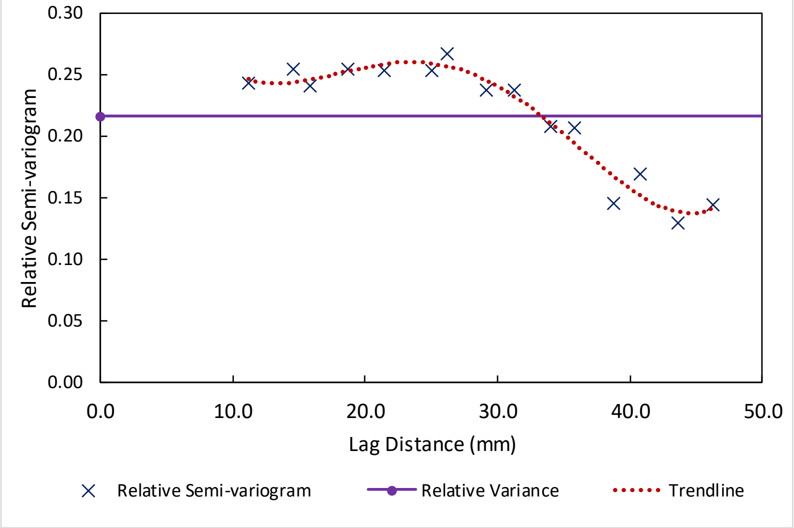

**H-4-3**

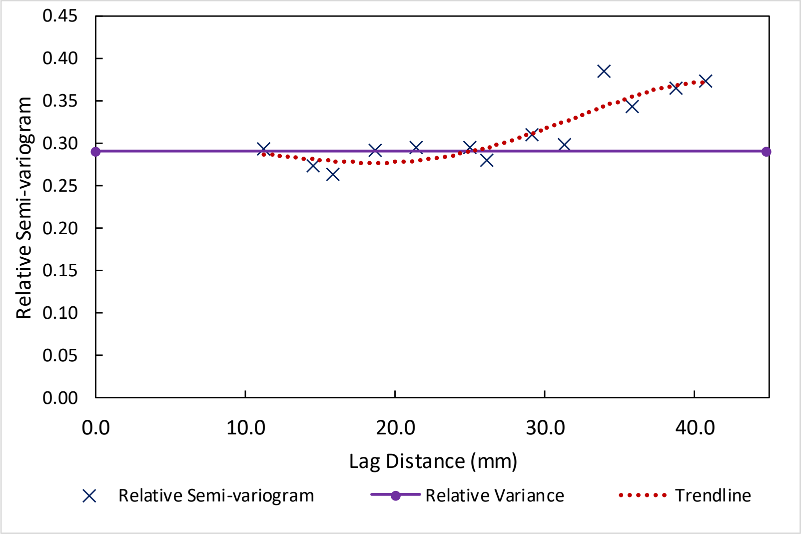

**H-4-4**

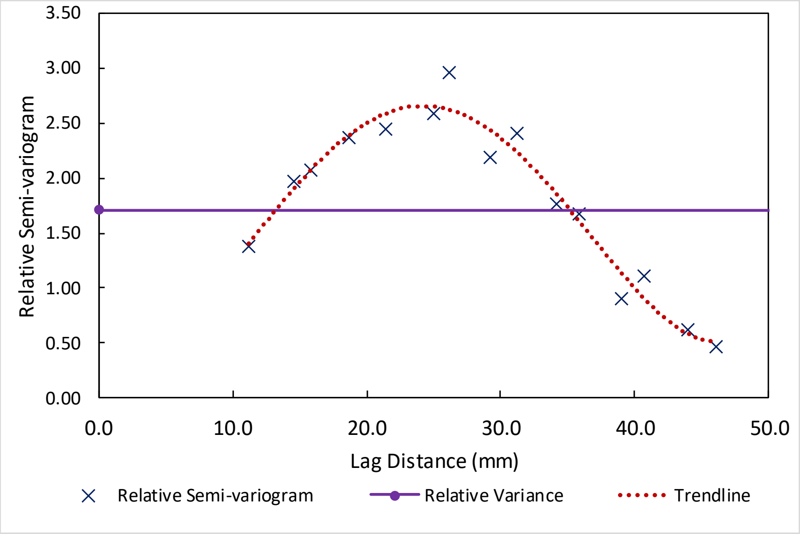

**H-5-1**

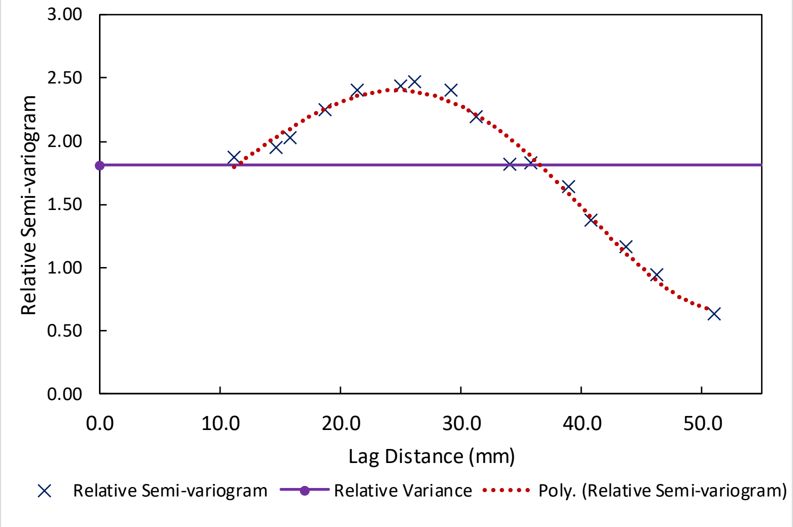

**H-5-2**

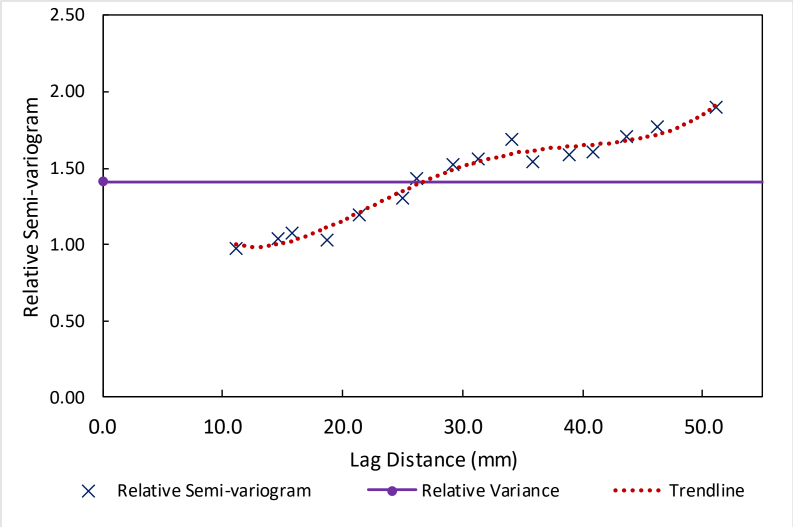

**H-5-3**

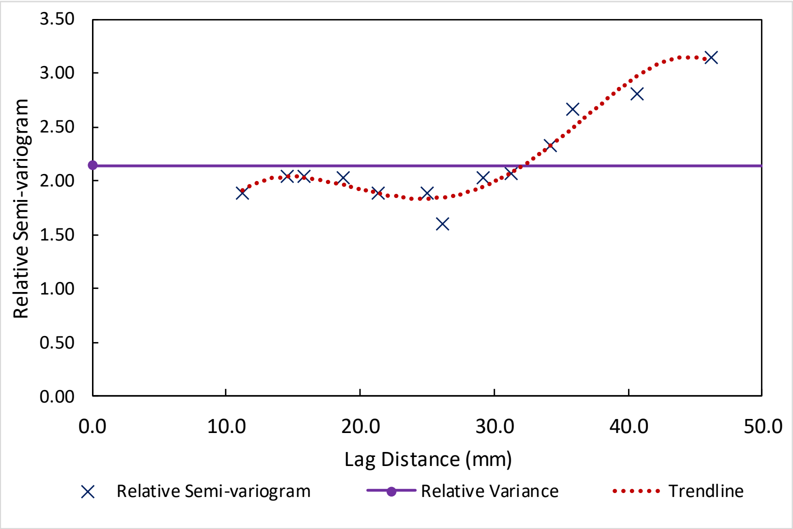

**H-5-4**

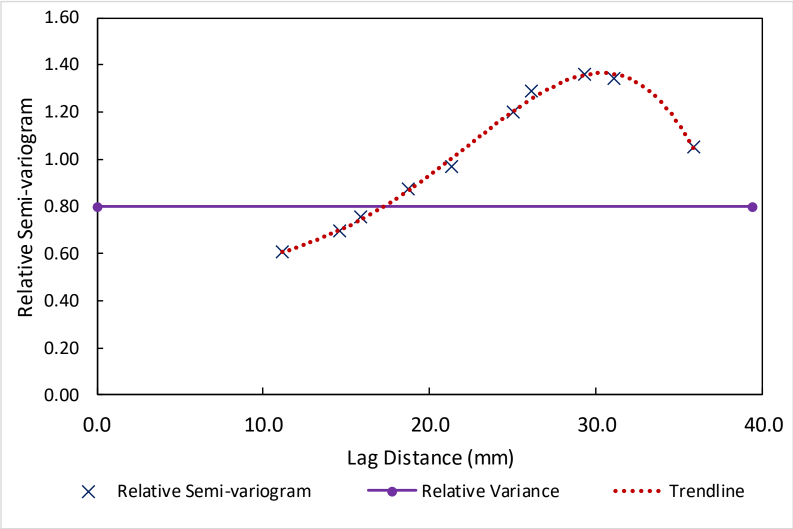

**L-1-1**

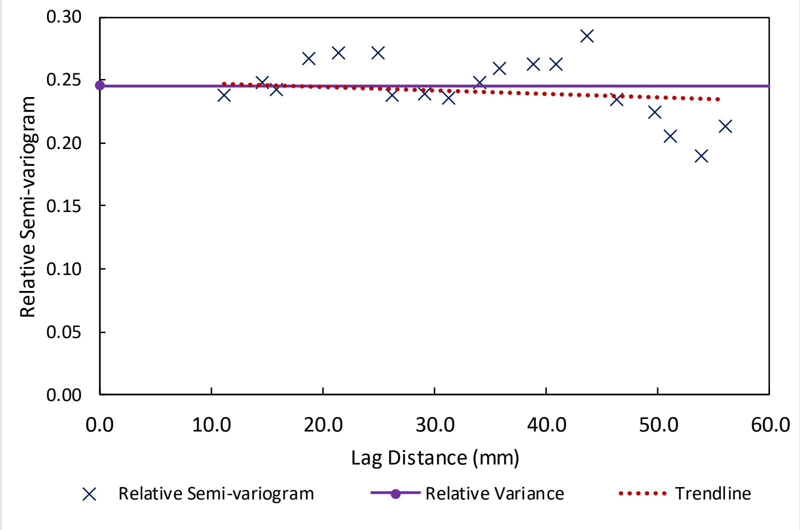

**L-1-2**

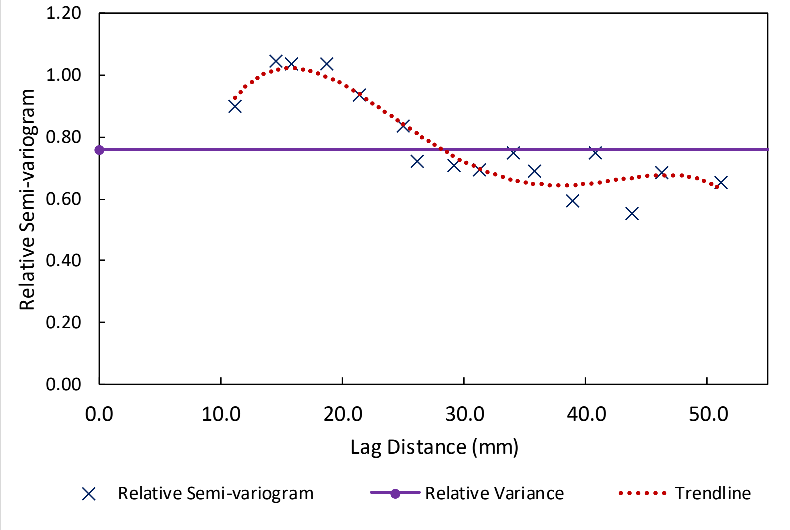

**L-1-3**

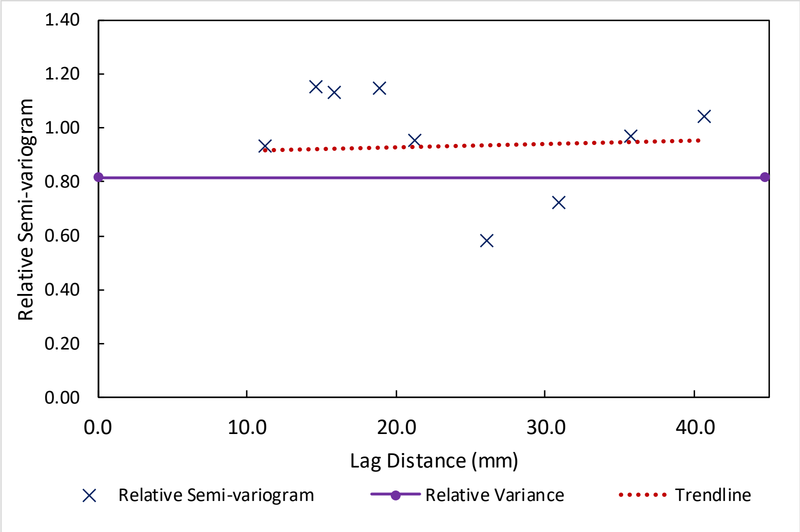

**L-1-4**

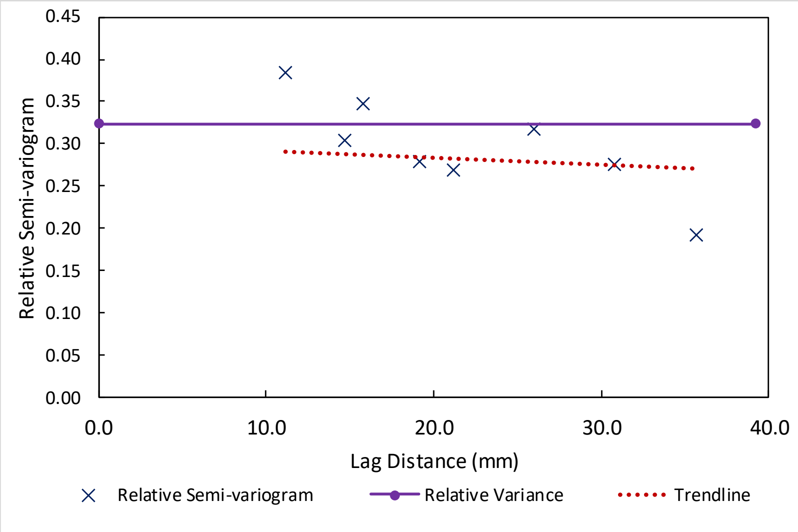

## L-2-1

**COPPER GRADES BELOW LIMIT OF DETECTION**

## L-2-2

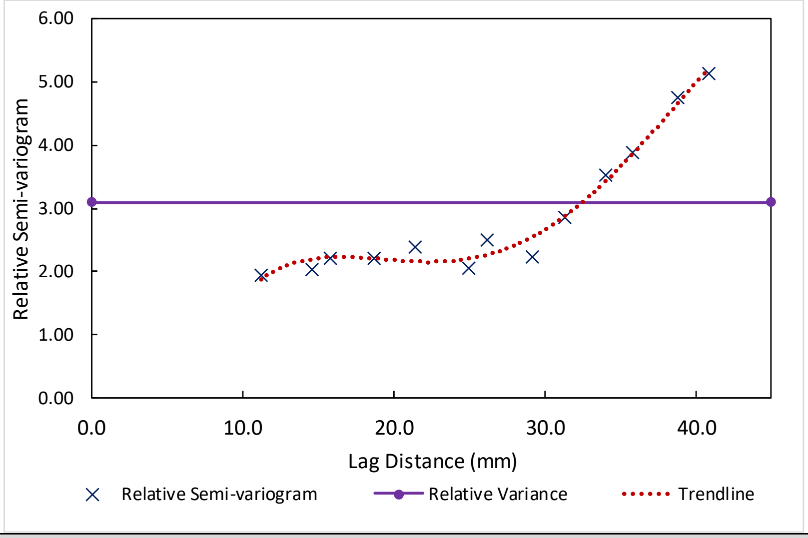

## L-2-3

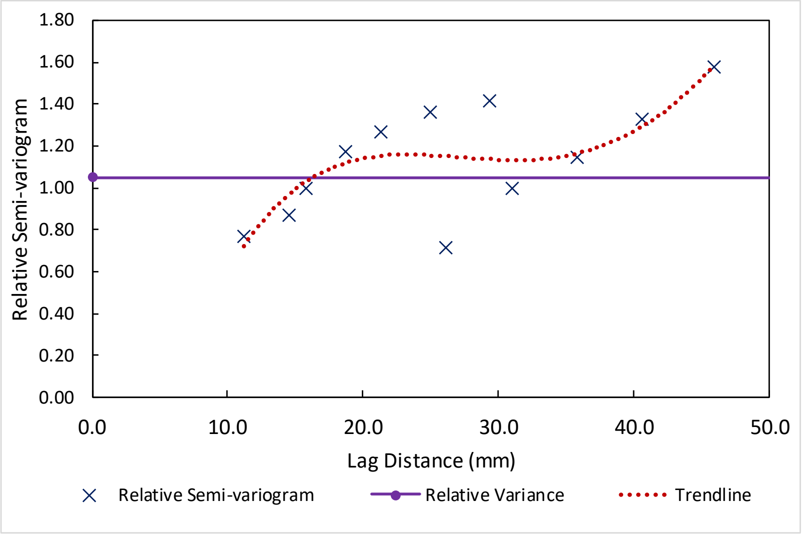

## L-2-4

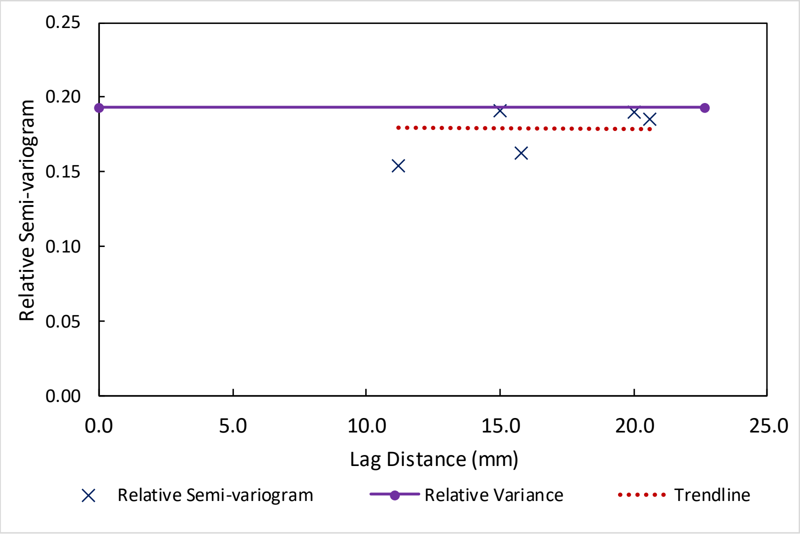

**L-3-1**

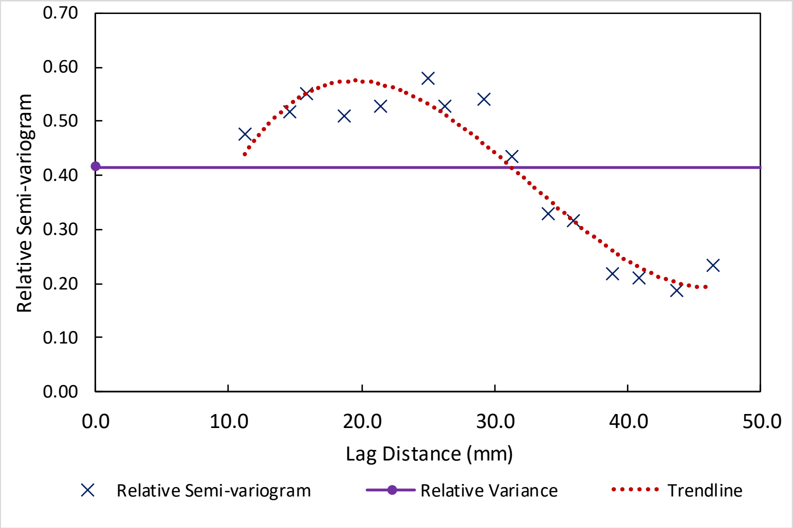

**L-3-2**

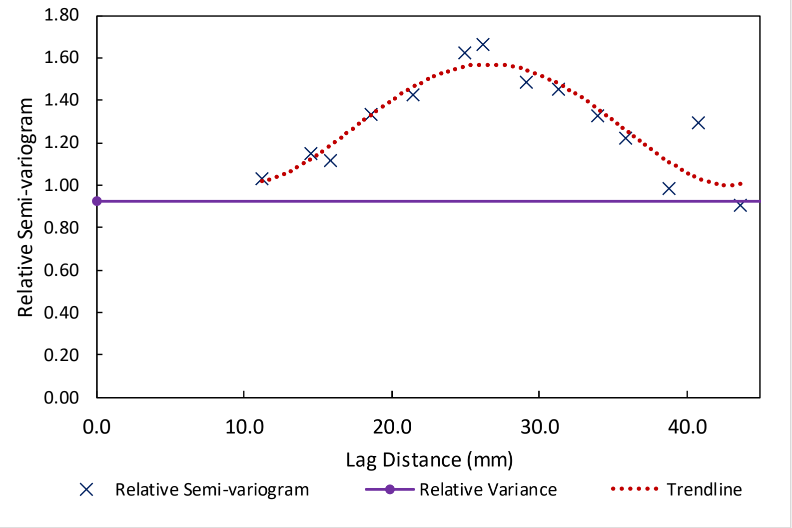

**L-3-3**

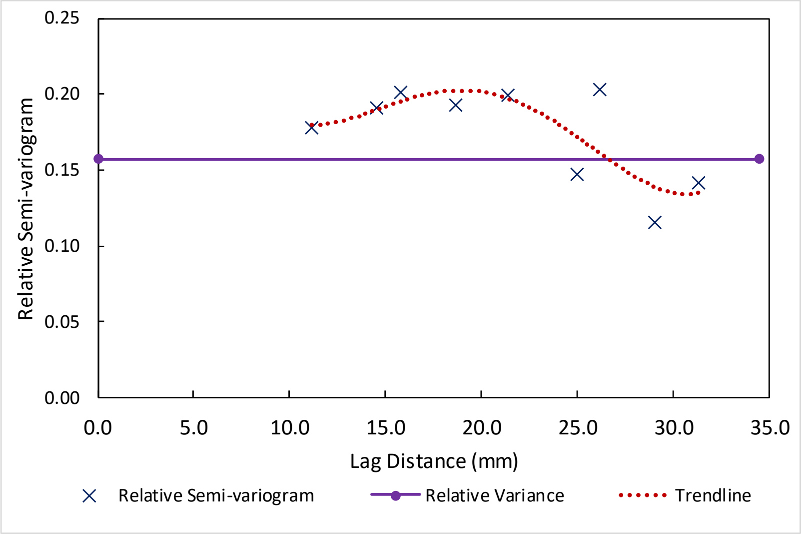

**L-3-4**

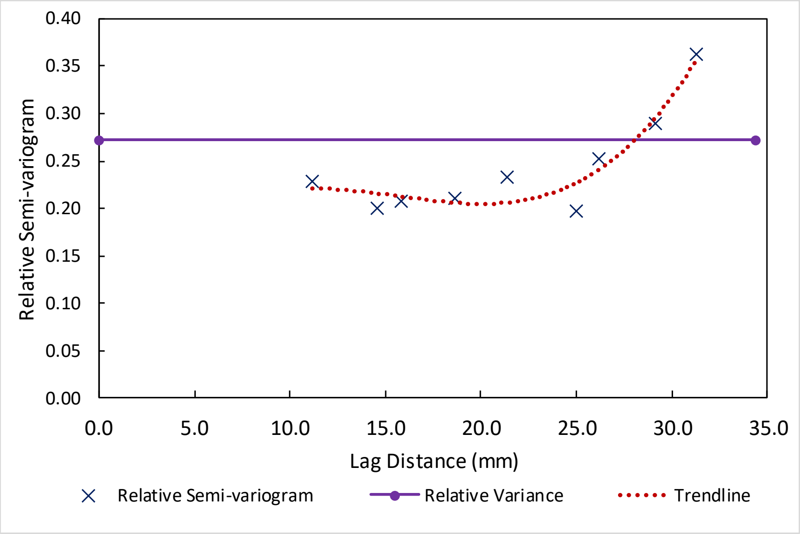

**L-4-1**

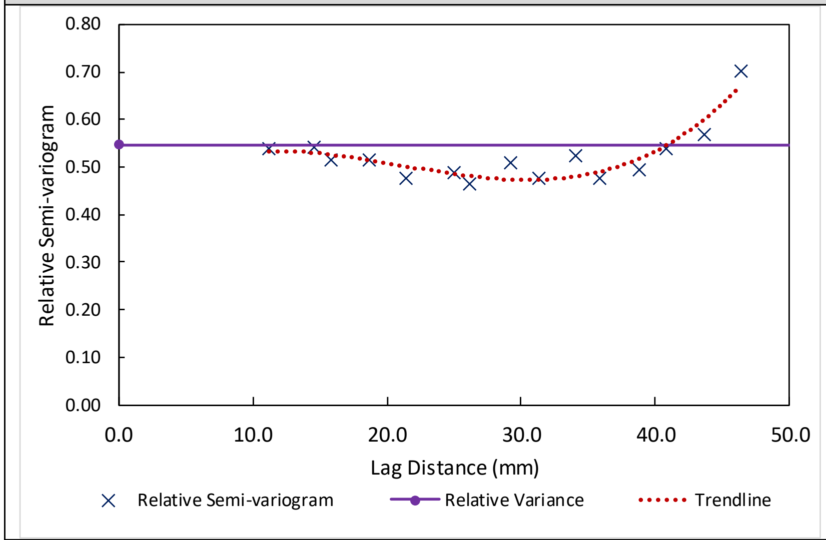

**L-4-2**

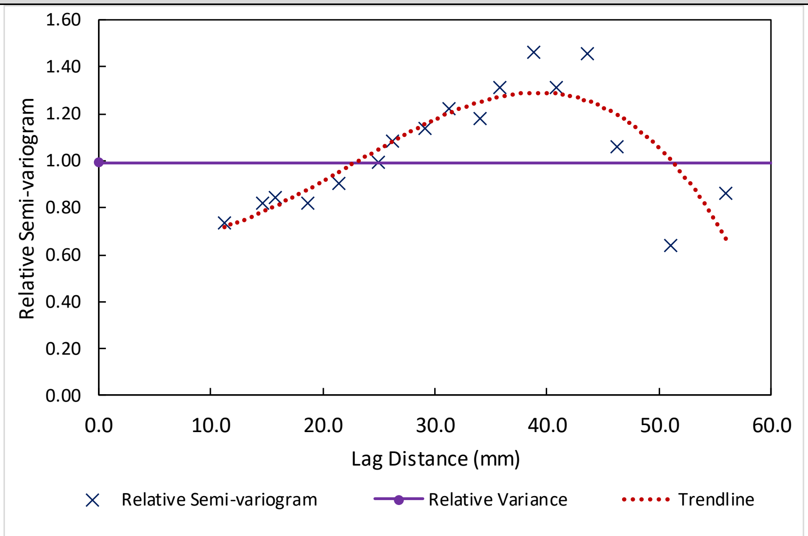

**L-4-3**

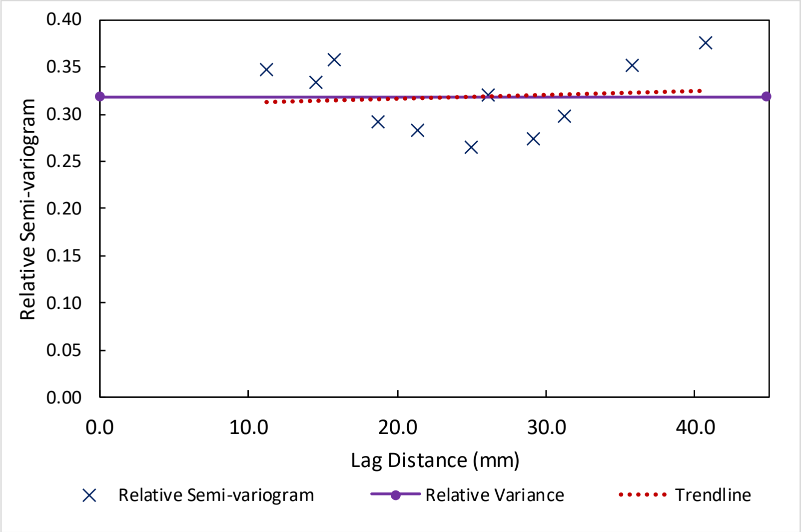

**L-4-4**

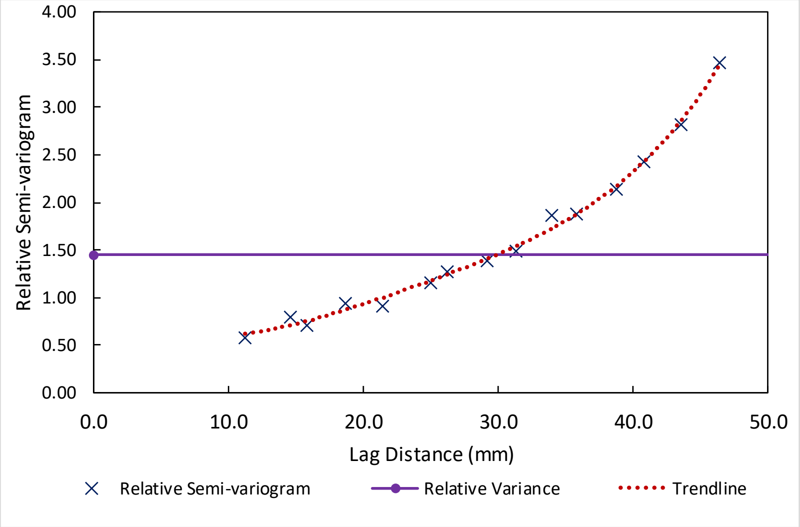

**L-5-1**

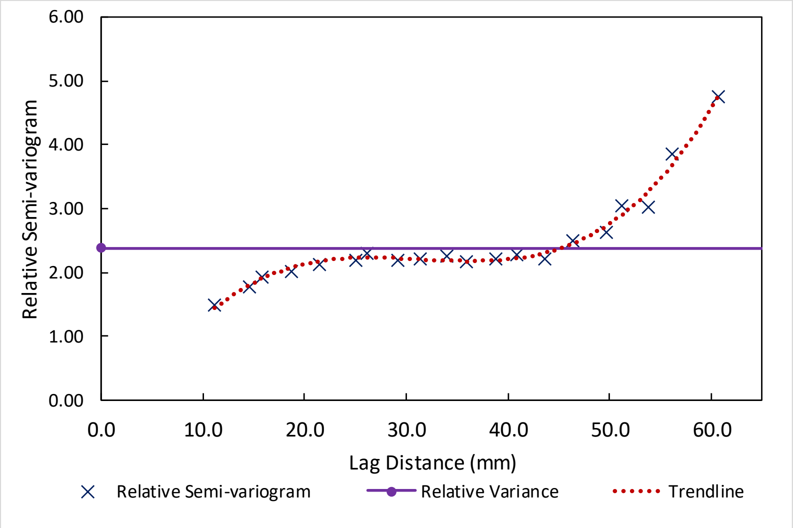

**L-5-2**

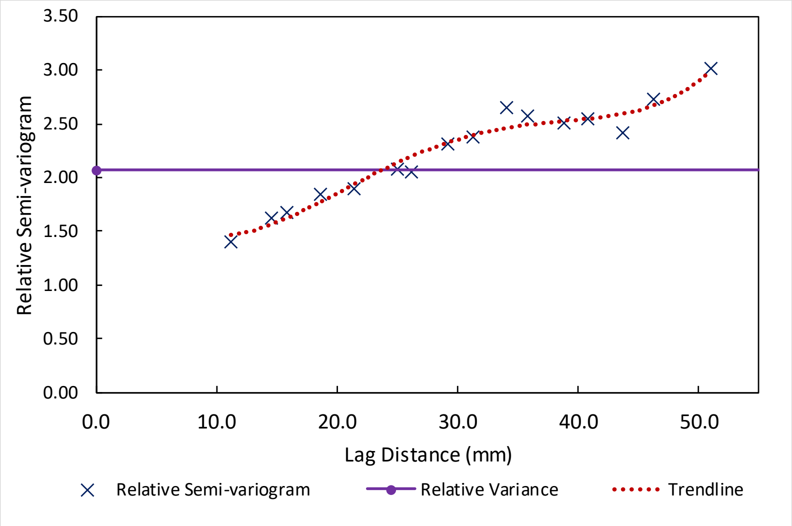

**L-5-3**

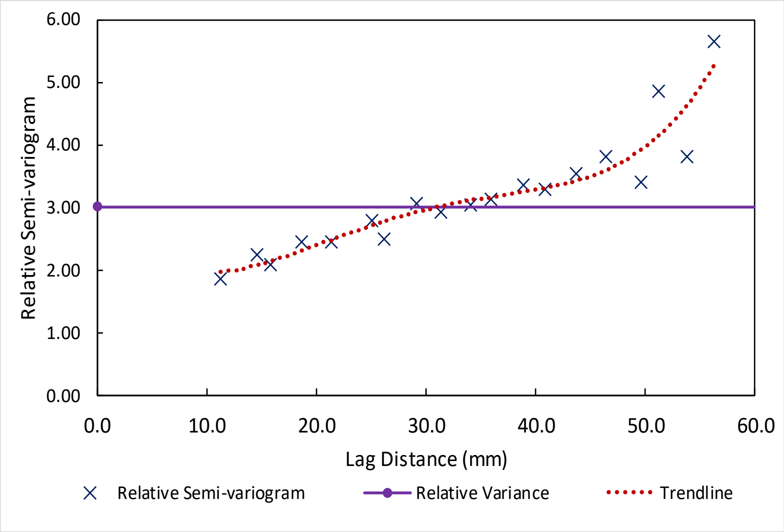

**L-5-4**

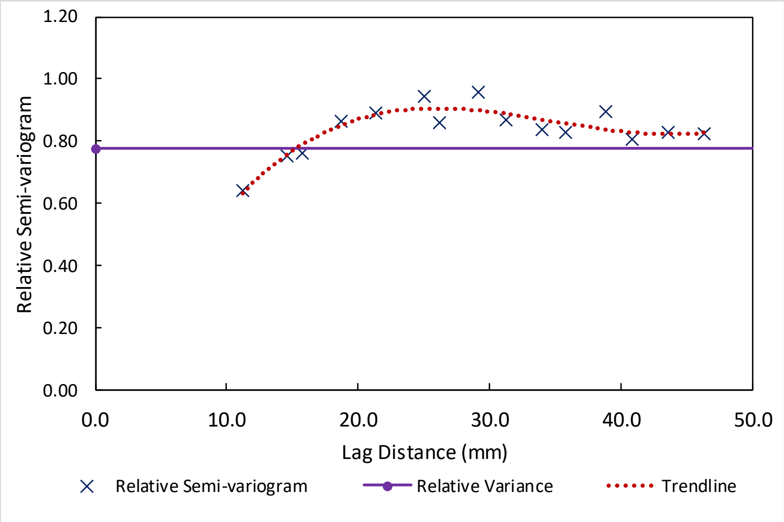

# Appendix H – Experimental variograms for iron grade

**H-1-1**

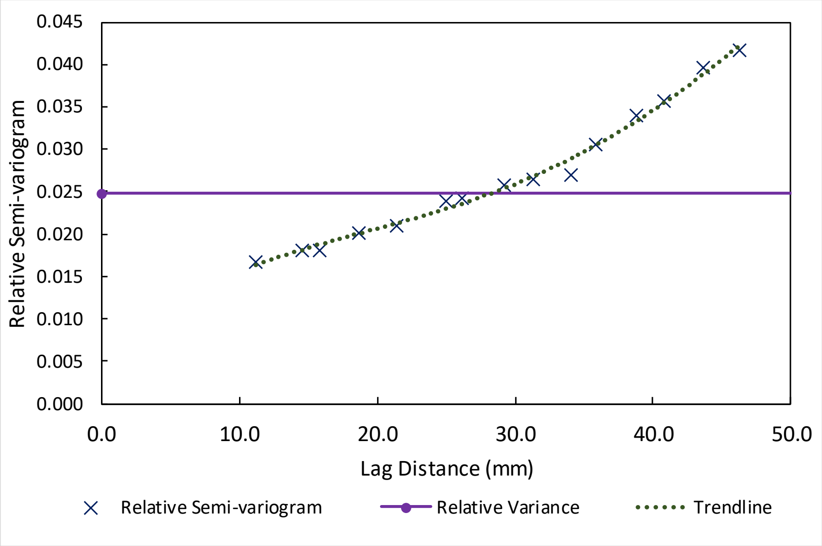

**H-1-2**

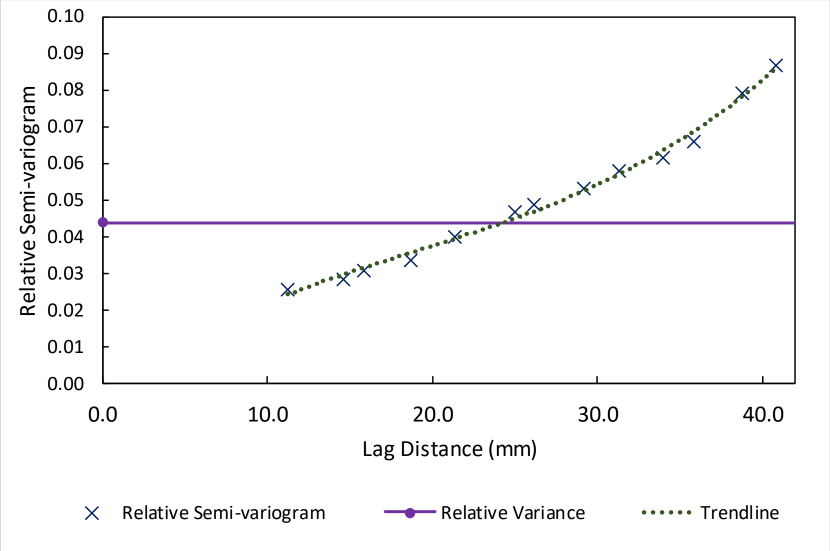

**H-1-3**

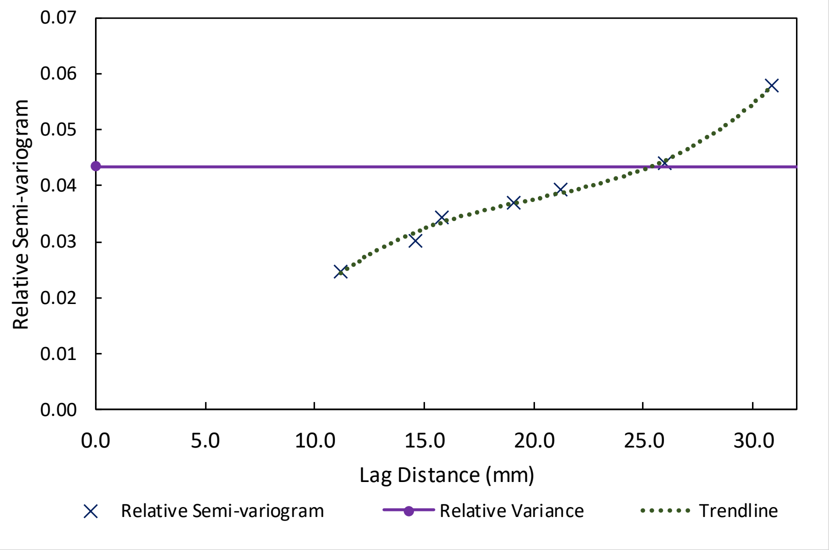

**H-1-4**

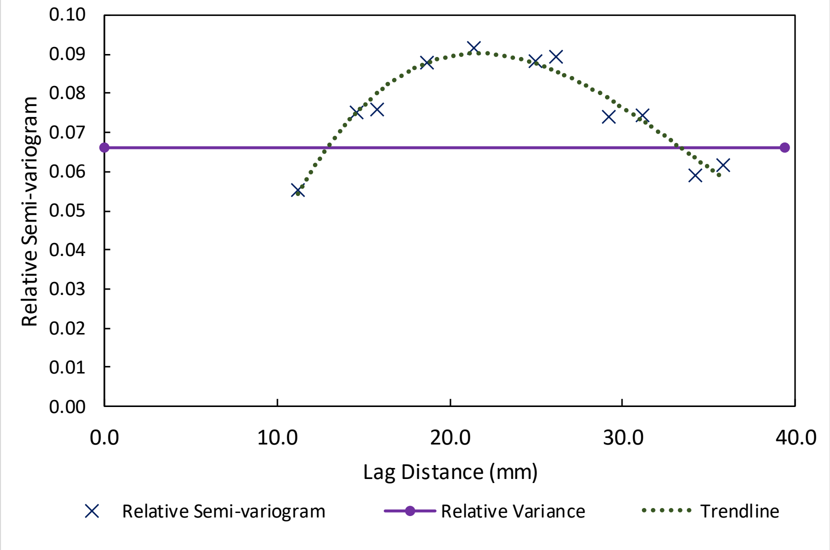

**H-2-1**

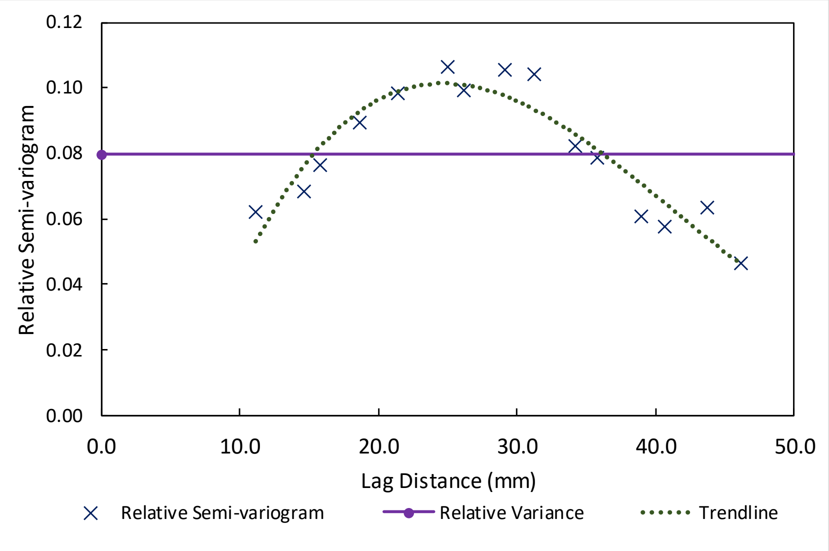

**H-2-2**

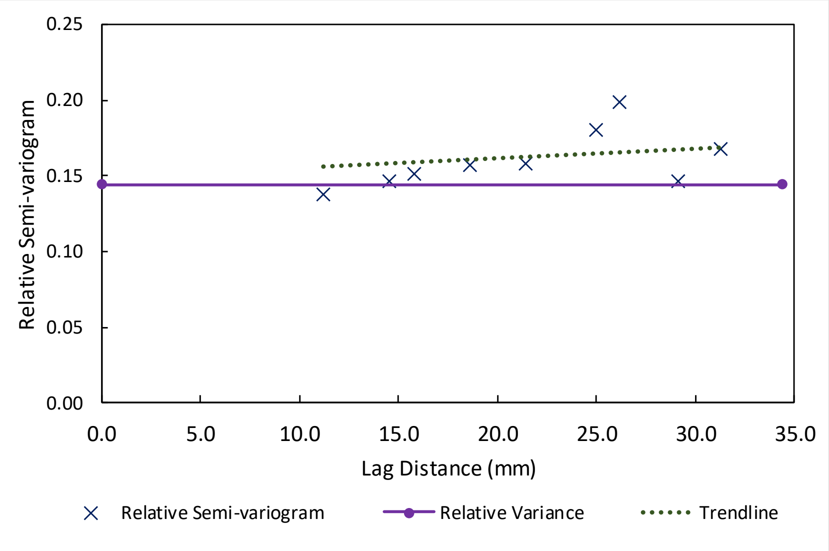

**H-2-3**

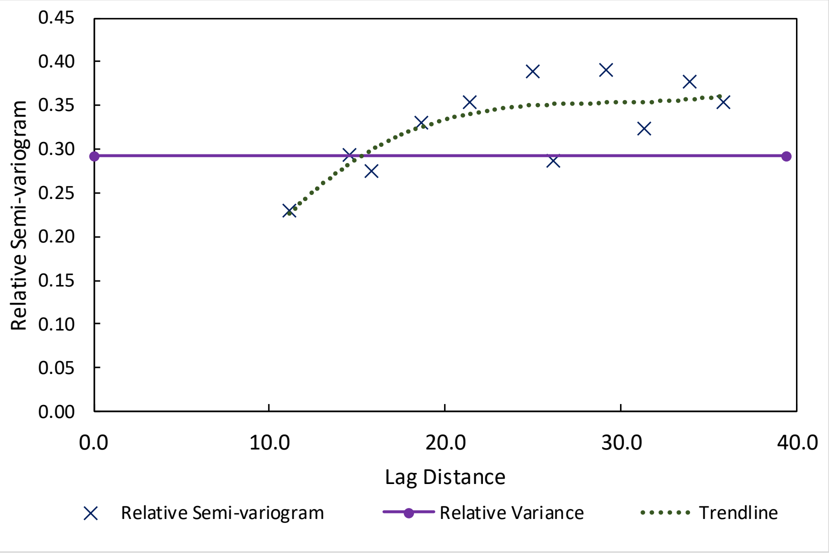

**H-2-4**

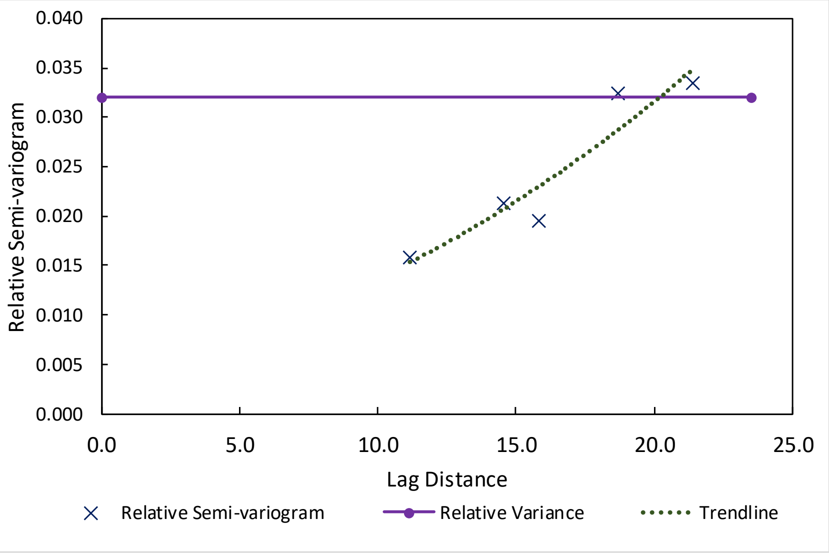

**H-3-1**

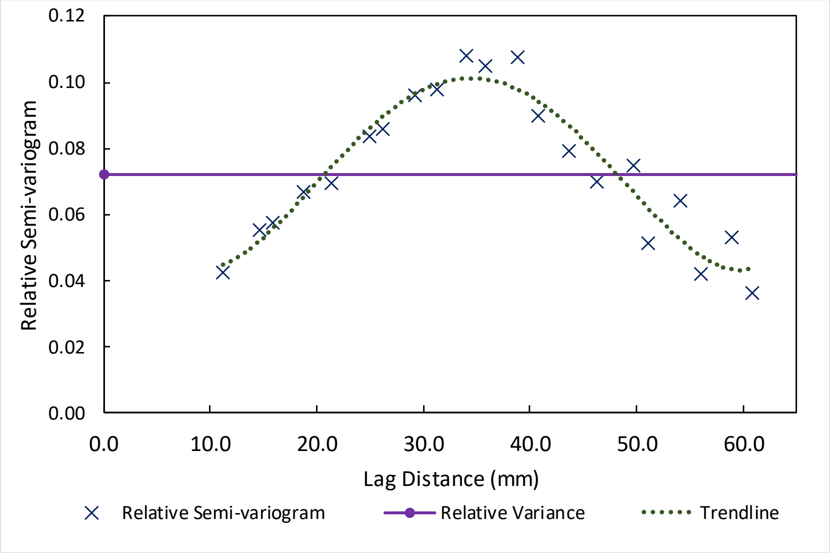

**H-3-2**

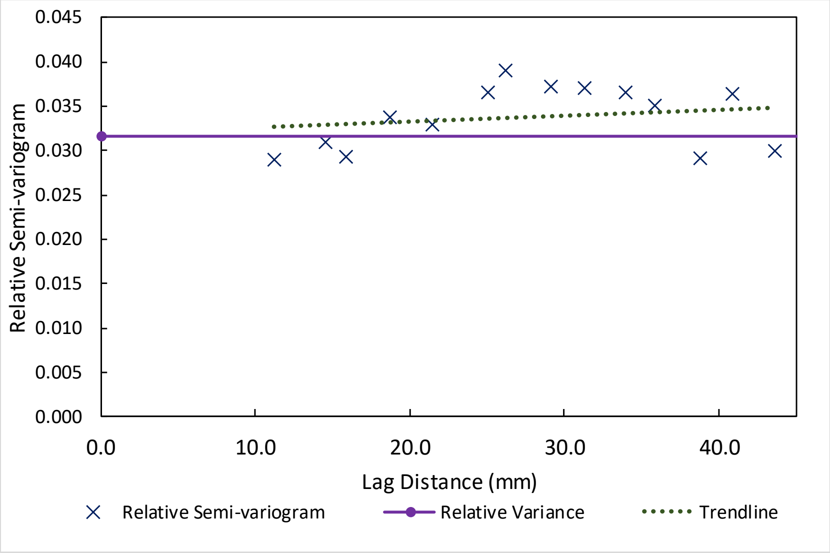

**H-3-3**

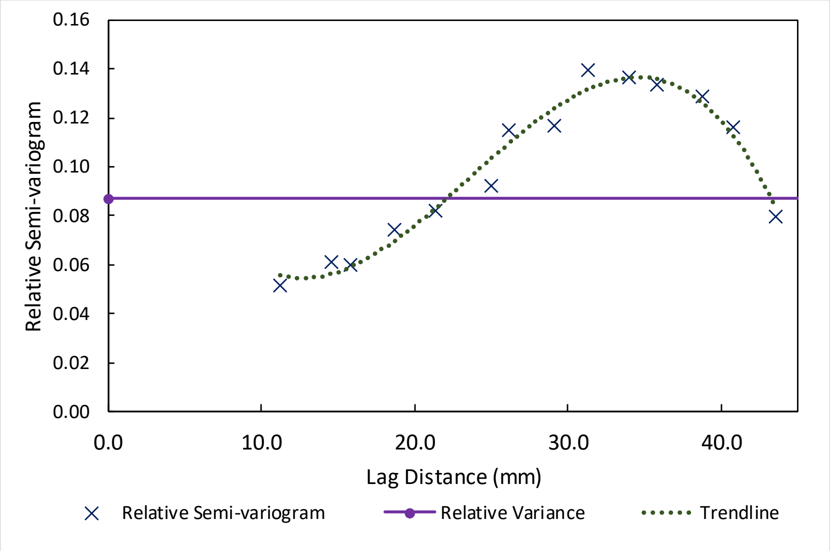

**H-3-4**

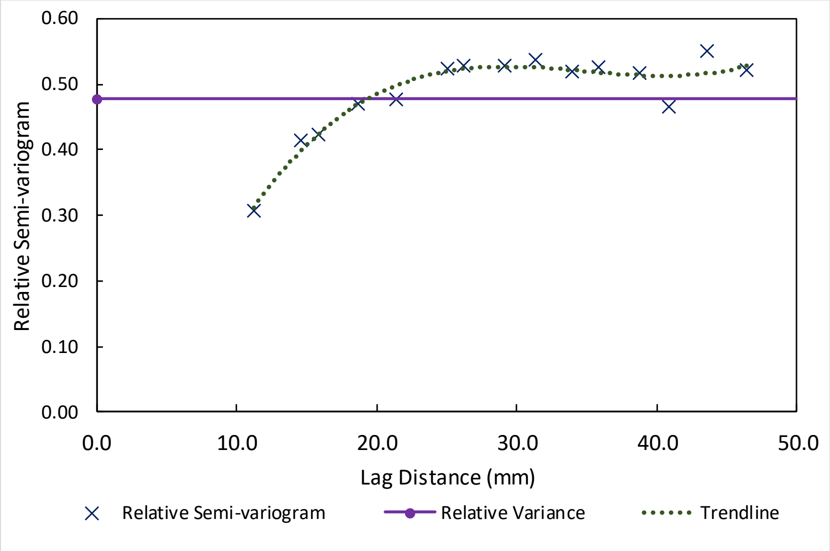

**H-4-1**

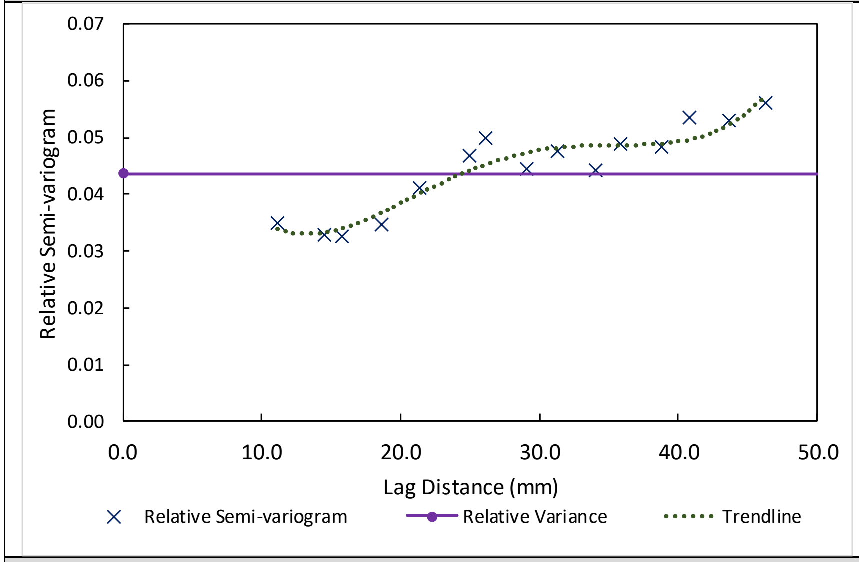

**H-4-2**

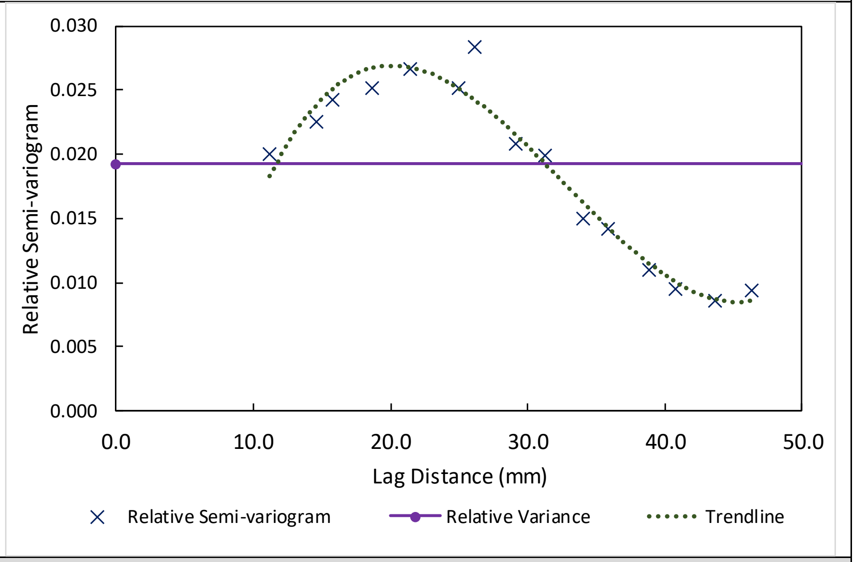

**H-4-3**

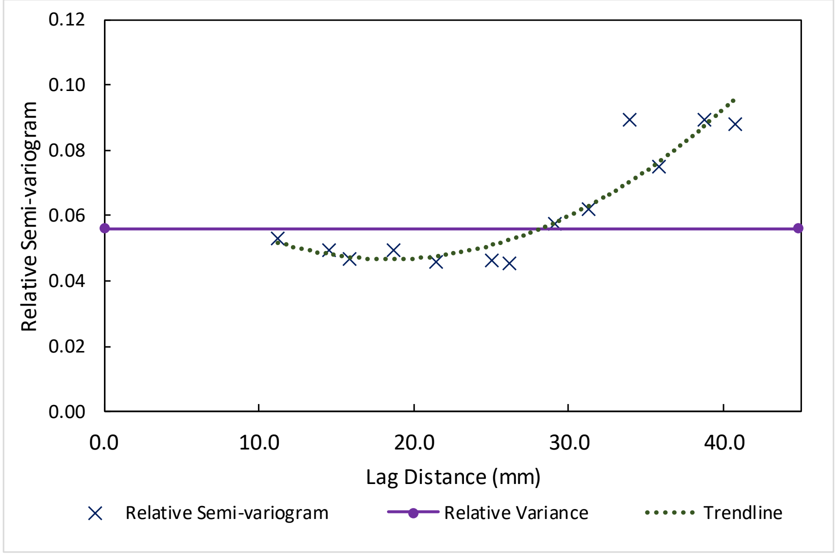

**H-4-4**

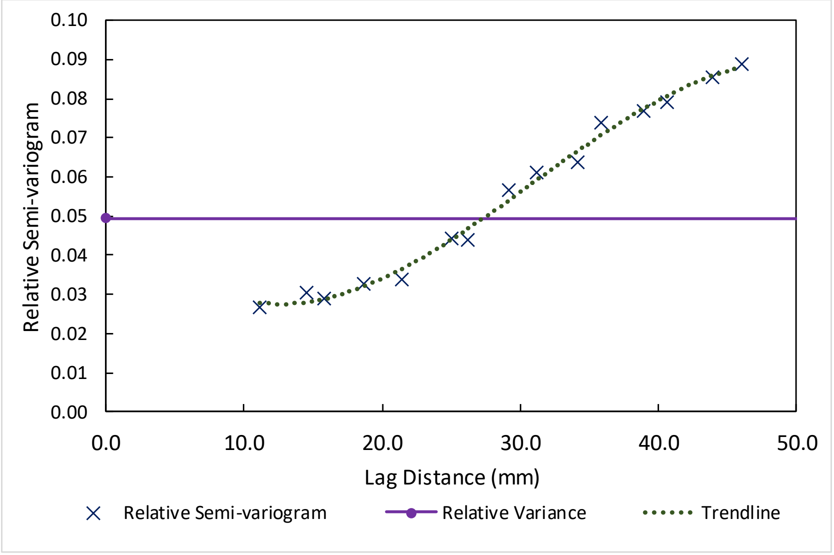

**H-5-1**

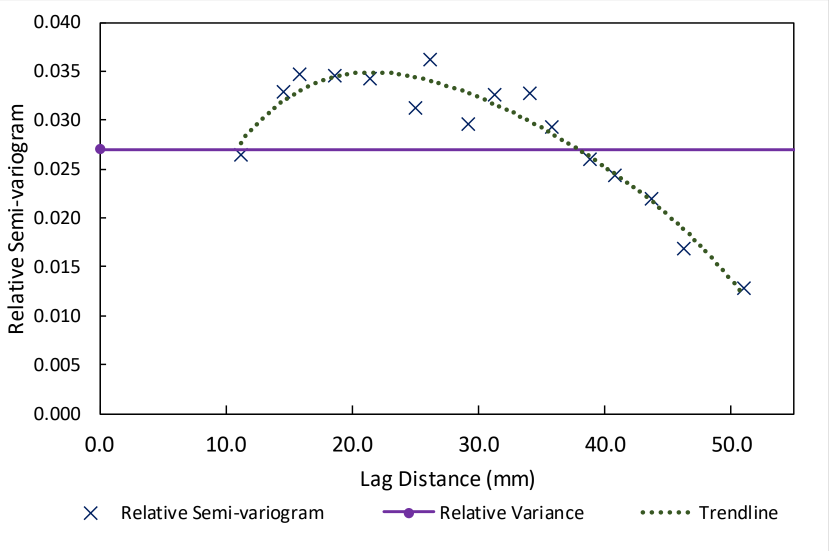

**H-5-2**

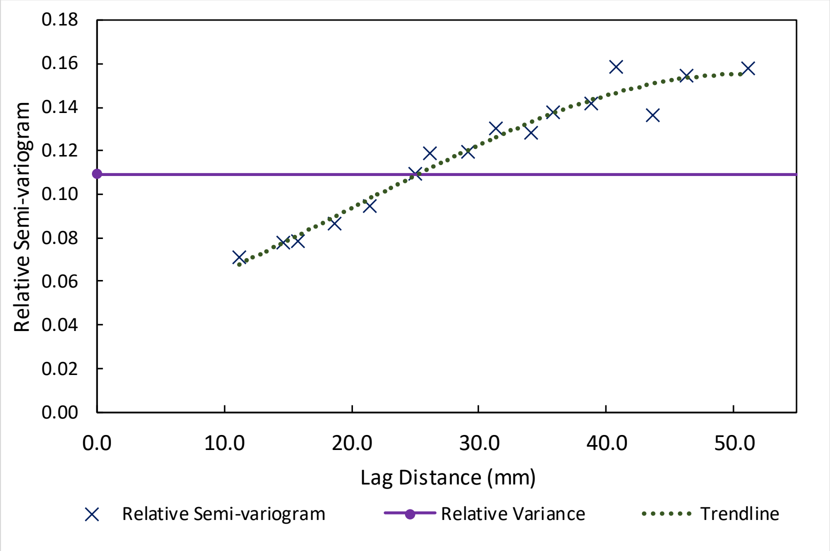

**H-5-3**

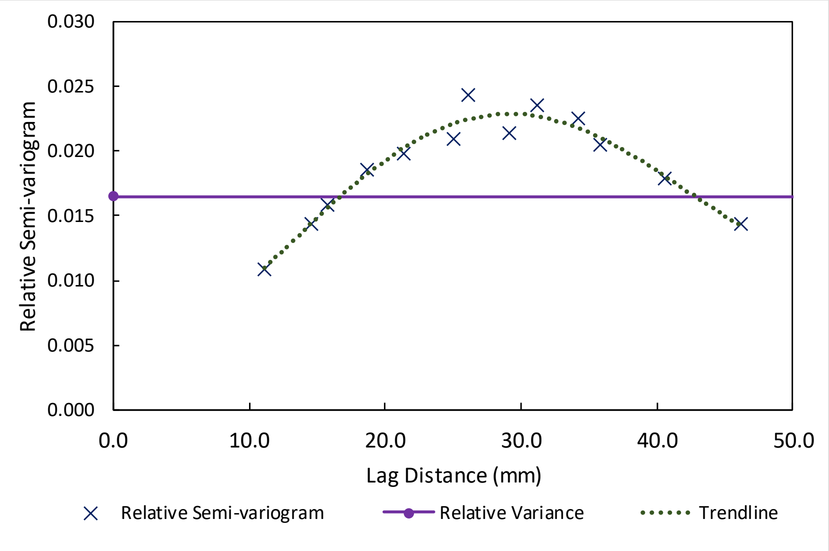

**H-5-4**

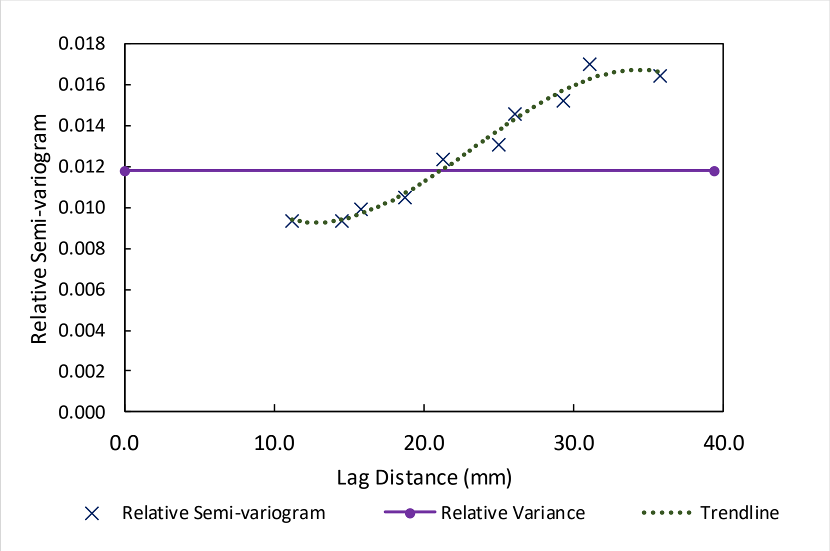

**L-1-1**

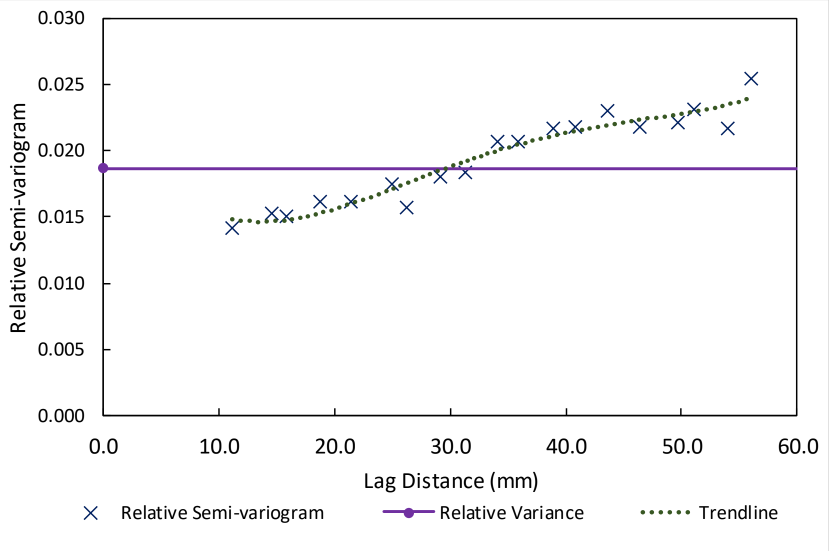

**L-1-2**

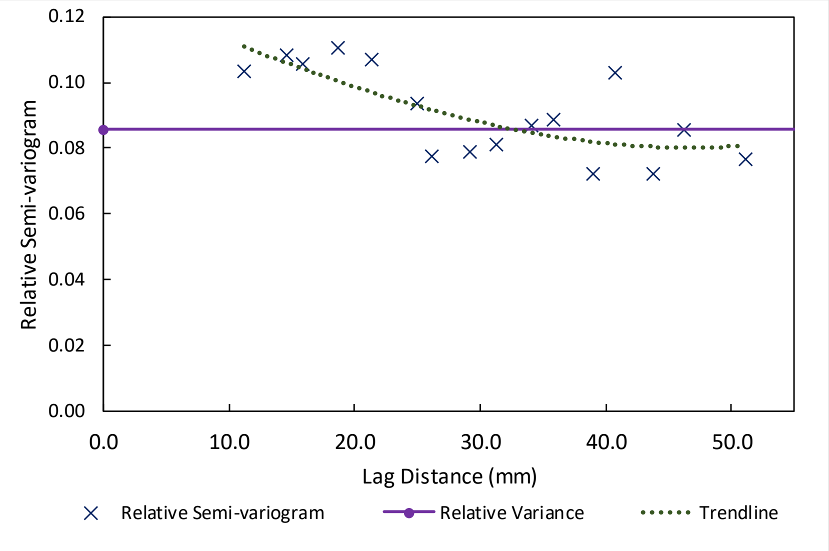

**L-1-3**

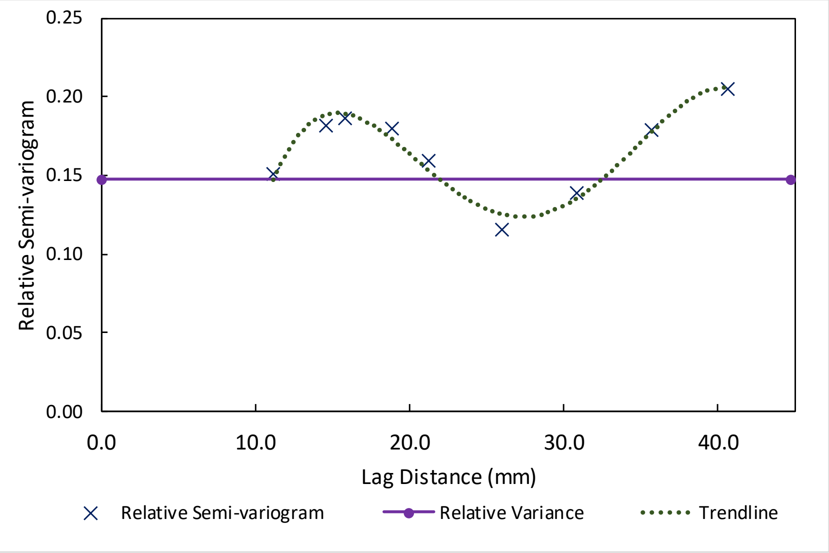

**L-1-4**

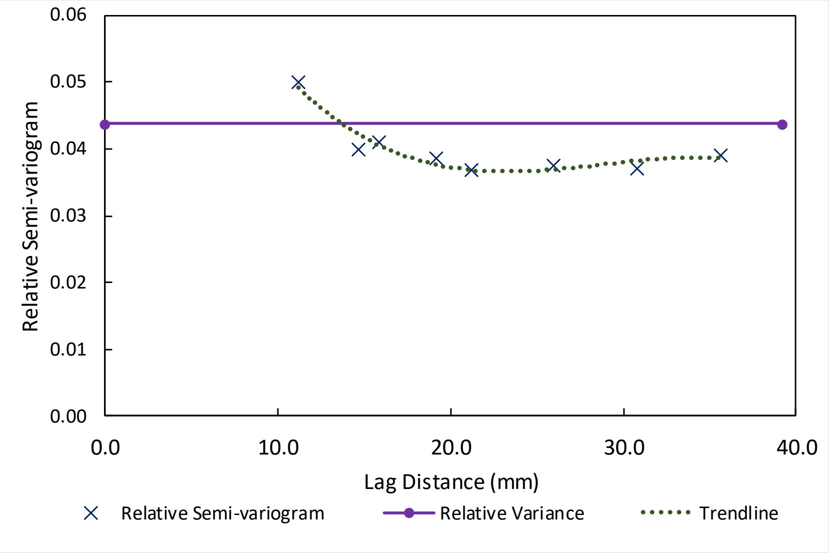

**L-2-1**

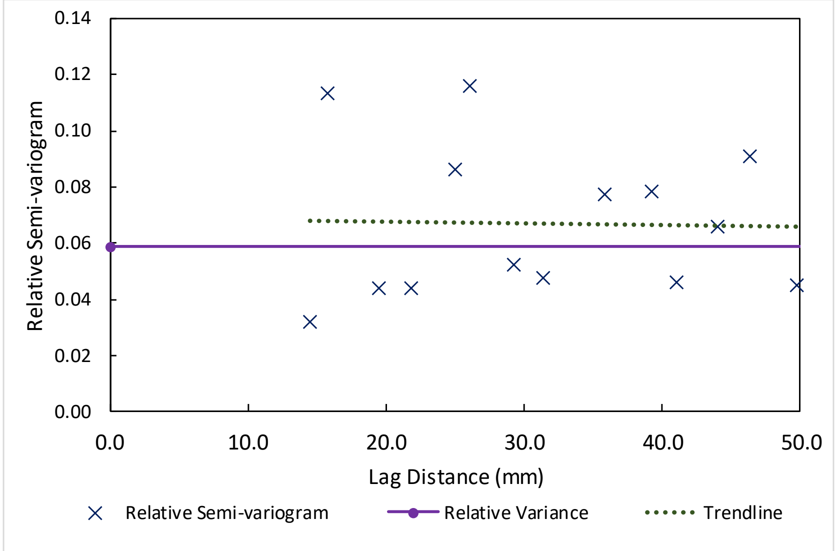

**L-2-2**

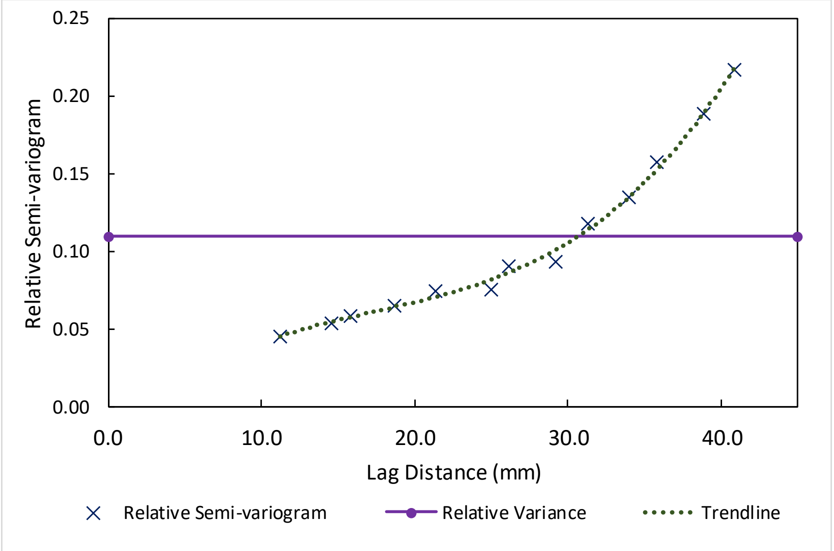

**L-2-3**

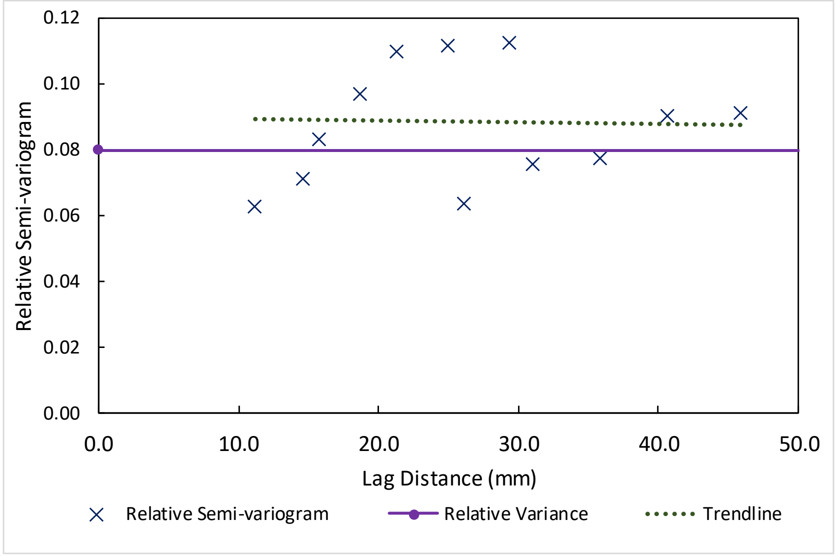

**L-2-4**

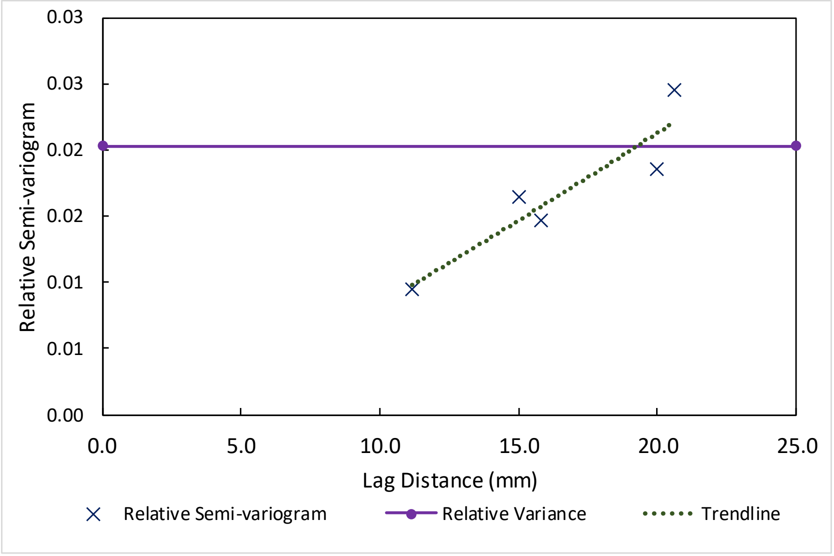

**L-3-1**

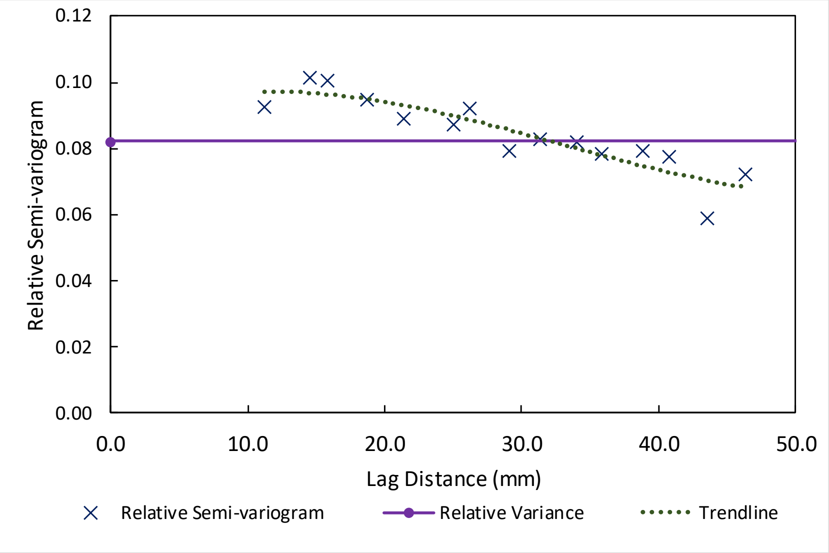

**L-3-2**

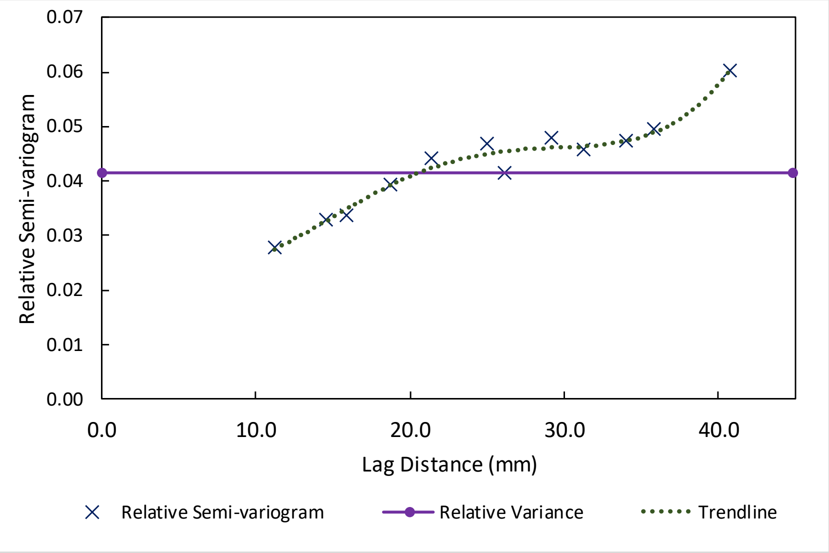

**L-3-3**

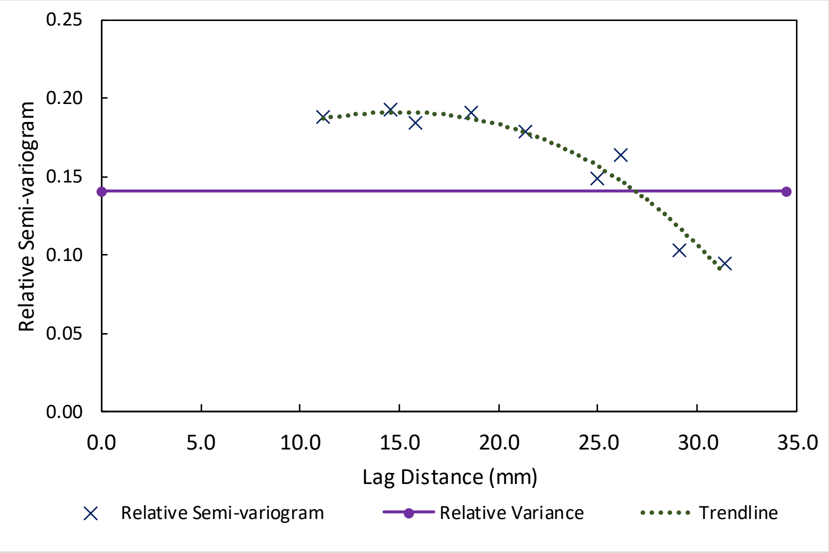

**L-3-4**

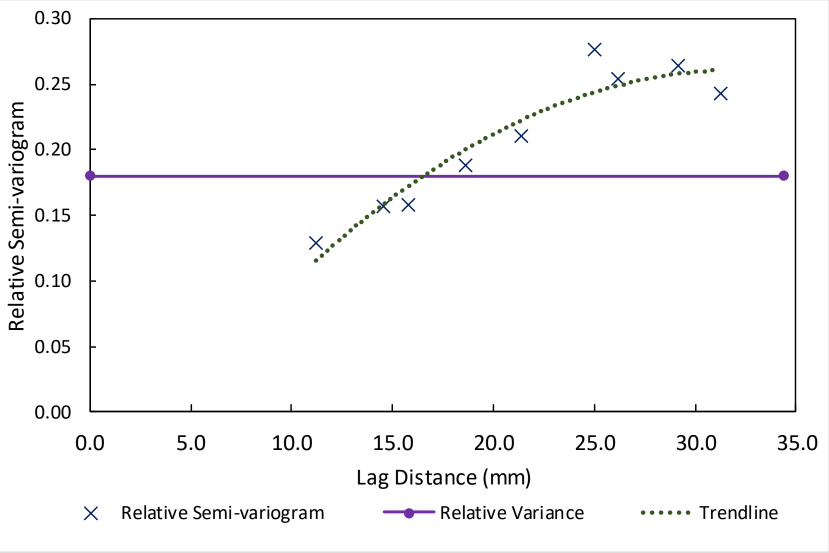

**L-4-1**

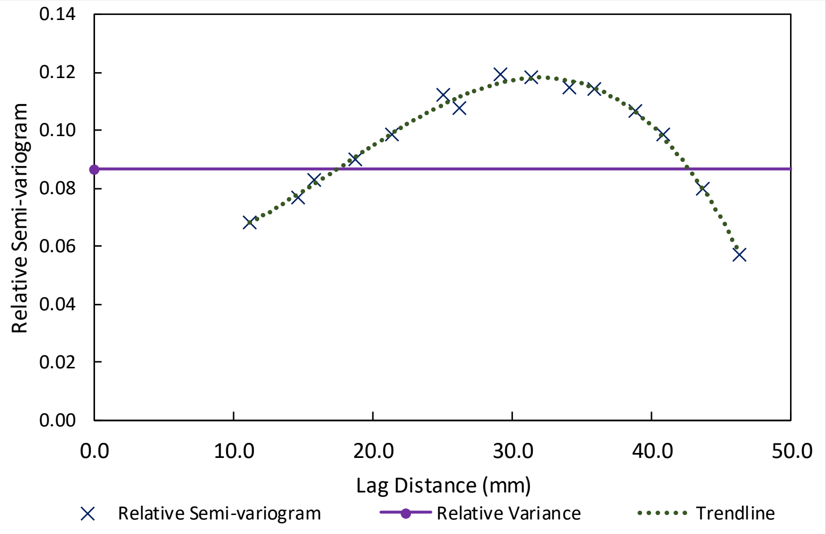

**L-4-2**

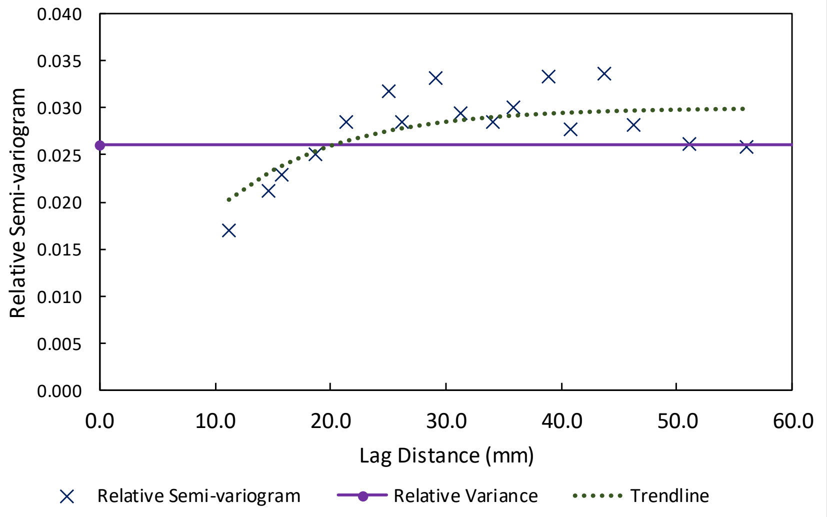

**L-4-3**

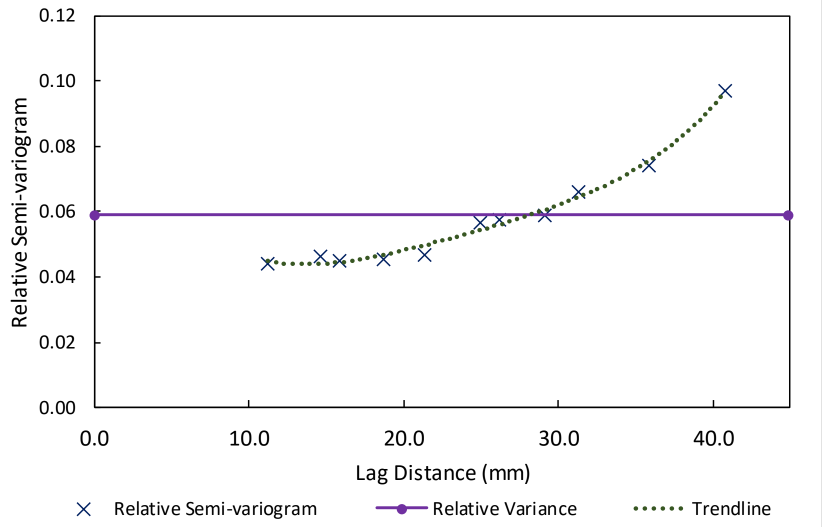

**L-4-4**

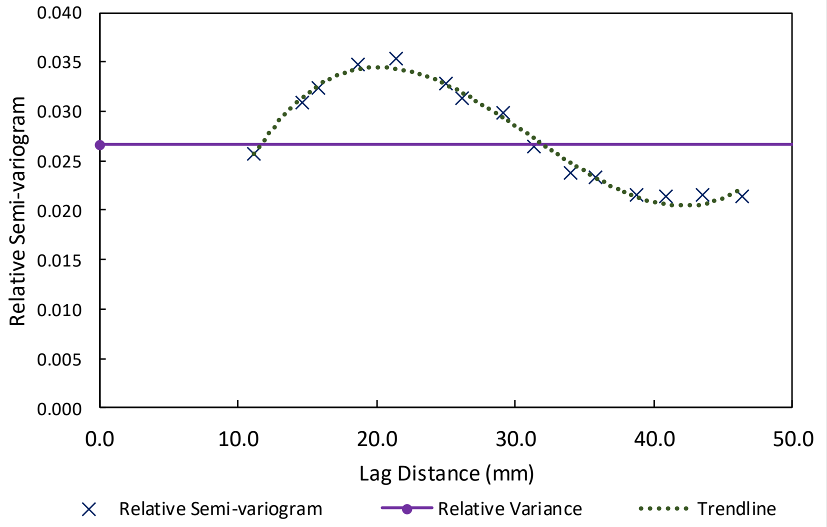

**L-5-1**

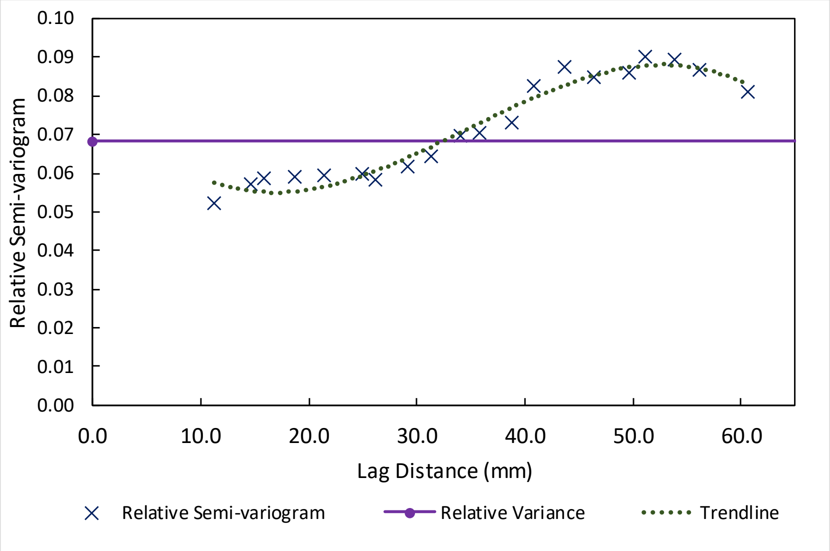

**L-5-2**

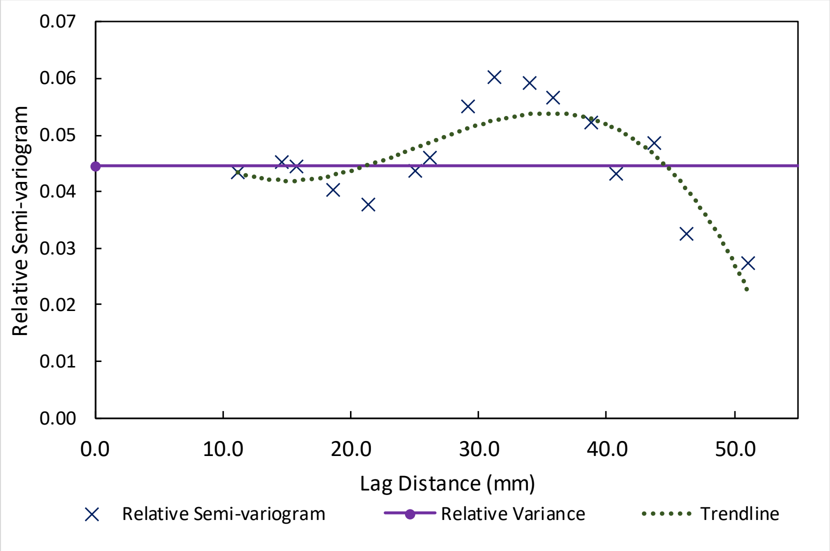

**L-5-3**

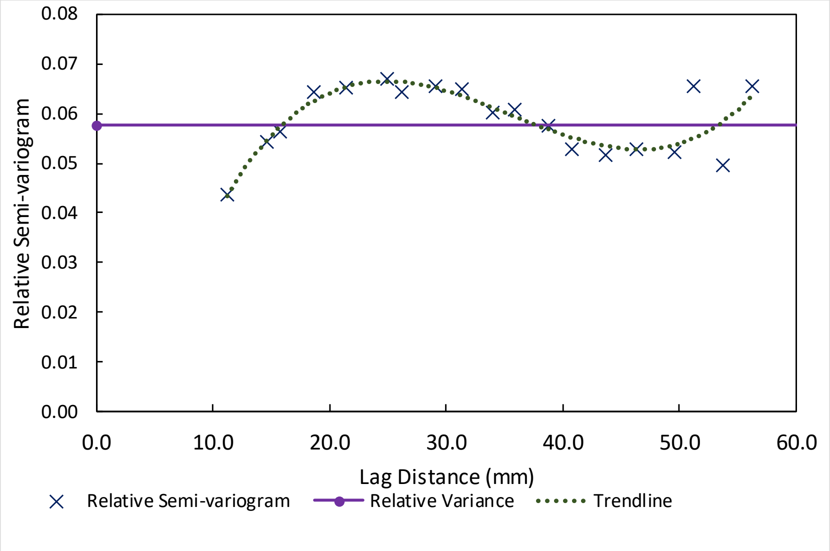

**L-5-4**

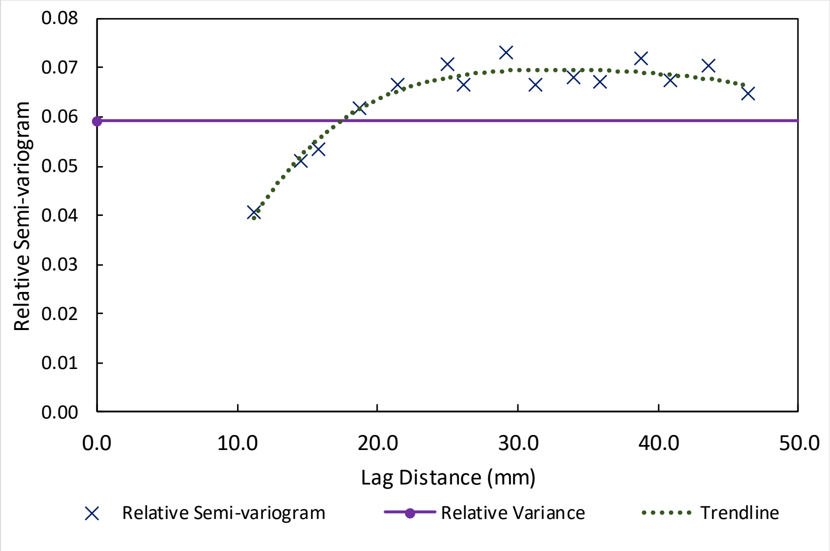

# Appendix I– Two-color mapping for copper grade (Red color for copper grades higher than 0.08%, blue color for copper grades lower than 0.08%)

**H-1-1**

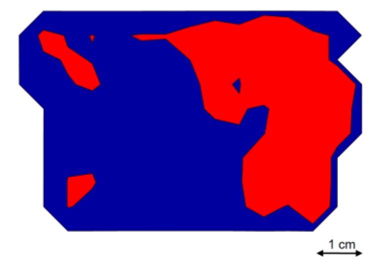

**H-1-2**

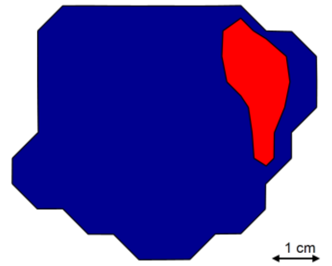

**H-1-3**

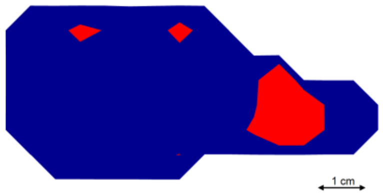

**H-1-4**

**H-2-1**

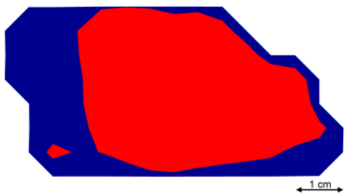

**H-2-2**

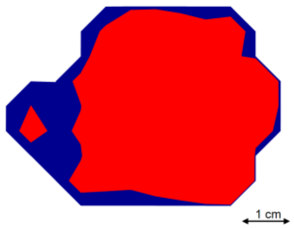

**H-2-3**

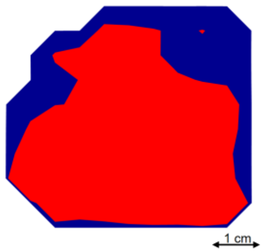

**H-2-4**

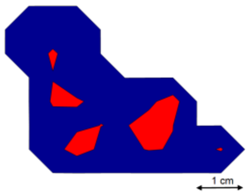

**H-3-1**

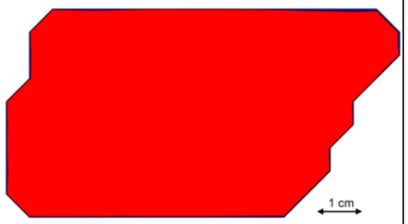

**H-3-2**

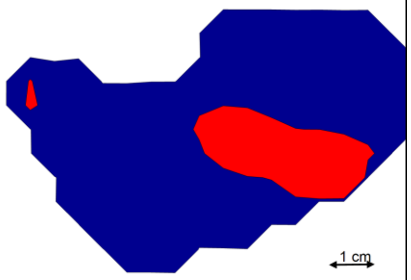

**H-3-3**

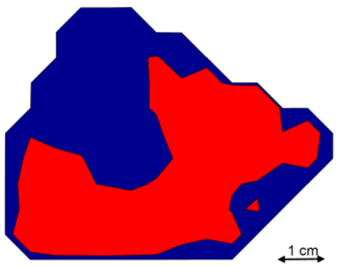

**H-3-4**

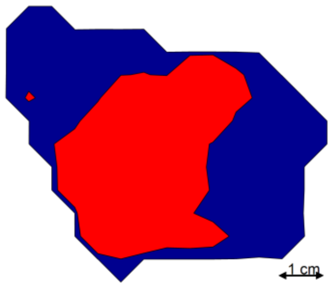

**H-4-1**

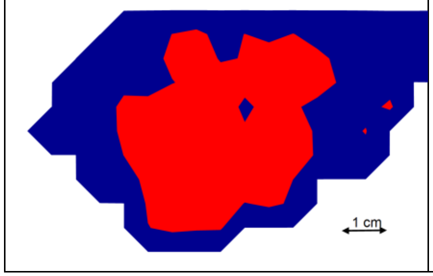

**H-4-2**

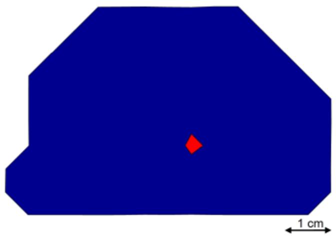

**H-4-3**

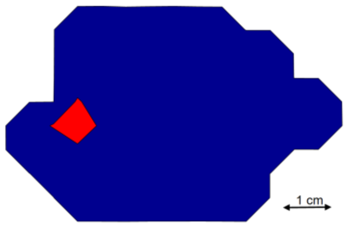

**H-4-4**

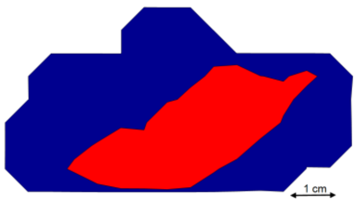

**H-5-1**

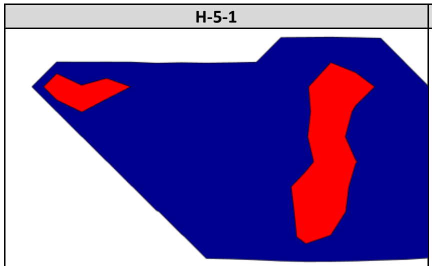

**H-5-2**

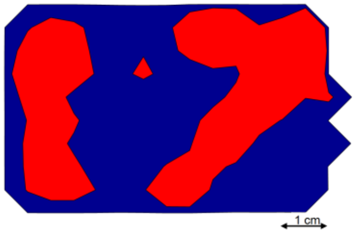

**H-5-3**

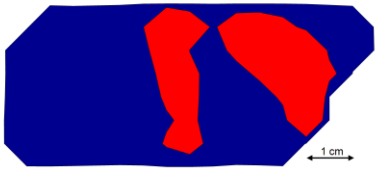

**H-5-4**

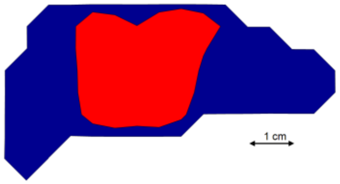

**L-1-1**

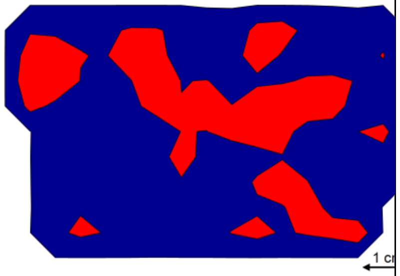

**L-1-2**

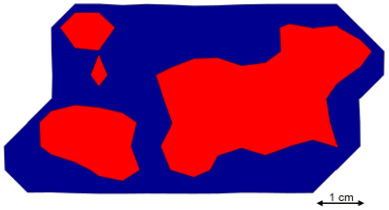

**L-1-3**

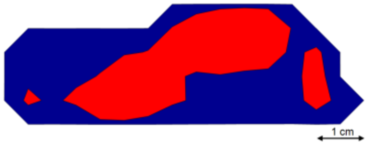

**L-1-4**

**L-2-1**

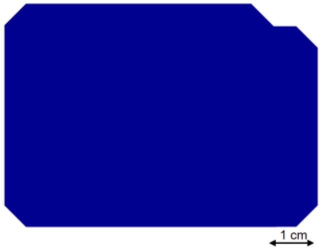

**L-2-2**

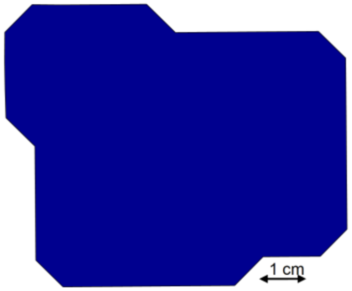

**L-2-3**

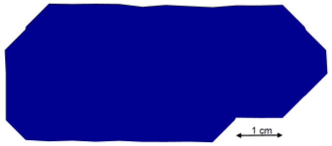

**L-2-4**

**L-3-1**

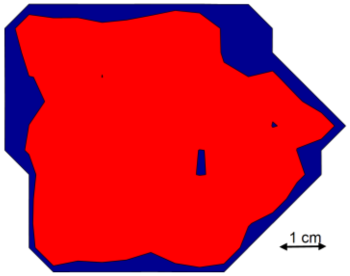

**L-3-2**

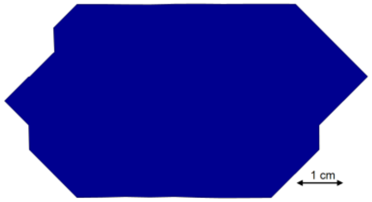

**L-3-3**

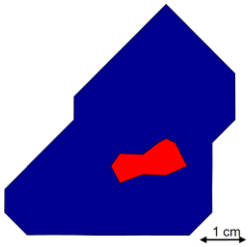

**L-3-4**

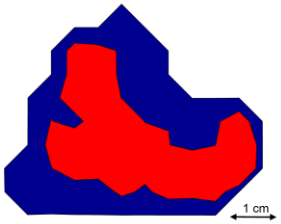

**L-4-1**

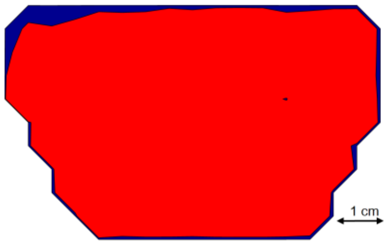

**L-4-2**

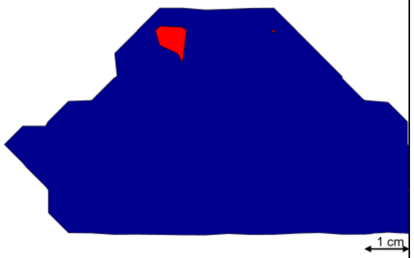

**L-4-3**

**L-4-4**

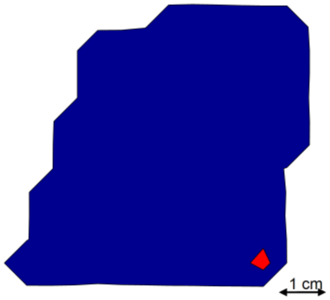

**L-5-1**

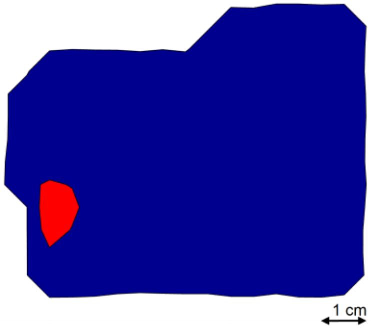

**L-5-2**

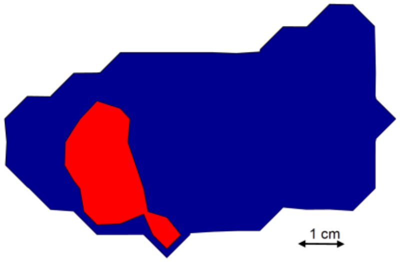

**L-5-3**

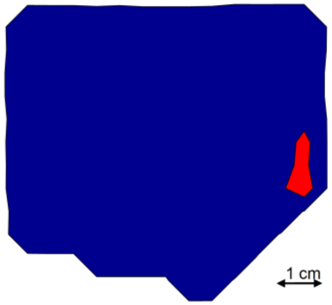

**L-5-4**